

**ILLUMINATING THE CELLULAR ANTENNA:  
PRINCIPLES OF CILIARY SIGNALING DISCOVERED BY  
MOLECULAR SENSORS AND ACTUATORS**

by

Siew Cheng Phua

A dissertation submitted to The Johns Hopkins University in conformity with the  
requirements of the degree of Doctor of Philosophy

Baltimore, Maryland

March, 2017

© Siew Cheng Phua

All Rights Reserved

# Abstract

Primary cilia function as specialized sensory antennae for cells to detect signals critical to proliferation and differentiation. Aberrant ciliary signaling is associated with developmental disorders commonly known as ciliopathies, as well as tumorigenesis. Understanding the principles of ciliary signaling is fundamental to developing strategies to treat cilia-related disorders. Yet, conventional imaging methods cannot sufficiently resolve ciliary signaling events occurring within a femtoliter volume from the cell body, and genetic or chemical perturbation are frequently non-specific. In this dissertation, our goal is to engineer molecular tools to illuminate ciliary signaling mechanisms and how they regulate cellular functions. We first developed a synthetic system for rapid, chemically-inducible trapping of protein probes in cilia. This system empowered us to discover a diffusion barrier at the ciliary base which regulates flux between the cilia and cytosol. We also built a robust series of genetically-encoded cilia-targeted calcium indicators and pioneered the visualization of ciliary calcium signals upon chemical and mechanical stimulation. Additionally, we established genetically-encoded actuators to manipulate phosphoinositides and actin in cilia. Using these tools, we proceeded to deconstruct primary cilia machinery. We revealed that an absence of phosphatidylinositol-4,5-bisphosphate (PI(4,5)P<sub>2</sub>) constitutes a fundamental aspect of primary cilia structural and functional identity. We first determined that PI(4,5)P<sub>2</sub> depletion is required for ciliary transduction of Hedgehog signals. Next, we discovered that PI(4,5)P<sub>2</sub> re-organization triggers actin polymerization in cilia, which excises cilia tips as extracellular ciliary vesicles in a process we call cilia decapitation. These conceptually new findings challenge currently-accepted models of cilia disassembly, and deliver novel concepts in organelle biogenesis. Moreover, we revealed that cilia decapitation occurs in quiescent cells, and drives G<sub>0</sub> to G<sub>1</sub> transit through Gli transcription factor activation. These findings propose decapitation-induced mitogenic signaling as a novel molecular link between the

ciliary life cycle and cell-division cycle. Overall, we have established a niche in cilia biology field by specifically focusing on ciliary signaling visualization and manipulation. The molecular strategies used in our studies are relevant to a broad, interdisciplinary audience. Importantly, the principles of ciliary signaling we discovered establish a solid ground for understanding disorders caused by sensory defects of the cellular antennae.

**Thesis advisor:** Takanari Inoue, Ph.D.

**Thesis readers:** Miho Iijima, Ph.D., Takanari Inoue, Ph.D.

**Thesis committee:** Andrew Holland, Ph.D., Miho Iijima, Ph.D., Rong Li, Ph.D.

# Acknowledgements

I would first like to thank my advisor, Dr. Takanari Inoue for his mentorship during my Ph.D. studies. The great balance of scientific guidance and freedom he provided has trained me to look at science from broader perspectives, and I also became confident to ask and attempt to answer different interesting scientific questions.

I would also like to acknowledge the members of my thesis committee, Drs. Andrew Holland, Miho Iijima and Rong Li for their insightful comments on my scientific work and presentations. My dissertation work was based on strong collaborations in the United States and Japan. I express my gratitude to Drs. Jeremy Reiter, Francesc Garcia and Elle Roberson at University of California, San Francisco and Drs. Rajat Rohatgi and Ganesh Pusapati at Stanford University for their expertise in Hedgehog signaling, Dr. Koji Ikegami at Hamamatsu University School of Medicine for his expertise in proteomics, as well as Dr. Shuhei Chiba at Osaka University for his expertise in electron microscopy and super-resolution imaging.

During my time in the Inoue lab, I have met many wonderful people that I will remember in the years to come. Helen, Albert, Allison, Frank and Steven are amazing lab buddies. I can always depend on them to discuss about anything from scientific ideas to food to pets, and they are always there to add some fun and humor to my everyday lab life. Bob, Hideki and Elmer were/are my bench-mates, and they have also been great company during my daily work. I am especially appreciative to Frank, Steven, and Emily, whom I worked together with as part of the “cilia team” during the earlier and mid-phases of my graduate training.

Finally, I would like to thank my Mum, Dad and sister in Singapore for providing unconditional love and encouragement during my years abroad. I am also very fortunate and grateful to have Xianrong and my cat, Wumao, for companionship during my time here in Baltimore.



# Table of Contents

Abstract.....	ii
Acknowledgements.....	iv
Table of Contents.....	vi
List of Tables .....	ix
List of Figures .....	x
Chapter 1 Introduction .....	1
1.1    Primary cilia structural and functional architecture.....	1
1.1.1    Overall structure .....	1
1.1.2    Ciliary receptors.....	2
1.1.3    Ciliary ion channels .....	3
1.1.4    Ciliary lipid metabolism enzymes .....	4
1.1.5    Ciliary intraflagellar transport .....	5
1.2    The capabilities of primary cilia as signaling antennae .....	5
1.3    Coupling between the cilia life cycle and the cell-division cycle.....	7
1.4    Developmental roles of primary cilia .....	9
1.5    Ciliopathies and cancer .....	10
1.6    Specific aims.....	12
Chapter 2 Earlier work.....	17

## Chapter 3 Genetically encoded calcium indicator illuminates calcium dynamics in primary

cilia .....	18
3.1 Overview.....	18
3.2 Results.....	18
3.2.1 Construction and characterization of cilia-targeted genetically encoded calcium indicators.....	18
3.2.2 Ciliary calcium responses to chemical stimulation.....	20
3.2.3 Ciliary calcium responses to mechanical stimulation.....	21
3.3 Discussion.....	22
3.4 Materials and Methods.....	22
3.4.1 DNA Construction .....	22
3.4.2 Cell culture and transfection .....	24
3.4.4 Immunofluorescence.....	25
3.4.5 Transmission electron microscopy .....	25
3.4.6 Epi-fluorescence imaging .....	26
3.4.7 Ciliary and cytoplasmic pH determination .....	27
3.4.8 Flow system coupled with epi-fluorescence time-lapse imaging .....	27
3.4.9 Accession codes.....	28
Chapter 4 Phosphoinositides dictate function and structure identity of primary cilia .....	56
4.1 Overview.....	56

4.2	Results.....	57
4.2.1	Inpp5e regulates ciliary phosphoinositides .....	57
4.2.2	Phosphoinositides regulate ciliary protein trafficking to modulate Hedgehog signaling .....	59
4.2.3	Inpp5e loss and growth stimulation promote ciliary vesicle release .....	59
4.2.4	Growth-stimulated cilia decapitation entails ciliary Inpp5e depletion and PI(4,5)P <sub>2</sub> re-distribution.....	60
4.2.5	Ciliary PI(4,5)P <sub>2</sub> induces F-actin in ciliary lumen.....	62
4.2.6	Intraciliary actin polymerization is required for cilia decapitation.....	62
4.2.7	Released ciliary vesicles contain IFT-B and related cargoes.....	64
4.2.8	Cilia decapitation is required for cilia disassembly .....	65
4.2.9	Cilia decapitation ensures timely quiescence exit .....	66
4.2.10	Cilia decapitation modulates Gli transcription factor activity .....	67
4.3	Discussion.....	68
4.4	Materials and Methods.....	71
4.4.1	Cell culture.....	71
4.4.2	Transient and stable transfection .....	72
4.4.3	DNA plasmid construction .....	72
4.4.4	Generation of Ift88-KO mIMCD-3.....	73
4.4.5	Generation of Ift81:YNL knock-in mIMCD-3 .....	73

4.4.6	Generation of NIH/3T3-Flp-In: 8xGBS-GFP and reporter assay .....	74
4.4.7	Immunofluorescence.....	74
4.4.8	Epi-fluorescence imaging .....	75
4.4.9	Confocal imaging.....	75
4.4.10	Structured illumination microscopy imaging.....	75
4.4.11	Quantitative image analyses .....	76
4.4.12	Ciliary vesicle collection .....	77
4.4.13	Western blotting.....	77
4.4.14	LC-MS/MS of proteins in pelleted conditioned culture media.....	78
4.4.15	Proteomic analyses .....	79
4.4.16	Quantitative real-time PCR.....	80
4.4.17	Quantification and statistical analysis.....	80
Chapter 5 Overall conclusion and outlook.....		130
Bibliography .....		138
Curriculum Vitae .....		149

# List of Tables

Table 1-1 A non-exhaustive list of gating stimuli and regulators for each cilia-residing TRP channel.....	16
Table 3-1 Complete list of all CTS-tagged GECI and characterization of their targeting ability and functionality in the cytosol and cilia of NIH-3T3 cells .....	54
Table 4-1 List of protein candidates detected twice or more in at least one experimental condition, Related to Figures 4-10A-B.....	121
Table 4-2 List of protein candidates detected twice or more in growth-stimulated WT or <i>Ift88</i> -KO mIMCD-3 conditioned culture media, Related to Figures 4-10C-D .....	125

# List of Figures

Figure 1-1 Primary cilia structural and functional architecture .....	14
Figure 3-1 The inability of small molecule dyes to detect increases in ciliary $\text{Ca}^{2+}$ .....	30
Figure 3-2 Targeting efficiency of different CTSs and their effects on ciliation efficiency, cilia length, and cilia morphology in NIH-3T3 cells .....	31
Figure 3-3 Representative images of NIH-3T3 cells transfected with the various GFP CTS tagged constructs .....	33
Figure 3-4 Cilia length versus morphology for 5HT <sub>6</sub> -GFP, IA-GFP, and 5HT <sub>6</sub> -G-GECO1.0 constructs .....	34
Figure 3-5 Representative images of mIMCD3 cilia expressing 5HT <sub>6</sub> -YFP immunostained to reveal the location of various ciliary proteins .....	35
Figure 3-6 Representative TEM images of primary cilia and basal bodies in NIH-3T3 cells expressing GFP and 5HT <sub>6</sub> -GFP .....	36
Figure 3-7 The targeting ability of various CTS-tagged GECI.....	37
Figure 3-8 The functionality of various CTS-tagged GECI in the cytosol of NIH-3T3 cells.....	38
Figure 3-9 The functionality of 5HT <sub>6</sub> -G-GECO1.0, IA-G-GECO1.0, and 5HT <sub>6</sub> -YC3.60 in cilia of NIH-3T3 cells .....	40
Figure 3-10 5HT <sub>6</sub> -G-GECO1.0 targets primary cilia and detects changes in ciliary $\text{Ca}^{2+}$ .....	42
Figure 3-11 5HT <sub>6</sub> -G-GECO1.0 detects ciliary $\text{Ca}^{2+}$ influxes in response to ATP .....	43

Figure 3-12 5HT <sub>6</sub> -G-GECO1.0 can detect ciliary Ca <sup>2+</sup> fluxes due to ATP .....	45
Figure 3-13 Ca <sup>2+</sup> enters from the base of cilia following ATP stimulation .....	47
Figure 3-14 5HT <sub>6</sub> -CFP-Venus(H148G) detects no change in ciliary pH in response to ATP.....	48
Figure 3-15 5HT <sub>6</sub> -mCherry-G-GECO1.0 detects ciliary Ca <sup>2+</sup> fluxes in response to laminar flow.....	50
Figure 3-16 Laminar fluid flow induces dynamic calcium signals in primary cilia .....	52
Figure 3-17 Quantification of 5HT <sub>6</sub> -mCherry-G-GECO 1.0 activity in primary cilia under flow	53
Figure 4-1 PI(4)P and PI(4,5)P <sub>2</sub> are present in distinct ciliary compartments regulated by Inpp5e .....	81
Figure 4-2 Model of the role of ciliary phosphoinositides in Hh signaling .....	84
Figure 4-3 Growth stimulation induces ciliary vesicle release regulated by Inpp5e .....	85
Figure 4-4 Characterization of cilia decapitation and <i>Inpp5e</i> <sup>+/-</sup> and <i>Inpp5e</i> <sup>-/-</sup> MEF .....	88
Figure 4-5 Growth stimulation regulates ciliary Inpp5e and PI(4,5)P <sub>2</sub> localization.....	91
Figure 4-6 AurA-dependent ciliary Inpp5e depletion re-organizes ciliary PI(4,5)P <sub>2</sub> .....	94
Figure 4-7 Ciliary PI(4,5)P <sub>2</sub> induces intraciliary F-actin assembly which executes cilia decapitation.....	97
Figure 4-8 PI(4,5)P <sub>2</sub> regulates ciliary localization of F-actin, actin regulatory proteins and small GTPases .....	100
Figure 4-9 F-actin and SNX9 localize in primary cilia prior to decapitation .....	103

Figure 4-10 Global proteomic profiling of conditioned culture media reveals growth-stimulated extracellular release of IFT-B dependent on primary cilia.....	106
Figure 4-11 Experimental scheme for ciliary vesicle proteomic profiling and analyses of ciliary IFT distribution .....	108
Figure 4-12 Inhibition of cilia decapitation suppresses growth-stimulated cilia disassembly.....	111
Figure 4-13 Cilia decapitation occurs in G <sub>0</sub> and regulates G <sub>1</sub> phase entry .....	113
Figure 4-14 Time-lapse measurements of nuclear Venus-p27K <sup>-</sup> /mCherry-hCdt1(30/120) signal intensity ratios under growth stimulation .....	116
Figure 4-15 Growth-induced Gli activation is dependent on cilia decapitation .....	118
Figure 5-1 Effect of Inpp5e on basal cellular and ciliary [Ca <sup>2+</sup> ] and pericentriolar localization of calmodulin.....	136



# Chapter 1 Introduction

As embryos grow, cells continuously detect and process environmental signals which instruct them to survive, function and propagate into specific tissue organization (Perrimon et al., 2012). To help accomplish these remarkable signaling feats, vertebrates develop primary cilia to function as specialized sensory antennae on the cell surface (**Figure 1-1**) (Goetz and Anderson, 2010). In mouse embryos, primary cilia appear as early as embryonic day six in pluripotent embryonic cells, but are suppressed in cells that give rise to extra-embryonic tissues (Bangs et al., 2015). Overall embryo patterning requires functional primary cilia (Babu and Roy, 2013; Goetz and Anderson, 2010). Being present on virtually all cell types in the body (Marshall and Nonaka, 2006), primary cilia also possess specific sensory roles in tissues such as the kidney and retina (Berbari et al., 2009). Consequently, defects to primary cilia result in diverse forms of developmental disorders collectively known as ciliopathies (Hildebrandt et al., 2011). In adults, dysregulation of ciliary signaling is also associated with tumorigenesis (Han et al., 2009; Wong et al., 2009). Understanding the principles of ciliary signaling is thus pivotal to developing strategies to treat cilia-related disorders.

## 1.1 Primary cilia structural and functional architecture

### 1.1.1 Overall structure

Primary cilia are solitary hair-like structures that protrude from the plasma membrane into the extracellular space. Depending on cell type, primary cilia typically range between 1 and 9  $\mu\text{m}$  in length and measure 200nm in diameter (Dummer et al., 2016; Phua et al., 2015). While an average cell consists of several picoliters in volume, the volume of a single primary cilium lies in the range of 0.1 femtoliters (Phua et al., 2015). In tubular organs such as the kidney, primary cilia are generally positioned on the apical surface of polarized epithelial cells and exposed to the tissue lumina (Zhang et al., 2004). In connective tissues and some epithelial cell types, can harbor

primary cilia can be harbored on either the dorsal or ventral surface of non-polarized cells when adherent in culture (Kukic et al., 2016; Phua et al., 2017). The membrane covering the primary cilium, known as the ciliary membrane, is continuous with the plasma membrane. Despite the contiguity, the ciliary membrane is selectively enriched with a complement of receptors, ion channels and catalytic enzymes that are different from the plasma membrane, signifying discrete signaling functions (**Figure 1-1**) (Marshall and Nonaka, 2006; Phua et al., 2015; Singla and Reiter, 2006). A transition zone located at the proximal ciliary base consists of Y-shaped linkers between the ciliary membrane and cytoskeleton proposed to restrict lateral diffusion between the plasma and ciliary membranes (Reiter et al., 2012) (**Figure 1-1**). The ciliary membrane does not enclose the organelle, and this creates a passage for soluble flux between the ciliary lumen and the main cell body. The ciliary cytoskeleton, or axoneme, consists of nine microtubule doublets emanated from the basal body, which is an adapted mother centriole tethered to the plasma membrane (**Figure 1-1**) (Hoey et al., 2012).

### 1.1.2 Ciliary receptors

Primary cilia are equipped with specialized trafficking machinery that transports a specific collection of transmembrane receptors to the ciliary membrane (Nachury et al., 2010). Ciliary receptors fall under three categories, namely the morphogen receptors, G-protein coupled receptors (GPCRs) and receptor tyrosine kinases (RTKs) (**Figure 1-1**) (Christensen et al., 2012; Satir et al., 2010; Singla and Reiter, 2006). The roles of primary cilia in embryogenesis are partly attributed to the ciliary enrichment of receptors which sense Hedgehog (Hh) and Notch morphogens during tissue patterning processes (Ezratty et al., 2011; Goetz and Anderson, 2010). In vertebrates, Hh signaling begins in primary cilia; extracellular Hh ligand binds to cilia-localized Patched1 (Ptch1) receptor and induces ciliary exit to permit Smoothened (Smo) entry (Rohatgi et al., 2007). Ciliary accumulation of Smo activates the Hh signaling cascade which ultimately leads to the processing of the Gli transcription factors into their activator forms. Gli

transcription factors are established regulators of genes related to cell proliferation and differentiation (Hui and Angers, 2011). Primary cilia are further implicated in cell fate decisions owing to an enrichment of receptors for various growth factors such as PDGF and IGF (Christensen et al., 2012; Yeh et al., 2013). In the developing neocortex, IGF-1 signaling in the primary cilia regulates neuronal differentiation (Yeh et al., 2013). In addition, primary cilia host GPCRs for hormones, such as serotonin and somatostatin, and regulate the development and function of neuronal cells (Schou et al., 2015). Orphan GPCRs such as Gpr161 are also components of primary cilia, and recent studies have elucidated their roles as cilia-specific Hedgehog signaling regulators (Mukhopadhyay et al., 2013).

### 1.1.3 Ciliary ion channels

Several  $\text{Ca}^{2+}$ -permeable channels from the transient receptor potential (TRP) superfamily have been detected in primary cilia to date, namely TRPC1, TRPP2, TRPP3 and TRPV4 (**Figure 1-1**) (Bai et al., 2008; Delling et al., 2013; Köttgen et al., 2008; Yoder et al., 2002). TRP channels are generally characterized with polymodal activation properties that implicate them in a broad range of functions (**Table 1-1**) (Gees et al., 2010; Zheng, 2013). This is best demonstrated by TRPV4, which is concomitantly activated by chemical, mechanical and heat stimuli (Vriens et al., 2004). Similarly, TRPC1 is a mechanosensitive channel that also acts downstream of GPCR- or RTK-regulated phospholipase C- $\beta/\gamma$  (Abramowitz et al., 2007; Maroto et al., 2005). Whilst TRPP2 and TRPP3 display low constitutive levels of channel activity at basal state (Giamarchi and Delmas, 2007; Shimizu et al., 2009), it is thought that TRPP2 could co-assemble with non-pore forming polycystic kidney disease 1 (PKD1) and polycystic kidney disease 1 like 1 (PKD1L1) proteins to form mechanosensitive ion channel complexes (Nauli et al., 2003; Yoshida et al., 2012). Collectively, ciliary localization of these TRP channels could endow primary cilia with polymodal sensitivity. Moreover, the intrinsic signaling properties of primary cilia could modulate the activity of resident TRP channels to generate local  $\text{Ca}^{2+}$  signals distinct from the rest

of the cell body (Phua et al., 2015). The significance of such bi-directional functional regulation between the ciliary TRP channels and primary cilia is underscored by developmental defects associated with the TRP channel functional loss (Delling et al., 2013; Field et al., 2011; Yoshida et al., 2012; Zhou, 2009). Yet, the nature of ciliary  $\text{Ca}^{2+}$  signals has remained an elusive subject.

#### **1.1.4 Ciliary phosphoinositide metabolic enzymes**

Inpp5e, Inpp5b and OCRL are phosphoinositide 5-phosphatases that reside in primary cilia of a variety of tissue types (Bielas et al., 2009; Jacoby et al., 2009; Luo et al., 2012, 2013). Depending on substrate availability, these enzymes are able to catalyze the conversion of  $\text{PI}(3,4,5)\text{P}_3$  and  $\text{PI}(4,5)\text{P}_2$  into  $\text{PI}(3,4)\text{P}_2$  and  $\text{PI}(4)\text{P}$  respectively (Rudge and Wakelam, 2017). Loss-of-function of Inpp5e accelerates cilia disassembly and implicates phosphoinositides in primary cilia stability (Bielas et al., 2009; Jacoby et al., 2009). In addition, OCRL and Inpp5b have been implicated in proper cilia formation (Luo et al., 2012, 2013). On the contrary, PIPKI $\gamma$ , a phosphoinositide 5-kinase isoform which catalyzes the reverse conversion of  $\text{PI}(4)\text{P}$  into  $\text{PI}(4,5)\text{P}_2$ , has been recently reported to reside at the basal body and is entailed in ciliogenesis (Xu et al., 2016). The association of primary cilia with these phosphoinositide metabolic enzymes suggests that the ciliary membrane lipid composition could be altered differently from the plasma membrane. Of note,  $\text{PI}(4,5)\text{P}_2$  is a major molecular identifier of the plasma membrane, where it recruits  $\text{PI}(4,5)\text{P}_2$ -binding actin regulators to modulate actin polymerization at the cell cortex required to drive almost all membrane processes on the cell surface (Saarikangas et al., 2010). As such, the nature of phosphoinositide metabolism in the ciliary membrane could affect actin polymerization within primary cilia. This is supported by the general absence of actin filaments in primary cilia (Francis et al., 2011), in contrast with other F-actin-based membrane protrusions such as filopodia (Mattila and Lappalainen, 2008). Nevertheless, the phosphoinositide composition in mammalian

ciliary membrane has not been characterized, and it is uncertain how phosphoinositides could regulate the structure and function of primary cilia.

### **1.1.5 Ciliary intraflagellar transport**

The composition of primary cilia is regulated by a sophisticated microtubule motor system known as the intraflagellar transport (IFT) (Rosenbaum and Witman, 2002). The IFT system comprises of two associated large protein complexes IFT-A and IFT-B, of which individual components possess binding specificity for various ciliary components (Lechtreck, 2015). The microtubule plus-end kinesin II motor binds with the IFT-B complex, and is responsible for the anterograde IFT transport into cilia (Rosenbaum and Witman, 2002). In contrast, retrograde IFT transport out of cilia is achieved by the microtubule minus-end cytoplasmic dynein 2 motor, which associates with IFT-A (Rosenbaum and Witman, 2002). Hence, the trafficking of IFT-B and IFT-A complexes along ciliary axoneme are respectively associated with the transport of contents into and out of primary cilia. Intraflagellar transport helps to regulate and maintain signaling receptors and effectors in cilia at steady state (Ishikawa and Marshall, 2011). Genetic perturbation to IFT components upset ciliary composition and growth, thereby resulting in aberrant signaling within primary cilia (Mourão et al., 2016).

## **1.2 The capabilities of primary cilia as sensory antennae**

In a tissue environment with fluid movements, such as the lumina of blood vessels or kidney tubules, fluids slow down or become static on the cell surface due to contact friction with the plasma membrane (Freund et al., 2012). Such non-uniform motion could result in an uneven mixing of receptor ligands in proximity with the cell surface. Moreover, the charged membrane lipids on cell surface as well as the presence of glycocalyx could influence the distribution of ligands in the immediate fluid environment above the cell surface (Novak, 1997; Reitsma et al.,

2007). Hence, the projection of primary cilia away from the cell surface could equip cells with more accurate assessment of their local environment (Marshall and Nonaka, 2006).

The cantilever-like structure of primary cilia is also an ideal design to sense flow mechanics (Hoey et al., 2012). Indeed, primary cilia have been proposed to sense urine flow in the kidney and the nodal flow in the embryonic node through flow-induced bending (see Section 1.4). The flexural rigidity of primary cilia of these cells are optimal for detecting changes in flow shear stress within a physiological range through corresponding changes in flow-induced bending angle (Hoey et al., 2012; Rydholm et al., 2010; Schwartz et al., 1997; Young et al., 2012). Interestingly, the flexural rigidity of the kidney primary cilia is also non-uniform along the axoneme, with the proximal part of the ciliary shaft stiffer than the distal segment (Hoey et al., 2012; Rydholm et al., 2010; Young et al., 2012). The higher stiffness of the proximal ciliary shaft may be crucial to keep the kidney primary cilia upright, and sensitize the cantilever-like structure to small variations in the luminal flow rate. This is in contrast with primary cilia in other cell types such as fibroblasts and retinal pigment epithelial cells, where the ciliary shafts are generally positioned more parallel with the cell surface. Interestingly, fluid shear forces on the ciliary membrane is thought to be sensed by mechanosensitive TRP channels residing in ciliary membrane (Nauli et al., 2003; Praetorius and Spring, 2001).

Primary cilia also possess a much higher surface area to volume ratio as compared with the rest of the cell body. This could allow a few number of activated receptors on ciliary membrane to induce a high local concentration of downstream signaling messengers which regulate signaling in the periphery (Marshall and Nonaka, 2006), making each primary cilium a highly robust sensor device. Once diffused into the cytosol, these signaling messengers will encounter a sharp decrease in their effective concentration (Delling et al., 2013); this may serve as an effective way to spark off highly localized and acute signaling events in the cilia-centrosome region without influencing activities in the rest of the cell.

The co-enrichment of receptors and ion channels in the ciliary membrane also establishes a unique platform for molecular crosstalk (Phua et al., 2015). Whilst TRP proteins generally assemble into homo-tetrameric ion channels, the co-presence of different TRP sub-families may promote them to associate into assemblies of novel molecular stoichiometry that possess gating and regulatory properties distinct from the homomeric channels (**Table 1-1**).

Finally, the absence of actin cortex in primary cilia (Francis et al., 2011) could modulate ciliary signaling dynamics differently from the plasma membrane. The actin cortex that underlies cell membrane plays a fundamental role in organizing transient nanoscale signaling assemblies on the cell membrane. Several models have been proposed to explain the phenomenon, including tethering between cortical actin filaments and cytosolic domains of transmembrane proteins and regulation of membrane lipid clustering through actin binding proteins (Kusumi et al., 2012; Viola and Gupta, 2007). This actin-dependent membrane organization is proposed to execute precise control over the strength, kinetics and spatiotemporal localization of cell membrane signals (Grecco et al., 2011). The lack of actin cortex underlying the ciliary membrane thereby suggests that the receptor and ion channel organization could be discrete from that of the surrounding plasma membrane. This could be reinforced by the enrichment of various phosphoinositide metabolic enzymes in primary cilia which could result in a distinct ciliary membrane composition (Jacoby et al., 2009; Luo et al., 2013; Xu et al., 2016). Altogether, we may expect divergent signaling outputs from these two separate compartments, despite utilizing the same ion channel or receptor.

### **1.3 Coupling between the cilia life cycle and the cell-division cycle**

Ciliary signaling that regulates cell proliferation and differentiation could act at the level of cell cycle control. Genetic studies have revealed a connection between cilia stability and cell cycle progression; unstable primary cilia are associated with shorter G<sub>1</sub>-S transit time (Jacoby et al., 2009), and the reverse has been observed in cells with longer cilia (Kim et al., 2011). The

assembly and disassembly processes of primary cilia are also tightly coupled with the cell cycle; cilia assemble in non-dividing cells of G<sub>0</sub>/G<sub>1</sub> phases, and disassemble prior to mitotic entry (Ishikawa and Marshall, 2011; Plotnikova et al., 2009). Indeed, the cilia life cycle and cell-division cycle are two tightly enmeshed processes, and this emphasizes the relevance to determine the underlying molecular mechanism. While much is known about ciliogenesis (Ishikawa and Marshall, 2011), current literature does not explain how the steady-state ciliary structure is insulated from contiguous dynamic membrane processes occurring on the cell surface, such as endo/exocytosis and membrane ruffling, to function as a stable signal transduction apparatus.

Primary cilia disassemble via gradual resorption of ciliary material into the cell body (Plotnikova et al., 2009). Aurora A kinase (AurA), a master regulator of cilia disassembly, induces cilia resorption partly via histone deacetylase 6 (HDAC6)-dependent deacetylation of ciliary microtubules, which destabilizes the axoneme (Pugacheva et al., 2007). The dynamics of cilia disassembly process, however, has not been visualized in detail. Interestingly, *Chlamydomonas* flagella has been shown to disassemble via excision and release into the extracellular environment, in response to environmental stress such as high acidity (Pan et al., 2004). Recent reports suggest that vertebrate primary cilia could possess similar capacity in releasing vesicles into the extracellular environment (Dubreuil et al., 2007; Wood and Rosenbaum, 2015). While monitoring primary cilia of cycling kidney fibroblasts, Paridaen et al. occasionally observed release of vesicular structures from distal cilia (Paridaen et al., 2013). Active release of ciliary contents was also observed in retinal pigment epithelial cells over-expressing a CEP162 mutant (Wang et al., 2013). Furthermore, extracellular vesicles were closely apposed with tip-dilated primary cilia in cystic kidneys of *Inpp5e* mutant mice (Jacoby et al., 2009), suggesting a connection between phosphoinositides and extracellular vesicle formation. Together, these evidence supports the notion that primary cilia undergo vesicle release under



specific conditions, and this process could be involved in cilia disassembly during cell cycle entry.

#### **1.4 Developmental roles of primary cilia**

The effects of ciliary signaling at the single cell level scale up to regulate tissue morphogenesis in the developing embryo (Goetz and Anderson, 2010). Left-right determination in the mammalian early embryo is initiated at the embryonic node, a pit-like structure where a leftward fluid flow generated by motile cilia of the central nodal cells elicits left-right asymmetric gene expression in lateral crown cells surrounding the embryonic node (Nakamura and Hamada, 2012; Nonaka et al., 2002). One long-standing model proposes that the primary cilia of crown cells could serve as mechanical flow sensors to the nodal flow (Babu and Roy, 2013). Interestingly, TRPP2 ion channel residing in crown cell primary cilia is also required to establish asymmetric gene expression at the embryonic node (Yoshida et al., 2012). This has led to a compelling hypothesis that TRPP2 could constitute part of a molecular mechanosensory complex which detects flow-induced primary cilia deformation to activate calcium-dependent asymmetric gene expression (Yoshida et al., 2012). Similar roles have also been ascribed for primary cilia and TRPP2 in the kidney. Urine flow within the kidney occurs with periodic oscillation in flow rates proposed to be regulated by the tubuloglomerular feedback mechanism (Kang et al., 2006; Rosivall et al., 2006). TRPP2 and PKD1 have been proposed to form a mechanosensory ion channel complex in kidney primary cilia, and activation of this ion channel complex could result in downstream calcium signals which regulate cell proliferation and/or the plane of cell division for normal kidney tubule development (Zhou, 2009). The apparent role of ciliary TRPP2 channels in these developmental systems stresses the relevance to understand calcium signals originating from primary cilia.

Primary cilia also serve as chemosensory antennae in the dorsal-ventral patterning of the neural tube, which gives rise to the vertebrate brain and spinal cord (Goetz and Anderson, 2010). Ventral specification of the neural tube depends on the Sonic Hedgehog (Shh) protein; the

notochord positioned at the ventral side of the neural tube secretes Shh ligand into the external environment to establish a morphogen concentration gradient that is the strongest at the ventral floor plate of the neural tube (Gilbert, 2000). Neural progenitor cells at this development stage possess primary cilia which help to sense the local Shh concentration depending on their position in the neural tube (Sasai and Briscoe, 2012). Depending on the strength of Shh signals, specific combinations of transcription factors gets induced, which specifies the neural cell identity (Gilbert, 2000). Primary cilia similarly serve as specialized Shh-sensory antennae in vertebrate limb development (Goetz and Anderson, 2010).

Besides organizing the body plan, primary cilia is also involved in epidermal differentiation during skin development by hosting Notch receptor signaling (Ezratty et al., 2011). By regulating the balance between canonical and non-canonical Wnt signaling, primary cilia also have suggested roles in planar cell polarity (Lancaster et al., 2011). Overall, primary cilia serve as nexuses for signaling pathways during development.

## **1.5 Ciliopathies and cancer**

Due to the ubiquitous presence of primary cilia in vertebrate tissues, genetic defects of ciliary components manifest as multi-system developmental disorders collectively known as ciliopathies (Hildebrandt et al., 2011; Tobin and Beales, 2009). Depending on the function of the ciliary component in question and the type of mutation, each form of ciliopathy could include a combination of the following defects, namely situs inversus (laterality defect), polydactyly, corpus callosum agenesis (brain deformation), encephalocoele (a lethal neural tube defect in which the brain protrudes through the skull), cystic kidneys, hepatobiliary disease, retinal degeneration, anosmia, obesity and skeletal bone defects (Hildebrandt et al., 2011; Tobin and Beales, 2009). While laterality defects highlight the role of cilia in defining left-right body organization (Babu and Roy, 2013; Nakamura and Hamada, 2012), polydactyly and brain deformation frequently co-exist in ciliopathies due to the common role of ciliary Hh signaling in

limb and brain development (Goetz and Anderson, 2010; Tobin and Beales, 2009). For instance, mutations in the cilia-enriched *Inpp5e* result in the Joubert syndrome that could encompass an abnormal number of digits and mid-brain malformation which display a molar tooth-like morphology, suggesting a role for *Inpp5e* in regulating Hh signaling (Travaglini et al., 2013).

Cyst formation in the kidney is one of the most prominent features of ciliopathies, which highlights the essentiality of ciliary signaling in the kidney (Tobin and Beales, 2009). Autosomal dominant polycystic kidney disease, which affects 1 in 1000 in the population, is caused by genetic mutations of *TRPP2* and *PKD1*, which are commonly implicated in tubular formation and maintenance through a yet-determined mechanism in primary cilia (Hildebrandt et al., 2011; Torres et al., 2007). Primary cilia specialization in the photoreceptors (connecting cilia) and olfactory neurons (sensory cilia) have also led to vision and smell defects as features of ciliopathies (Hildebrandt et al., 2011; Tobin and Beales, 2009).

Besides developmental disorders, aberrant primary cilia and ciliary signaling are linked with tumorigenesis in adults (Hassounah et al., 2012; Seeger-Nukpezah et al., 2013). Hh signals acts as a potent mitogen in several tissue types in our body through expression of genes that drive cell proliferation (Roy and Ingham, 2002). Though Hh signals are sensed by the primary cilia, primary cilia serve opposing roles in downstream Hh signaling, as they are required for the formation of Gli activators as well as repressors which respectively promote or suppress expression of Hh target genes (Han et al., 2009; Toftgard, 2009; Wong et al., 2009). Thus, primary cilia are predominantly present in Hh signal-dependent cancers such as basal cell carcinoma, but are absent in other types of cancer where the presence of cilia would restrict the abnormal activation of mitogenic Hh signaling (Hassounah et al., 2012; Toftgard, 2009). In addition, the link between cilia stability and cell cycle dynamics suggests that tumorigenic roles of primary cilia could be further attributed to other forms of ciliary signaling (e.g. RTK signaling) that could modulate the balance between cell proliferation and differentiation. Understanding the

regulatory crosstalk between primary cilia and cell cycle thus holds much physiological and clinical significance.

## **1.6 Specific aims**

Whilst genetic studies have established a close association between primary cilia and vertebrate embryo development, knowledge on ciliary signaling molecular mechanisms and how they regulate cellular functions is still in its infancy. The evolution of vertebrates to confine various developmental signaling pathways within this tiny organelle is also of much interest to basic scientists. To enlighten ourselves to these questions, it is of prime importance to understand the nature of signaling within primary cilia. Specifically, we need to elucidate how the exclusive antennae-like capabilities of primary cilia (Section 1.2) could tune the dynamic behavior of signaling entities to produce functions unique from the rest of the cell. This could be especially applicable to small signaling messengers such as  $\text{Ca}^{2+}$  ions and  $\text{PI}(4,5)\text{P}_2$  phospholipid which participate in diverse cellular functions depending on their spatiotemporal localization (Clapham, 2007; Gamper and Shapiro, 2007). Indeed, genetics studies have revealed roles of  $\text{Ca}^{2+}$  and  $\text{PI}(4,5)\text{P}_2$  in the stability and sensory modalities of primary cilia (Jacoby et al., 2009; Nauli et al., 2003). However, the 10,000-fold volumetric difference between the solitary primary cilium and the cell body has hampered the use of conventional imaging methods to resolve ciliary signaling events from the rest of the cell. Moreover, genetic and chemical perturbations act at the whole-cell level and frequently culminate in non-specific effects which complicate the interpretation of ciliary functions. Exploiting the live-cell fluorescence imaging and molecular engineering expertise of the Inoue laboratory, I will develop molecular sensor and actuator technology to visualize and/or manipulate  $\text{Ca}^{2+}$  and  $\text{PI}(4,5)\text{P}_2$  to probe their spatiotemporal dynamics and functional roles in the primary cilia. This will be divided into two specific aims that are addressed in Chapters 3 and 4 of this dissertation:

Specific aim 1: Develop genetically-encoded cilia-targeted calcium indicators for illumination of calcium signals in primary cilia.

We explore different combinations of ciliary targeting sequences and calcium biosensors to engineer genetically-encoded cilia-targeted calcium indicators. We then use these molecular sensors to reveal ciliary calcium signals in response to chemical and mechanical stimulation.

Specific aim 2: Defining the roles of phosphoinositides in the structure and function of primary cilia.

We first characterize the phosphoinositide composition of primary cilia, and determine a mechanism for molecular regulation. We use genetic methods and molecular actuators to perturb the phosphoinositide composition of primary cilia, and reveal their roles in regulating the structure and signaling properties of cilia. Finally, we develop insight into the roles of ciliary phosphoinositides in regulating cellular function, specifically in cell cycle progression.

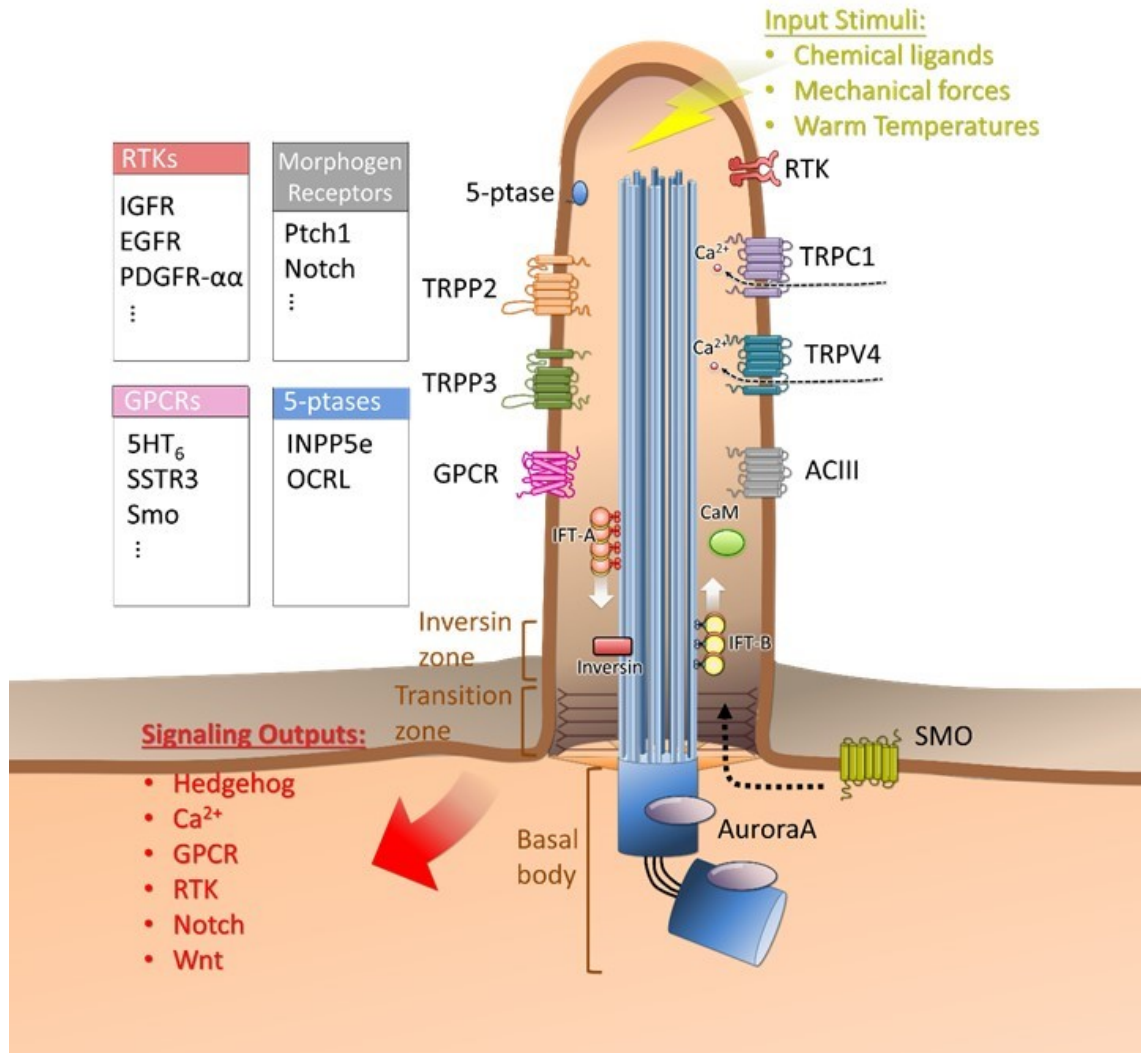


**Figure 1-1. Primary cilia structural and functional architecture.**

Primary cilia harbor diverse signaling components to function as polymodal sensory organelles. The intraflagellar transport (IFT) machinery is a cilia-specific trafficking machinery that regulates anterograde (IFT-B) and retrograde (IFT-A) transport within the cilium. RTK: receptor tyrosine kinase (EGFR: epithelial growth factor receptor; PDGFR- $\alpha$ : platelet-derived growth factor receptor  $\alpha$  homodimer; IGFR: insulin-like growth factor receptor); morphogen receptors (Ptch1: Patched 1 receptor for Hedgehog ligands; Notch: Notch receptor); GPCR: G-protein coupled receptor (5HT<sub>6</sub>: serotonin receptor isoform 6; SSTR3: somatostatin receptor isoform 3; Smo: smoothened); 5-ptase: phosphoinositide 5-phosphatase (Inpp5e: inositol polyphosphate-5-

phosphatase; OCRL: Lowe oculocerebrorenal syndrome protein); CaM: Calmodulin. Adapted from (Phua et al., 2015).

**Table 1-1. A non-exhaustive list of gating stimuli and regulators for each cilia-residing TRP channel.**

Reported co-assembly partners for respective TRP channels are also listed in the right column together with associated function. Note that these are mostly determined via whole cell studies, and their specific effect within primary cilia requires further elucidation. Adapted from (Phua et al., 2015).

TRP channels detected in primary cilium	Gating stimuli (direct/indirect)	Channel activity regulators and interacting partners	Heteromeric co-assembly partners and associated function
<b>TRPC1</b>	Direct membrane stretch Intracellular $\text{Ca}^{2+}$ store depletion Gq-coupled GPCR/PLC $\beta$ RTK/PLC $\gamma$ Nitric oxide	IP $_3$ R Phosphorylation by PKC, PKG $\text{Ca}^{2+}$ -Calmodulin STIM1 MARCKS PI(4,5)P $_2$	TRPP2: Gq-coupled GPCR/PLC $\beta$
<b>TRPP2</b>	Displays some constitutive activity Direct $\text{Ca}^{2+}$ activation Triptolide Voltage (positive potential) EGF	Microtubule kinesin motors Actin-binding proteins IP $_3$ R EGFR PLC- $\gamma$ 2 PACS-1-2 Phosphorylation by casein kinase 2, glycogen synthase kinase (GSK)-3, protein kinase D [ $\text{Ca}^{2+}$ ] PI(4,5)P $_2$	PKD1: Fluid flow PKD1L1: Fluid flow
<b>TRPP3</b>	Displays some constitutive activity Direct $\text{Ca}^{2+}$ activation Hypo-osmotic cell swelling Voltage (repolarization after depolarization) Warm temperatures	[ $\text{Ca}^{2+}$ ] Actin-binding proteins [H $^+$ ] RACK1	PKD1L1: ATP purinergic signaling; warm temperatures; displays constitutive activity?
<b>TRPV4</b>	Hypo-osmotic cell swelling Fluid flow Warm temperatures (threshold: 27–35°C) Phorbol esters Arachidonic acids and metabolites	Phosphorylation by PKC, PKA, Src tyrosine kinase $\text{Ca}^{2+}$ -Calmodulin PI(4,5)P $_2$ MAP7 PACIN3	TRPP2: Fluid flow; warm temperatures TRPC1: Fluid flow



## Chapter 2 Earlier work

During the pre-candidate phase of my graduate training, I co-developed a synthetic actuator system based on the rapamycin-dependent FKBP.FRB dimerization system for rapid inducible trapping of cytoplasmic protein probes in primary cilia. This system empowered us with an unprecedented ability to measure protein trafficking kinetics in primary cilia of living cells, and to determine a sieve-like diffusion barrier positioned at the ciliary base which regulates soluble flux between the cilia and cytosol (Lin et al., 2013). Whilst such chemically inducible synthetic systems are powerful approaches to dissect complex spatiotemporal signaling in cells, overexpression of protein actuator probes freely in the cytosol often results in elevated background activity prior to chemical induction, which perturbs the cellular basal state and thereby limits their wide application. As a fundamental solution, we rationally designed and developed a strategy to remove unwanted background activity without compromising the extent of induced activation. By exploiting interaction between a membrane lipid and its binding protein, target proteins were translocated from one organelle to another on a time scale of seconds. We demonstrated that this improved strategy allows for rapid manipulation of small GTPases under a physiological state, thus enabling fine dissection of sophisticated signaling processes shaped by these molecules (Phua et al., 2012).

# **Chapter 3 Genetically encoded calcium indicator illuminates calcium dynamics in primary cilia**

## **3.1 Overview**

Conventional calcium signal measurement methods encounter limitations when applied to primary cilia. An electrophysiological method to measure signals in primary cilia has been previously reported (Kleene and Kleene, 2012), but the sub-micrometer size of this organelle makes patch-clamping the ciliary membrane difficult. Synthetic  $\text{Ca}^{2+}$  indicator dyes allow the monitoring of multiple cells but often result in signal saturation of the entire cytosol that overwhelms local transient  $\text{Ca}^{2+}$  fluxes in specific subcellular compartments (**Figure 3-1**). Here we develop a strategy to specifically target genetically encoded  $\text{Ca}^{2+}$  indicators (GECIs) into primary cilia to distinguish cilia-specific  $\text{Ca}^{2+}$  signaling from that of the main cell body (Su et al., 2013). We then use these molecular sensors to reveal ciliary calcium signals in response to ATP stimulation and laminar flow stimulation in an enclosed chamber. The successful development of these cilia-targeted GECIs opens a possibility to understand the significance of calcium signaling in cilia physiology.

## **3.2 Results**

### **3.2.1 Construction and characterization of cilia-targeted genetically encoded calcium indicators**

We first evaluated a collection of ciliary targeting sequences (CTSs) (Nachury et al., 2010), which included two truncated peptides derived from the cytoplasmic tail of fibrocystin (CTS20 and CTS68), full-length 5- hydroxytryptamine (serotonin) receptor isoform 6 (5HT<sub>6</sub>), a fusion peptide consisting of the transmembrane domain of integrin  $\beta$ 1 and the C-terminal domain of

Arl13b (integrin-Arl13b; IA) as well as a 5HT<sub>6</sub>-CTS20 combination. We tagged each CTS with GFP and evaluated these constructs for targeting efficiencies and effects on cilia morphology (**Figures 3-2 and 3-3**). 5HT<sub>6</sub>-GFP and IA-GFP demonstrated high cilia-targeting efficiencies of 87% (131/150 GFP-expressing cells) and 85% (146/172 GFP-expressing cells), respectively (**Figures 3-2A and 3-3E,G**). None of the CTSs tested had an obvious effect on ciliation frequency, indicating that overexpression of CTSs in cells did not adversely affect ciliogenesis (**Figure 3-2B**). Expression of 5HT<sub>6</sub>-GFP and IA-GFP, however, caused the average length of primary cilia to increase approximately twofold, (**Figure 3-2C**) and correlated with a higher frequency of morphological deformations (**Figures 3-2D and 3-4**). Nevertheless, the bulk of primary cilia expressing these two constructs exhibited regular morphology. Transmission electron microscopy and immunofluorescence studies of 5HT<sub>6</sub>-expressing primary cilia demonstrated no obvious defects in cilia ultrastructure as well as normal localization of key ciliary proteins (**Figures 3-5 and 3-6**).

We next fused these CTSs with currently available GECIs, including intramolecular CFP and YFP fluorescence resonance energy transfer (FRET) indicators TNXXL (Mank et al., 2008) and YC3.60 (Horikawa et al., 2010), as well as single fluorescence GFP indicators G-CaMP5G (Akerboom et al., 2012) and G-GECO1.0 (Zhao et al., 2011) (**Table 3-1**). We characterized the cilia-targeting efficiency and signal dynamic range of each CTS-tagged GECI (Figures 3-7, 3-8 and 3-9). 5HT<sub>6</sub>-G-GECO1.0 (**Figure 3-10A**) demonstrated the greatest potential as a cilia-specific Ca<sup>2+</sup> indicator and was comparable with 5HT<sub>6</sub>-GFP in cilia-targeting efficiency, ciliation efficiency and effects on ciliary structure (**Figures 3-2, 3-3, 3-4 and 3-10B**). At the basal state, 5HT<sub>6</sub>-G-GECO1.0 displayed weak GFP fluorescence in primary cilia but exhibited an increase of 360.0% ± 62.1% (± s.e.m., *n* = 13 cells) in GFP fluorescence when stimulated with 2 μM ionomycin (**Figures 3-9A, 3-10C, and Table 3-1**). All subsequent experiments were conducted with 5HT<sub>6</sub>-G-GECO1.0.

### 3.2.2 Ciliary calcium responses to chemical stimulation

ATP triggers increases in cellular calcium levels via the activation of ATP-gated P2X calcium-permeable channels and/or G protein-coupled P2Y receptors, which induce the mobilization of intracellular  $\text{Ca}^{2+}$  from inositol 1,4,5-trisphosphate-sensitive stores. We therefore investigated whether ciliary  $\text{Ca}^{2+}$  changes could be detected in response to ATP stimulation. Through the co-expression of cytosolic R-GECO1 (a single red fluorescent GECI (Zhao et al., 2011)) and cilia-targeted 5HT<sub>6</sub>-G-GECO1.0 in NIH-3T3 cells, we detected a pronounced rise in cytosolic  $\text{Ca}^{2+}$  that was accompanied by a comparable increase in ciliary  $\text{Ca}^{2+}$  in 52.2% (12/23) of cells stimulated by 10  $\mu\text{M}$  ATP (**Figure 3-11A**). We observed an average maximum increase of  $53.9\% \pm 20.4\%$  ( $\pm$  s.e.m.,  $n = 11$  cells) and  $54.3\% \pm 10.0\%$  ( $\pm$  s.e.m.,  $n = 11$  cells) in fluorescence intensity in the cilia and the cytosol, respectively (**Figure 3-10A**). In contrast, vehicle control did not generate any  $\text{Ca}^{2+}$  response in the cytosol and primary cilia (**Figures 3-11B and 3-12B**). To determine the source of observed ciliary  $\text{Ca}^{2+}$  fluxes, we increased our imaging frequency from 0.067 Hz to 0.63 Hz. We observed that spikes in cytosolic  $\text{Ca}^{2+}$  clearly preceded ciliary  $\text{Ca}^{2+}$  spikes in 100% (14/14) of cells (**Figures 3-11C and 3-12C**). The average delay time between the cytosolic and ciliary  $\text{Ca}^{2+}$  elevation was  $6.04 \text{ s} \pm 0.98 \text{ s}$  ( $\pm$  s.e.m.;  $n = 14$  cells). Consistent with this, whenever we detected  $\text{Ca}^{2+}$  oscillations in the cytosol, we also observed correlated but delayed calcium spikes in the cilia (**Figures 3-11C and 3-12C**). Furthermore, ciliary  $\text{Ca}^{2+}$  fluxes propagated in a base-to-tip direction in the ciliary lumen in 100% (14/14) of ATP-induced ciliary  $\text{Ca}^{2+}$  spikes detected (**Figure 3-13**). Collectively, these observations suggest that the ciliary  $\text{Ca}^{2+}$  flux originates from the calcium stores in the cytosol. However, we cannot exclude other possibilities such as a contribution of ATP-gated P2X calcium-permeable channels localized at the base of primary cilia. By further increasing the imaging frequency to 1.5 Hz, we calculated the linear rate of  $\text{Ca}^{2+}$  propagation along the ciliary shaft to be  $0.83 \pm 0.22 \mu\text{m/s}$  ( $\pm$  s.d.) in cilia where the  $\text{Ca}^{2+}$  propagated the entire length of the lumen ( $n = 11$  cells). Of note, these numbers

could be at least partially affected by buffering effect from overexpressed 5HT<sub>6</sub>-G-GECO1.0. Because GFP-based GECIs are sensitive to changes in pH (Mank and Griesbeck, 2008), we confirmed that ciliary pH did not change with ATP by using a newly developed ciliary pH biosensor, 5HT<sub>6</sub>-CFP-Venus(H148G) (**Figure 3-14**).

### 3.2.3 Ciliary calcium responses to mechanical stimulation

Finally, we asked whether we could detect Ca<sup>2+</sup> dynamics in primary cilia when subjecting them to a mechanical stimulus. Fluid flow across the apical cell membrane induces bending of the cilia, and the resultant shear force is commonly believed to activate cilia-localized Ca<sup>2+</sup>-permeable TRPP2 channels (Nauli et al., 2003). However, the critical step involving the entry of extracellular Ca<sup>2+</sup> into the ciliary lumen has not been demonstrated. Therefore, we set up a fluid flow system to subject ciliated mouse inner medullary collecting duct (mIMCD3) cells with defined laminar flow. To normalize for the anticipated flow-induced movements of cilia, we transiently expressed 5HT<sub>6</sub>-mCherry-G-GECO1.0 in cells such that cilia spatial movements could be visualized by the mCherry fluorescence marker (**Figures 3-15A-B**). Initiation of fluid flow (with wall shear stress corresponding to a physiological value of 1 dyne/cm<sup>2</sup>) induced the immediate bending of cilia (**Figure 3-15C**), whereas specific bending behavior of each primary cilium was dependent on parameters such as spatial orientation and cilium length. Flow initiation also induced a pronounced increase in ciliary Ca<sup>2+</sup> which initiated within 15 s of flow induction on average, and attained peak responses at 1 min after induction of flow (**Figures 3-15C and 3-16A**). To validate that the observed changes in GFP fluorescence in primary cilia were indicative of genuine changes in GECI activity and were not due to ciliary movement, we ascertained that flow initiation did not induce a significant change in GFP fluorescence in cilia expressing 5HT<sub>6</sub>-mCherry-GFP ( $P = 0.9545$ ), whereas cilia expressing 5HT<sub>6</sub>-mCherry-G-GECO1.0 exhibited an

average 1.46-fold increase in GFP fluorescence 1 min after induction of flow (**Figures 3-16 and 3-17**). Additional work is required to elucidate the source of  $\text{Ca}^{2+}$  signaling observed.

### **3.3 Discussion**

The intermediate affinity of G-GECO1.0 for  $\text{Ca}^{2+}$  ( $K_d$  value of 749 nM (Zhao et al., 2011)) is of sufficient sensitivity to detect changes in  $\text{Ca}^{2+}$  concentrations in primary cilia when cells are stimulated with ATP and mechanical flow. Nevertheless, other forms of signaling stimuli may induce lower concentration ranges of ciliary  $\text{Ca}^{2+}$  that may not be detectable by G-GECO1.0. For these applications, it may be necessary to target GECIs with lower  $K_d$  values to the primary cilia. The successful application of the cilia-targeted GECI also serves as a proof of concept to extend this approach to visualize other signaling molecules in primary cilia.

### **3.4 Materials and Methods**

#### **3.4.1 DNA Construction**

All DNA plasmids are available through Addgene.

*$\beta$ 1Int-HaloTag-Arl13b-C-GFP (IA-GFP) expression vector:* DNA encoding the human Arl13b C-terminal region (amino acids 355–428 of Arl13b (Hori et al., 2008)) was amplified using PCR primers (5'-cccaagcttaggaaccaccgggtagaacc and 5'-aggtegactgagatcacatcatgagcatca) and subcloned into pEGFP-C-CMV5 (a modified pCMV5 mammalian expression vector encoding C-terminal GFP-fusion protein). DNA encoding  $\beta$ 1Int-HaloTag (Svendsen et al., 2008) was then subcloned into pEGFP-C-CMV5/Arl13b(355–428) to make the  $\beta$ 1Int-HaloTag-Arl13b-C-GFP expression vector.

*Lyn-GFP expression vector:* GFP was subcloned into sequence encoding Lyn-YFP (Clontech pYFP-N1 vector; gift from M. Fivaz) using AgeI and BsrGI to replace YFP.

*5HT<sub>6</sub>-GFP-CTS20 expression vector:* DNA encoding 5HT<sub>6</sub> flanked by AgeI was amplified by PCR primers (5'-ctactgaccggtcgccaccatggttcagagcccgccctgtcaacag and 5'-gctgacaccggtcctcctgcgctaccaccagcactgttcattgggggaaccaagtgg) from sequence encoding 5HT<sub>6</sub>-GFP (Berbari et al., 2008) (Clontech pEGFP-N3 vector; gift from A. Seki and T. Meyer), and then subcloned into the 5' AgeI site of sequence encoding GFP-CTS20 (ref. 20) (Clontech pEGFP-C2 vector; gift from G. Pazour). CTS20 sequence encodes residues 1–20 of the N-terminal cytoplasmic tail of fibrocystin.

*5HT<sub>6</sub>-YC3.60 expression vector:* DNA encoding 5HT<sub>6</sub> flanked by HindIII was amplified by PCR primers (5'-catccgaagcttgccaccatggttcagagc and 5'-gcacctaaagcttctcctgcgcttctcctgcgctctttgagattcgctggaacacatgataatag) from sequence encoding 5HT<sub>6</sub>-GFP (Berbari et al., 2008) (Clontech pEGFP-N3 vector) and then subcloned into a YC3.60 vector (gift from A. Miyawaki).

*5HT<sub>6</sub>-G-GECO1.0 expression vector:* DNA encoding 5HT<sub>6</sub> flanked by BamHI was amplified by PCR primers (5'-cattcaggatccgccaccatggttcagagc and 5'-gcatctggatcctcctcctcgcgctaccacca) from sequence encoding 5HT<sub>6</sub>-GFP (Berbari et al., 2008) (Clontech pEGFP-N3 vector) and then subcloned into CMV-G-GECO1.0 vector (obtained from Addgene).

*5HT<sub>6</sub>-G-CaMP expression vector:* DNA encoding G-CaMP5G (gift from L. Looger) flanked with BamHI and HindIII was amplified by PCR primers (5'-ctactgggatccagtgtggtgtagcgcaggaggaatgggttctcatcatcatcatcatg and 5'-gcaacatagttaagaataccagtcattctttcac) and then subcloned into a 5HT<sub>6</sub>-CFP-FKBP vector (Lin et al., 2013) in replacement of CFP-FKBP.

*TNXXL-CTS20 expression vector:* First, the stop codon was removed from the 3' end of the TNXXL sequence (gift from O. Griesbeck) by site-directed mutagenesis (Stratagene) using PCR

primers (5'-cgaggactacgaattctgcagatatccatcacactggcgccc and 5'-ggccgccagtgtgatggatatctgcagaattcgtagtcctcg). The resulting vector was digested with EcoRI and ligated to CTS20 digested with EcoRI from a GFP-CTS20 vector.

*TNXXL-CTS68 expression vector:* The TNXXL vector with no stop codon was digested with EcoRI and then ligated to CTS68 digested with EcoRI from a GFP-CTS20 vector. CTS68 encodes residues 1–68 of the N-terminal cytoplasmic tail of fibrocystin.

*5HT<sub>6</sub>-mCherry-G-GECO1.0:* DNA encoding G-GECO1.0 was digested from CMV-G-GECO1.0 vector using BamHI and EcoRI and subcloned into a sequence encoding 5HT6-mCherry (pmCherry-C1, Clontech) that had been digested with BglII and EcoRI.

*5HT<sub>6</sub>-mCherry-GFP expression vector:* GFP was digested from sequence encoding 5HT6-GFP (pEGFP-N3, Clontech) using Acc65I and BsrGI and subcloned into a sequence encoding 5HT6-mCherry (pmCherry-C1, Clontech) that had been digested with Acc65I.

*5HT6-CFP-Venus(H148G) expression vector:* Sequence encoding 5HT6-CFP was first constructed by subcloning sequence encoding 5HT6 into a CFP vector using NheI and AgeI. Sequence encoding Venus(H148G) flanked with EcoRI and BamHI was then amplified by PCR primers (5'-catccggaattcgatggtgagcaagggcgagg and 5'-gcagtgggatccttactgtacagctcgccatgcc) and subcloned into the 5HT6-CFP vector.

### **3.4.2 Cell culture and transfection**

NIH-3T3 cells and mIMCD3 cells containing an integrated FRT site in the genome (gift from R. Reed) were cultured in DMEM (Gibco) supplemented with 10% FBS. For all transient transfections, cells were transfected with the respective DNA constructs by plating them directly in a transfection solution containing DNA plasmid and FuGENE HD (Roche). Cells were plated



on poly(D-lysine)-coated borosilicate glass Lab-Tek 8-well chambers (Thermo Scientific). Ciliogenesis was induced by serum starvation for 24 h. For flow experiments, transfected cells were seeded into Microslide VI0.4 channels (ibidi) at a cell suspension density of approximately  $1.3 \times 10^6$  cells/ml to achieve confluence.

### **3.4.3 Immunofluorescence**

To mark primary cilia, NIH-3T3 cells were fixed with 4% (w/v) paraformaldehyde, permeabilized with 0.1% (v/v) Triton X-100 and immunostained with mouse monoclonal anti-acetylated tubulin antibody (Sigma, T7451, 1:2,000 dilution) and secondary anti-mouse antibody conjugated to Alexa Fluor 568 (Invitrogen, 1:1,000 dilution). For immunostaining of IMCD3 cells, cells were grown on cover slips, transfected with vector encoding 5HT6-YFP, cultured for 72 h, washed with phosphate-buffered saline (PBS) and fixed with ice-cold methanol at  $-20^{\circ}\text{C}$  for 7 min. Fluorescence images were obtained using a LSM710 confocal microscope (Carl Zeiss) equipped with a Plan Apochromat  $\times 100$  oil-immersion objective lens (NA 1.4) and processed using ImageJ software. The antibodies used include rabbit polyclonal antibodies against pericentrin (Babco, PRB-432C, 1:250 dilution), NPHP3 (Proteintech, 22026-1-AP, 1:1,000 dilution), IFT88 (Proteintech, 13967-1-AP, 1:750 dilution), Arl13b (Proteintech, 17711-1-AP, 1:1,000 dilution), Cep164 (Novus, 45330002, 1:4,000 dilution), Cep290 (Bethyl Laboratories, A301-659A, 1:1,000 dilution), and mouse monoclonal antibodies against acetylated  $\alpha$ -tubulin (Sigma; 6-11B-1, T7451, 1:1000 dilution),  $\gamma$ -tubulin (Sigma; GTU-88, T-6557, 1:1000 dilution) and poly(Glu-tubulin) (Enzo; GT335, ALX-804-885-C100, 1:1,000 dilution). The secondary antibodies used in this study were Alexa Fluor 568-labeled anti-mouse IgG (Molecular Probes, 1:1,500 dilution) and Alexa Fluor 633-labeled anti-rabbit IgG (Molecular Probes, 1:2,000 dilution).

### **3.4.4 Transmission electron microscopy**

For the ultrastructural analysis of cilia overexpressing 5HT6-GFP or GFP alone, the genes encoding these proteins were introduced into NIH-3T3 cells using a lentiviral expression system developed by H. Miyoshi at the RIKEN BioResource Center (Honda et al., 2010). For the expression of 5HT6-GFP, the cDNA was amplified with KOD DNA polymerase and ligated into the Eco47III site of CSII-CMV-MCS-IRES2-Bsd. For the expression of GFP alone, the CS-CDF-CG-PRE was used. These expression constructs were packaged into infectious viral particles (Honda et al., 2010) and added to the NIH-3T3 culture medium at the multiplicity of infection of >20. After the viral transduction, cells expressing 5HT6-GFP were selected with 30  $\mu$ M blasticidin. Expression of 5HT6-GFP or GFP alone in most if not all cells was confirmed by fluorescence microscopy. Preparations of the cells and observation of cilia by transmission electron microscopy were carried out principally according to the previous study (Narita et al., 2010) with slight modifications. Briefly, cultured cells were fixed with a half Karnovsky's solution (2% paraformaldehyde and 2.5% glutaraldehyde in 0.1 M cacodylate buffer, pH 7.5) supplemented with 1% tannic acid for 30 min at room temperature, followed by rinse with 10% sucrose in cacodylate buffer (pH 7.5) three times. The cells were post-fixed with 1% osmium tetroxide for 30 min on ice, followed by extensive irrigation with ice-cold distilled water. Subsequently, the cells were stained en bloc with 1% uranyl acetate in 50% ethanol for 2 h, dehydrated with a series of graded concentration of ethanol and embedded in epoxy resin. The cells in the epoxy block were cut by the LKB2088 ultramicrotome (Stockholm), mounted onto formvar-reinforced single slot grids, and stained with uranyl acetate and lead citrate. The samples were observed under the Hitachi H-7500 transmission electron microscope (Tokyo). Images of ciliary cross-sections were analyzed with ImageJ to measure the ciliary diameter.

### **3.4.5 Epi-fluorescence imaging**

Most of the imaging experiments were performed on an Axiovert135TV epi-fluorescence microscope (Zeiss) with 63× oil objective (Zeiss), and images were collected by a QIClick charge-coupled device (CCD) camera (QImaging). For the dual-color epi-fluorescence imaging under flow conditions, IX-71 (Olympus) microscope was used together with a 40× oil objective (Olympus) and a CoolSNAP HQ CCD camera (Photometrics). Imaging was driven by Metamorph 7.5 imaging software (Molecular Devices). All calcium imaging experiments were performed in Dulbecco's Phosphate-Buffered Saline (Gibco) containing 0.9 mM [Ca<sup>2+</sup>], except for the characterization of the cytosolic dynamic range of each CTS-GECl, which was performed in DMEM with 25 mM HEPES (Gibco). All pH imaging experiments were performed in DMEM with 25 mM HEPES (Gibco). All imaging experiments were completed at room temperature (21–23 °C). FRET images were thresholded to remove background before any contrast adjustments.

#### **3.4.6 Ciliary and cytoplasmic pH determination**

NIH-3T3 cells were transfected with either vector encoding 5HT6-CFP-Venus(H148G) for cilia measurements, or vector encoding CFP plus vector encoding Venus(H148G) for cytoplasmic measurements. For measurements of fluorescence ratios at known pH, cells were washed once with DMEM plus HEPES at the chosen pH, then allowed to sit in DMEM plus HEPES at the known pH containing 5 μM each of the H<sup>+</sup> ionophores nigericin and monensin (both Sigma) for 5 min to equilibrate. Approximately 8–10 cilia were analyzed at each chosen pH point. All fluorescence ratios are normalized to an initial measurement at pH 7.4. For determination of pH in cilia and cytoplasm, cells were placed in DMEM plus HEPES at the standard pH of 7.4 with no H<sup>+</sup> ionophores and imaged.

#### **3.4.7 Flow system coupled with epi-fluorescence time-lapse imaging**

Syringe pump (Model 230, KD Scientific) was used to provide unidirectional laminar flow when connected with cell-seeded microchannel slides. DPBS (Gibco) was used as flow perfusate. Using the Poiseuille equation for rectangular channels,  $\tau = 6\mu Q/bh^2$  (where  $\tau$  is shear stress,  $\mu$  is medium viscosity,  $Q$  is the flow rate,  $b$  is channel width and  $h$  is channel height), a flow rate of 0.6 ml/min was provided by the syringe pump to provide a shear stress of approximately 1 dyne/cm<sup>2</sup> within the microchannel. In these experiments, only upright-positioned cilia were imaged. Each cilium was imaged at 0.067 Hz for 2 min before flow was initiated for a period of ~7.5 min. Imaging was continued for an additional 4 min after flow was stopped. At each time point, each primary cilium was imaged in the x-y plane with nine z-stacks (separated by 1  $\mu$ m). A total of 18 cells from seven independent experiments were imaged and quantified for 5HT6-mCherry-G-GECO1.0, and a total of nine cells from three independent experiments were imaged and quantified for 5HT6-mCherry-GFP. Notably, the flow-induced calcium response was found to be sensitive to environmental changes. Each imaging experiment was performed at room temperature (21–23 °C), and was completed within 1 h after cells were taken out from an incubator 37 °C. Fluorescence images shown in Figure 3-15C are z-projections of nine consecutive x-y planes. GFP and corresponding mCherry cilia images have been normalized against background signal variation. GFP divided by mCherry fluorescence ratio cilia images were obtained by taking the fluorescence ratio of background-normalized GFP and background-normalized mCherry signal intensities and represented in pseudocolor scale. These values have been further subjected to two other steps of normalization, (i) normalization against signal area variation and (ii) normalization against basal signal intensities (before flow), and presented in graph plots in Figure 3-16A as normalized measurements of GFP divided by mCherry fluorescence ratios in response to flow stimulation.

### 3.4.8 Accession codes

GenBank, European Molecular Biology Laboratory and DNA Data Bank of Japan: NM\_021358 (5HT6), NM\_153179.2 (fibrocystin), NM\_001174150 (Arl13b) and NM\_002211 ( $\beta$ 1 integrin receptor).

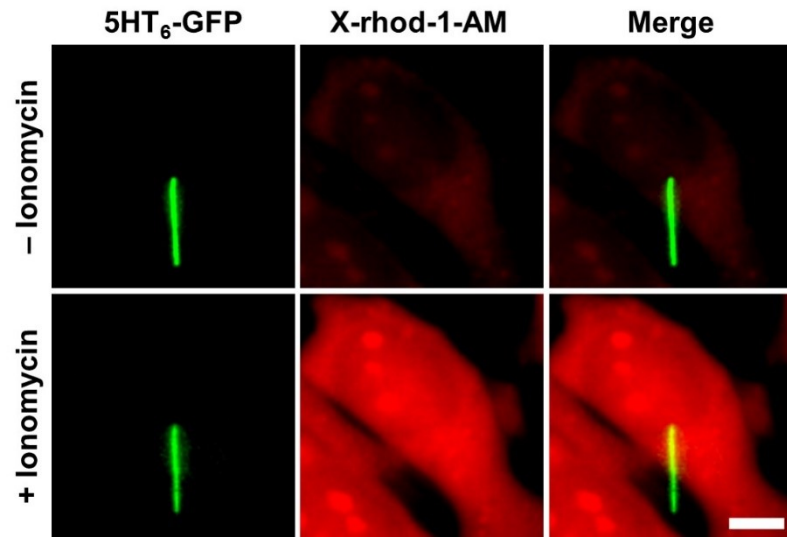


**Figure 3-1. The inability of small molecule dyes to detect increases in ciliary  $\text{Ca}^{2+}$ .**

X-rhod-1 AM fails to detect increase in ciliary  $\text{Ca}^{2+}$  in mIMCD3 cells after the addition of 1  $\mu\text{M}$  Ionomycin due to its inability to specifically target the primary cilia.

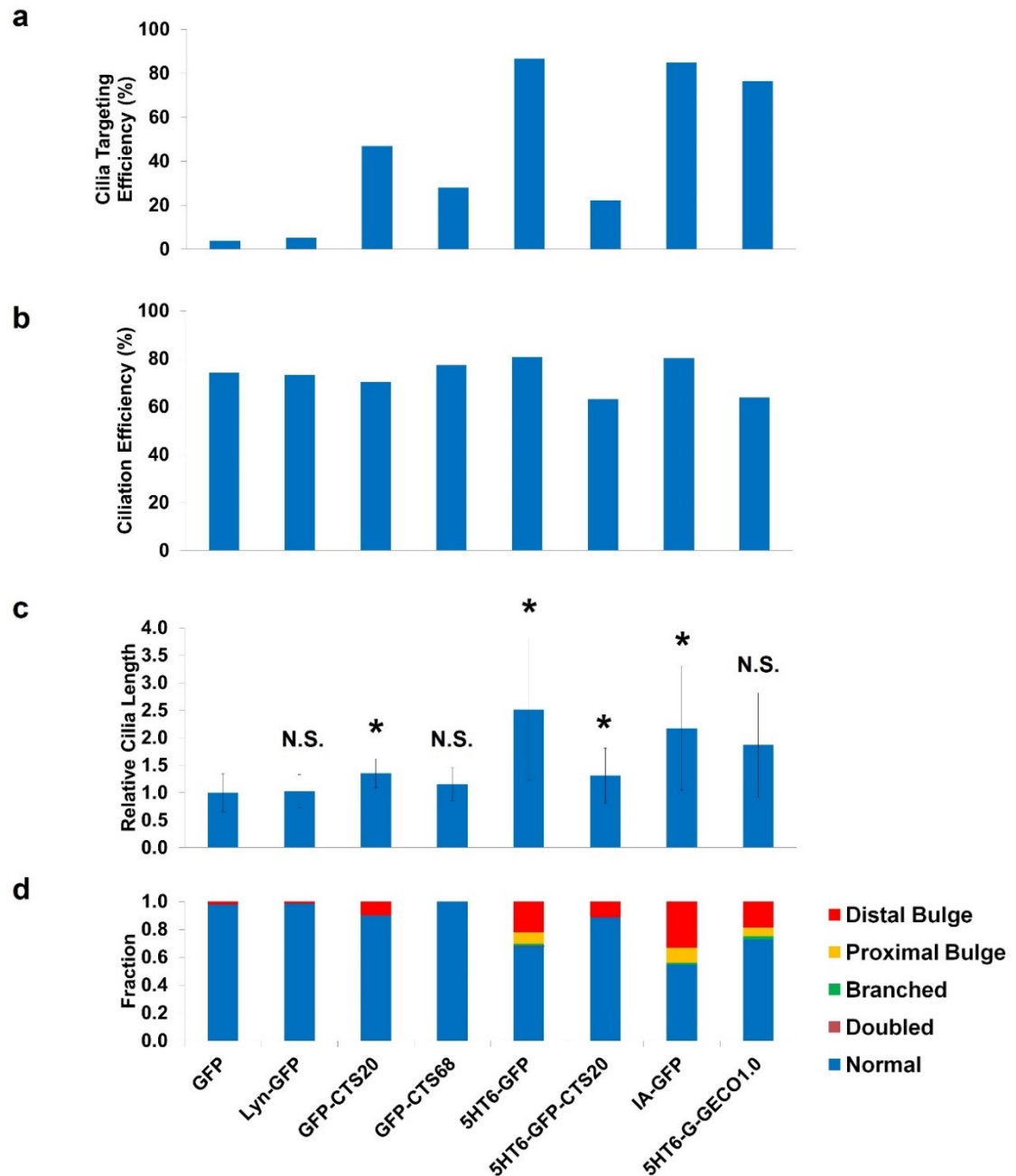


**Figure 3-2. Targeting efficiency of different CTSs and their effects on ciliation efficiency, cilia length, and cilia morphology in NIH-3T3 cells.**

Columns for (A-C) correspond to the columns in (D) and represent the same construct. (A) Targeting efficiency for each construct. Data represent the number of cells in which the GFP is targeted in the cilia divided by the number of cells with cilia in which GFP is expressed

anywhere. For every cilium, the ratio of the average ciliary GFP fluorescence to average cytosolic GFP fluorescence was computed. Any cilium with ratio value greater than 2 was considered to have the specified construct targeted in the cilia. ( $n=101$ ,  $n=19$ ,  $n=68$ ,  $n=57$ ,  $n=150$ ,  $n=27$ ,  $n=172$ , and  $n=102$ , respectively for GFP, Lyn-GFP, GFP-CTS20, GFP-CTS68, 5HT<sub>6</sub>-GFP, 5HT<sub>6</sub>-GFP-CTS20, IA-GFP, and 5HT<sub>6</sub>-G-GECO1.0.) (B) Ciliation efficiency for each construct. Data represent the number of GFP-expressing cells which possess a cilium (as determined by staining for acetylated tubulin) divided by the total number of GFP-expressing cells. ( $n=259$ ,  $n=278$ ,  $n=185$ ,  $n=119$ ,  $n=567$ ,  $n=179$ , and  $n=401$ , respectively for GFP, Lyn-GFP, GFP-CTS20, GFP-CTS68, 5HT<sub>6</sub>-GFP, 5HT<sub>6</sub>-GFP-CTS20, IA-GFP, and 5HT<sub>6</sub>-G-GECO1.0.) (C) Average cilia length for each construct normalized to average cilia length in GFP expressing cells. Constructs with statistically significant differences as compared to GFP are indicated with an asterisk. N.S. indicates no statistically significant difference as compared to GFP. Error bars are standard deviation. (Student's *t*-test,  $P=0.49$ ,  $P=0.0018$ ,  $P=0.18$ ,  $P=1.5E-73$ ,  $P=0.0012$ ,  $P=2.8E-34$ , and  $P=0.055$  respectively for Lyn-GFP, GFP-CTS20, GFP-CTS68, 5HT<sub>6</sub>-GFP, 5HT<sub>6</sub>-GFP-CTS20, IA-GFP, and 5HT<sub>6</sub>-G-GECO1.0;  $n=147$ ,  $n=133$ ,  $n=10$ ,  $n=400$ ,  $n=35$ ,  $n=288$ , and  $n=81$ , respectively for GFP, Lyn-GFP, GFP-CTS20, GFP-CTS68, 5HT<sub>6</sub>-GFP, 5HT<sub>6</sub>-GFP-CTS20, IA-GFP, and 5HT<sub>6</sub>-G-GECO1.0.) (D) Cilia morphology associated with each construct. Cilia were classified in five categories: normal morphology, doubled, branched, proximal bulge, and distal bulge. For GFP and Lyn-GFP constructs, all cilia in GFP-expressing cells were analyzed. For the remaining cilia-targeting constructs, only cilia that showed GFP expression were analyzed. ( $n=147$ ,  $n=131$ ,  $n=10$ ,  $n=9$ ,  $n=401$ ,  $n=35$ ,  $n=284$ , and  $n=81$ , respectively for GFP, Lyn-GFP, GFP-CTS20, GFP-CTS68, 5HT<sub>6</sub>-GFP, 5HT<sub>6</sub>-GFP-CTS20, IA-GFP, and 5HT<sub>6</sub>-G-GECO1.0.)



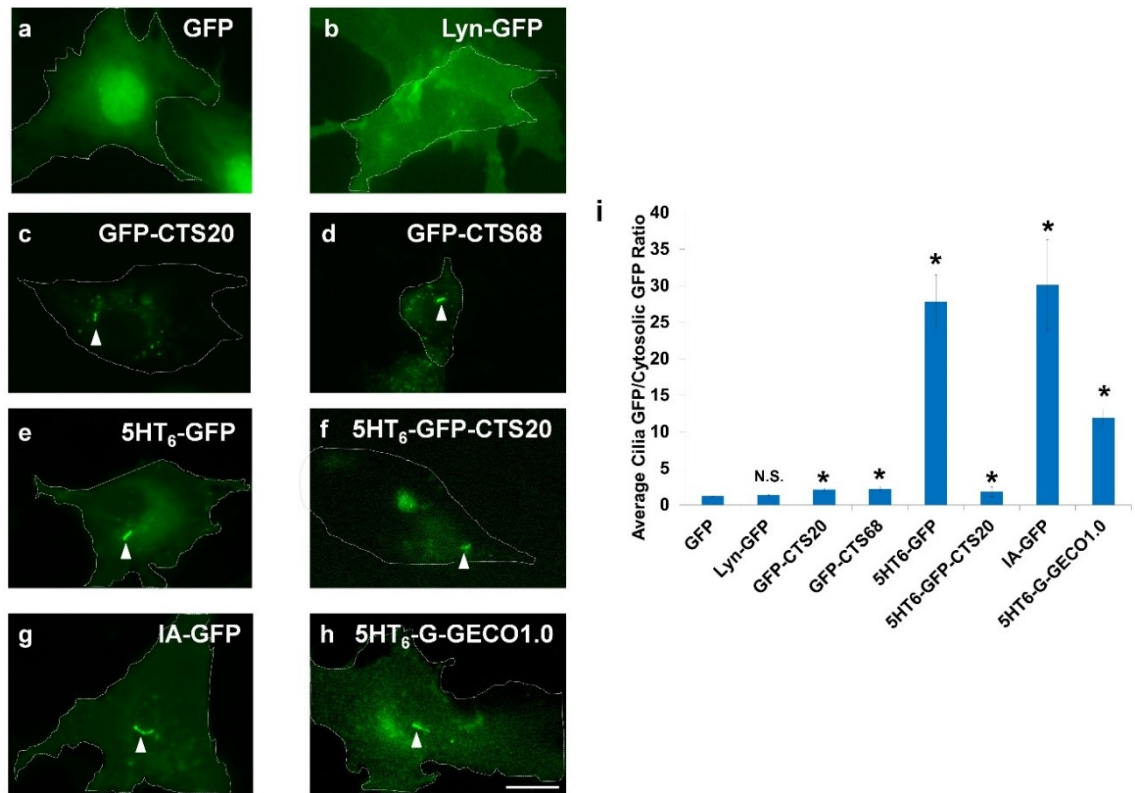


**Figure 3-3. Representative images of NIH-3T3 cells transfected with the various GFP CTS tagged constructs.**

(A) GFP. (B) Lyn-GFP. (C) GFP-CTS20. (D) GFP-CTS68. (E) 5HT<sub>6</sub>-GFP. (F) 5HT<sub>6</sub>-GFP-CTS20. (G) IA-GFP. (H) 5HT<sub>6</sub>-G-GECO. Dotted line indicates cell boundary. Scale bar indicates 10  $\mu$ m. (i) The average ciliary GFP intensity to cytosolic GFP intensity ratio values for each of the constructs. Constructs with statistically significant differences as compared to GFP are indicated with an asterisk. N.S. indicates no statistically significant difference as compared to GFP. Error bars are SEM. (Student's *t*-test,  $P=0.16$ ,  $P=4.2E-6$ ,  $P=0.011$ ,  $P=1.2E-11$ ,  $P=0.36$ ,  $P=5.3E-6$ , and  $P=3.1E-4$  respectively for Lyn-GFP, GFP-CTS20, GFP-CTS68, 5HT<sub>6</sub>-GFP, 5HT<sub>6</sub>-GFP-CTS20, IA-GFP, and 5HT<sub>6</sub>-G-GECO1.0;  $n=101$ ,  $n=19$ ,  $n=68$ ,  $n=57$ ,  $n=150$ ,  $n=27$ ,  $n=172$ , and  $n=102$ , respectively for GFP, Lyn-GFP, GFP-CTS20, GFP-CTS68, 5HT<sub>6</sub>-GFP, 5HT<sub>6</sub>-GFP-CTS20, IA-GFP, and 5HT<sub>6</sub>-G-GECO1.0.)

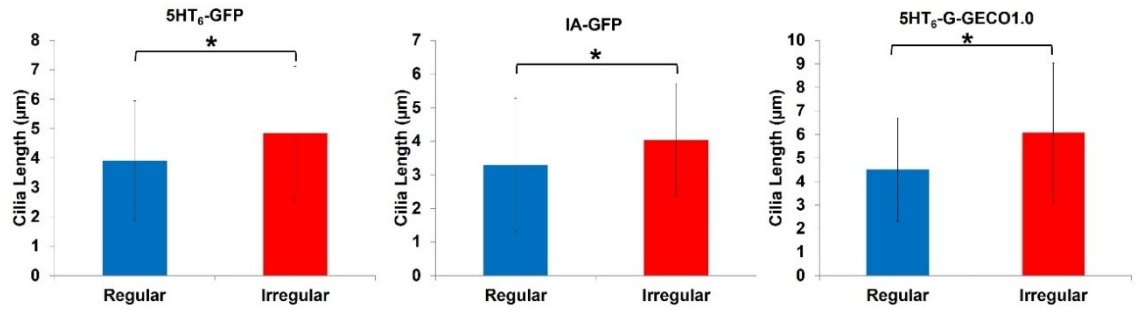


**Figure 3-4. Cilia length versus morphology for 5HT<sub>6</sub>-GFP, IA-GFP, and 5HT<sub>6</sub>-G-GECO1.0 constructs.**

For this analysis, cilia displaying the doubled, branched, proximal bulge, or distal bulge morphologies were categorized as irregular. Statistically significant differences, as determined by a two sample student's *t*-test, are indicated with an asterisk. Error bars are standard deviation. (For 5HT<sub>6</sub>-GFP,  $n=270$  and  $n=129$ , for regular and irregular, respectively, with  $P=4.1E-5$ . For IA-GFP,  $n=156$  and  $n=127$ , for regular and irregular, respectively, with  $P=0.0008$ . For 5HT<sub>6</sub>-G-GECO1.0,  $n=81$  and  $n=22$ , for regular and irregular, respectively, with  $P=0.012$ )

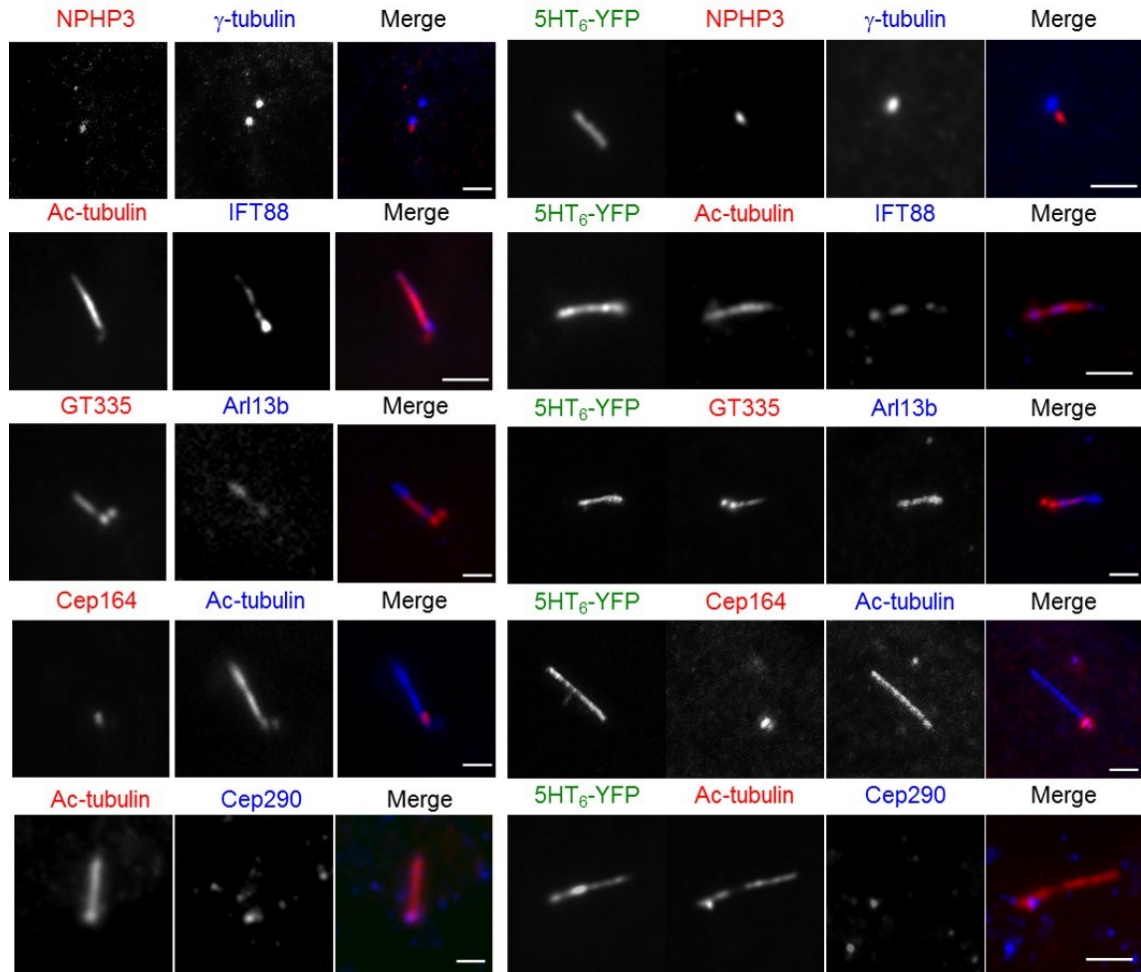


**Figure 3-5. Representative images of mIMCD3 cilia expressing 5HT<sub>6</sub>-YFP immunostained to reveal the location of various ciliary proteins.**

mIMCD3 cells expressing 5HT<sub>6</sub>-YFP were immunostained against various ciliary proteins. Compared with control cells, no difference in protein localization was observed. Abbreviations: Nephrocystin-3 (NPHP3), Gamma-tubulin ( $\gamma$ -tubulin), Acetylated  $\alpha$ -tubulin (Ac-tubulin), Intraflagellar Transport Protein 88 (IFT88), Poly-Glutamylated-tubulin (GT335), ADP-ribosylation factor-like protein 13B (Arl13b), Centrosomal Protein of 164 kDa (Cep164), and Centrosomal Protein of 290 kDa (Cep290). Scale bars, 2  $\mu$ m.

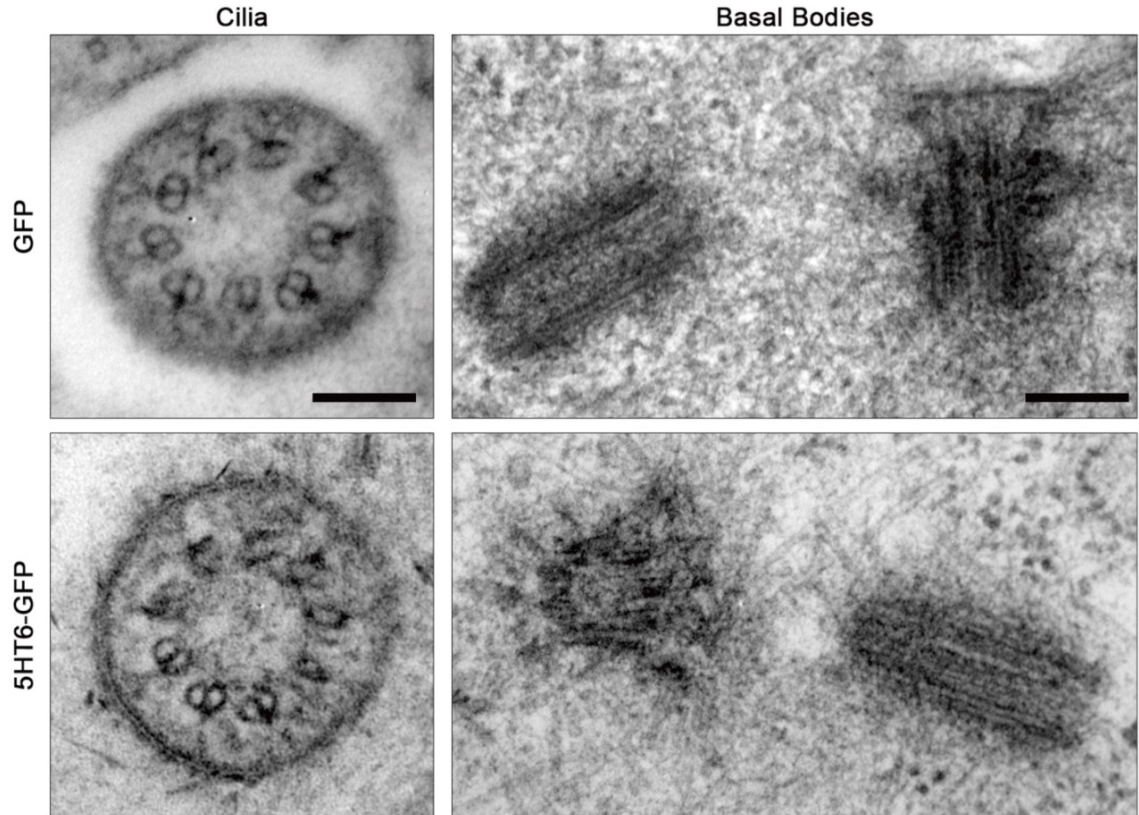


**Figure 3-6. Representative TEM images of primary cilia and basal bodies in NIH-3T3 cells expressing GFP and 5HT<sub>6</sub>-GFP.**

The ultrastructure of primary cilia and basal bodies in NIH-3T3 cells expressing 5HT<sub>6</sub>-GFP did not show any obvious changes when compared with that of control cells expressing GFP. Both of them displayed a typical 9 + 0 axonemal configuration, and their diameters were  $266 \pm 10$  (mean  $\pm$  SD,  $n=10$ ) versus  $276 \pm 15$  (mean  $\pm$  SD,  $n=10$ ) for GFP expressing and 5HT<sub>6</sub>-GFP expressing cells, respectively (Student's *t*-test,  $P=0.083$ ). Scale bars, 100 nm (cilia); 200 nm (basal bodies).

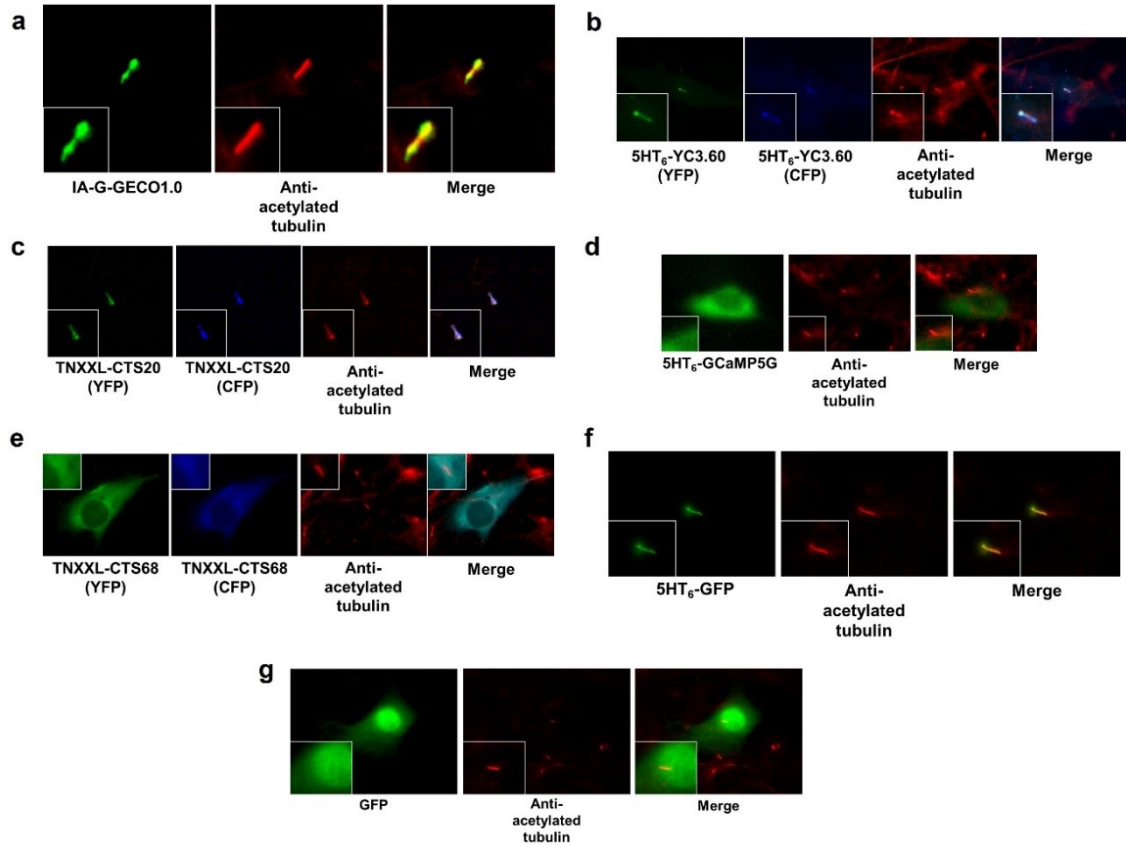


**Figure 3-7. The targeting ability of various CTS-tagged GEI.**

Only certain CTS-tagged GEI demonstrate primary cilia targeting ability. (A) IA-G-GECO1.0, (B) 5HT<sub>6</sub>-YC3.60 and (C) TNXXL-CTS20, in addition to 5HT<sub>6</sub>-G-GECO1.0 (shown in Fig. 1), were able to successfully target primary cilia in NIH-3T3 cells as determined by the constructs co-localization with Anti-acetylated tubulin, a primary cilium marker. (D) 5HT<sub>6</sub>-G-CaMP5G and (E) TNXXL-CTS68 failed to target primary cilia in NIH-3T3 cells. 5HT<sub>6</sub>-GFP and GFP were used as controls, and as expected 5HT<sub>6</sub>-GFP successfully targeted primary cilia while GFP failed to target primary cilia, as shown in (F) and (G), respectively. See Table 3-1 for targeting percentages. Note the bulging morphology in the cilia shown in (A). This morphology was common among cilia targeted with IA-G-GECO1.0.



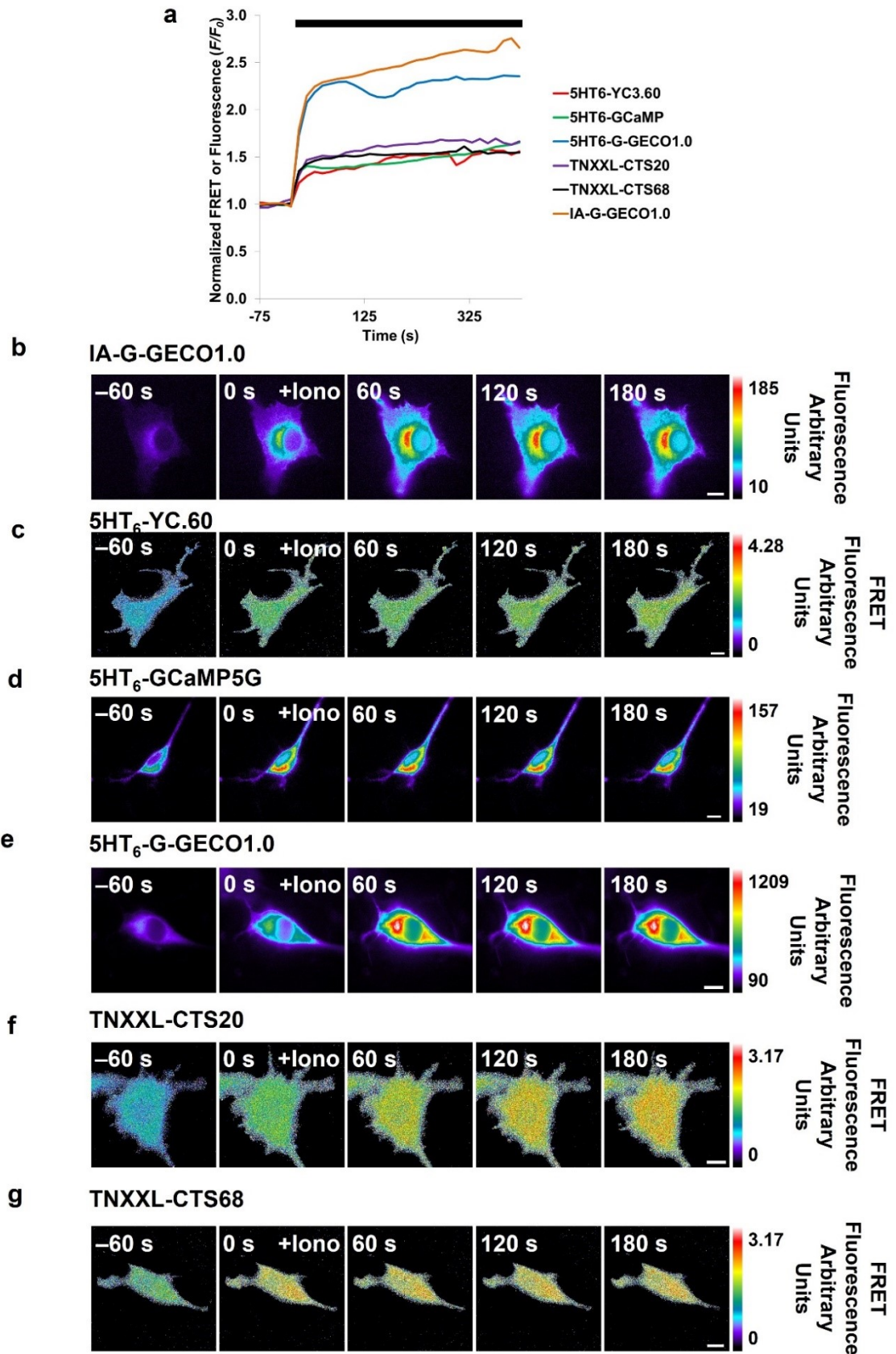


**Figure 3-8. The functionality of various CTS-tagged GECI in the cytosol of NIH-3T3 cells.**

All of the CTS-tagged GECI maintained their ability to detect a cytosolic  $\text{Ca}^{2+}$  increase induced by 1  $\mu\text{M}$  Ionomycin in NIH-3T3 cells. **(A)** The response of the various CTS-tagged GECI to 1  $\mu\text{M}$  Ionomycin (indicated by black bar). **(B-G)** are time lapse images showing the increase in cytosolic  $\text{Ca}^{2+}$  detected by IA-G-GECO1.0, 5HT<sub>6</sub>-YC3.60, 5HT<sub>6</sub>-G-CaMP5G, 5HT<sub>6</sub>-G-GECO1.0, TNXXL-CTS20, and TNXXL-CTS68, respectively, in an individual cell. Scale bar indicates 10  $\mu\text{m}$ . See 3-1 for detailed percentages.

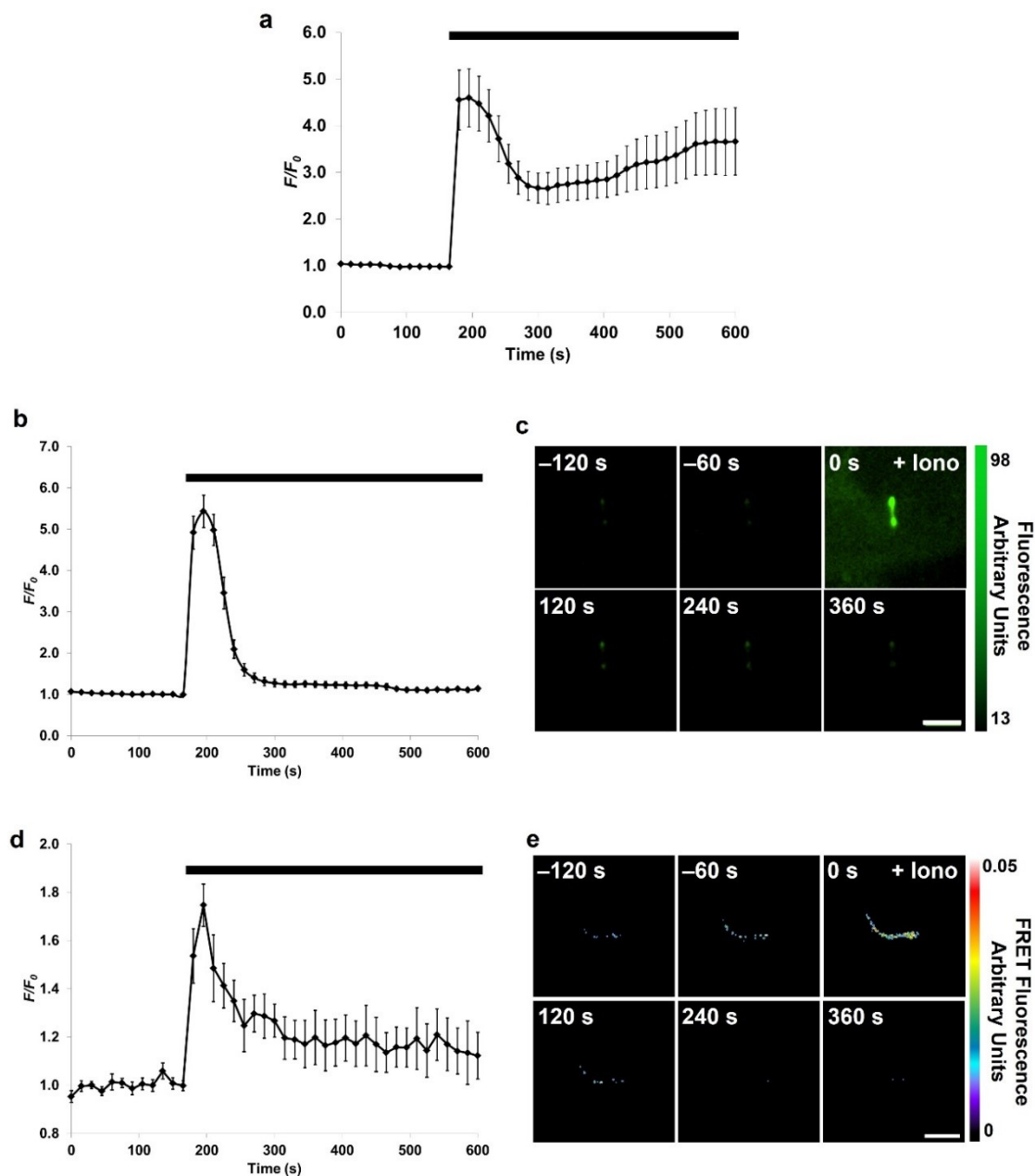


**Figure 3-9. The functionality of 5HT<sub>6</sub>-G-GECO1.0, IA-G-GECO1.0, and 5HT<sub>6</sub>-YC3.60 in cilia of NIH-3T3 cells.**

(A) The average normalized GFP fluorescence ( $F/F_0$ ) 5HT<sub>6</sub>-G-GECO1.0 in response to 2  $\mu$ M Ionomycin (indicated by black bar). Error bars are SEM. ( $n=13$ ) (B) The average normalized GFP fluorescence ( $F/F_0$ ) of IA-G-GECO1.0 in response to 2  $\mu$ M Ionomycin (indicated by black bar).



Error bars are SEM. ( $n=9$ ) (C) Timelapse imaging showing the increase in GFP fluorescence in a single cilium expressing IA-G-GECO1.0 following treatment with 2  $\mu$ M Ionomycin. Scale bar is 5  $\mu$ m. (D) The average normalized FRET fluorescence ( $F/F_0$ ) of 5HT<sub>6</sub>-YC3.60 in response to 2  $\mu$ M Ionomycin (indicated by black bar). Error bars are SEM. ( $n=10$ ) (E) Timelapse imaging showing the increase in FRET in a single cilium expressing 5HT<sub>6</sub>-YC3.60 following treatment with 2  $\mu$ M Ionomycin. Scale bar is 5  $\mu$ m. GFP fluorescence values were normalized to average baseline values measured prior to Ionomycin addition.

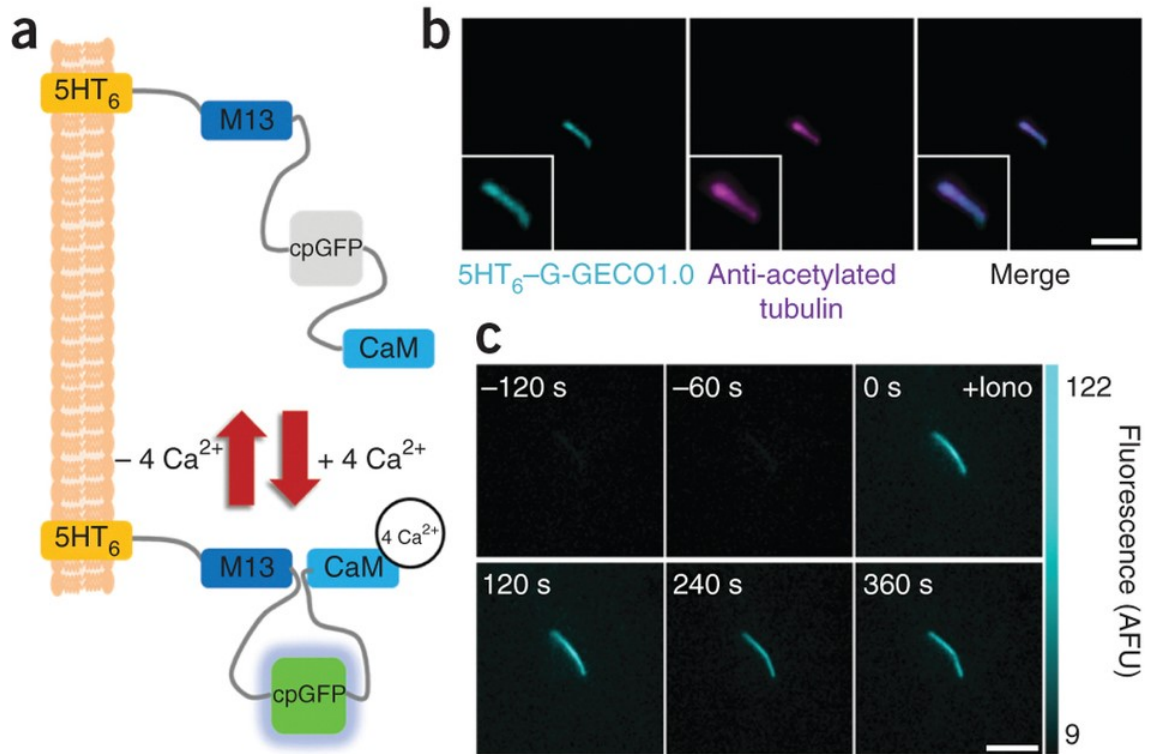


**Figure 3-10: 5HT<sub>6</sub>-G-GECO1.0 targets primary cilia and detects changes in ciliary Ca<sup>2+</sup>.**

(A) Schematic of 5HT<sub>6</sub>-G-GECO1.0, containing M13 (a skeletal muscle light-chain kinase), a circularly permuted GFP (cpGFP) and calmodulin (CaM). (B) A primary cilium from a NIH-3T3 cell expressing 5HT<sub>6</sub>-G-GECO1.0 stained with antibody against acetylated  $\alpha$ -tubulin. Scale bar, 3  $\mu$ m. Insets show magnified cilia. (C) Time-lapse imaging of a NIH-3T3 primary cilium expressing 5HT<sub>6</sub>-G-GECO1.0 at indicated times relative to addition of ionomycin (+Iono). AFU, arbitrary fluorescence unit. Scale bar, 5  $\mu$ m.

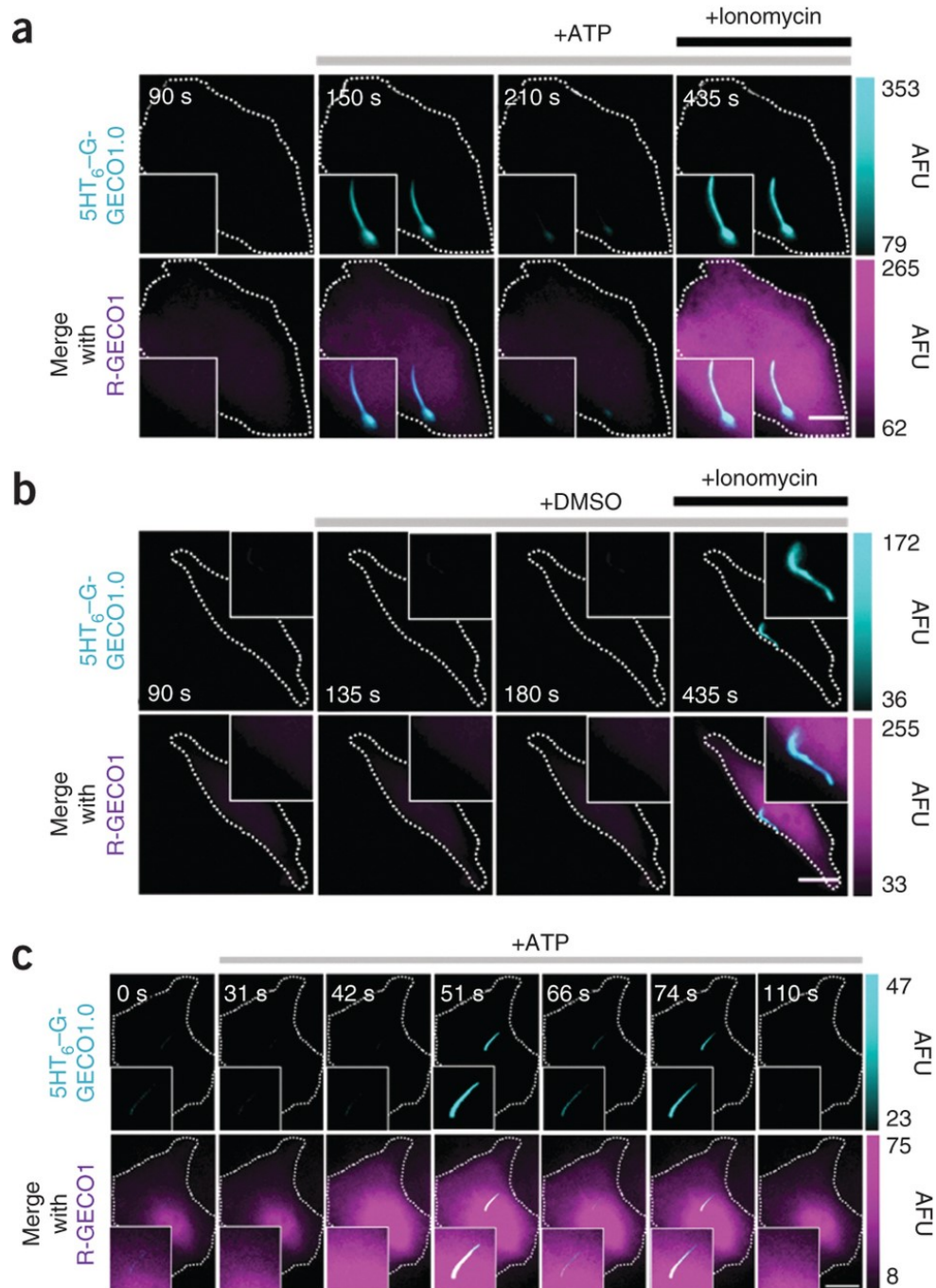


**Figure 3-11: 5HT<sub>6</sub>-G-GECO1.0 detects ciliary Ca<sup>2+</sup> influxes in response to ATP.**

(A,B) Fluorescence microscopy images of NIH-3T3 cells expressing the indicated sensors, showing response to ATP (A) or DMSO (B). Scale bars, 5  $\mu$ m. Time-lapse imaging was initiated at 0 s, and images were captured at 0.067 Hz. (C) High-speed time lapse imaging (0.63 Hz)

reveals oscillations in cytosolic and ciliary  $\text{Ca}^{2+}$  in response to 10  $\mu\text{M}$  ATP in NIH-3T3 cells expressing indicated sensors. Scale bar, 10  $\mu\text{m}$ . AFU, arbitrary fluorescence unit. Dotted lines indicate cell boundaries.

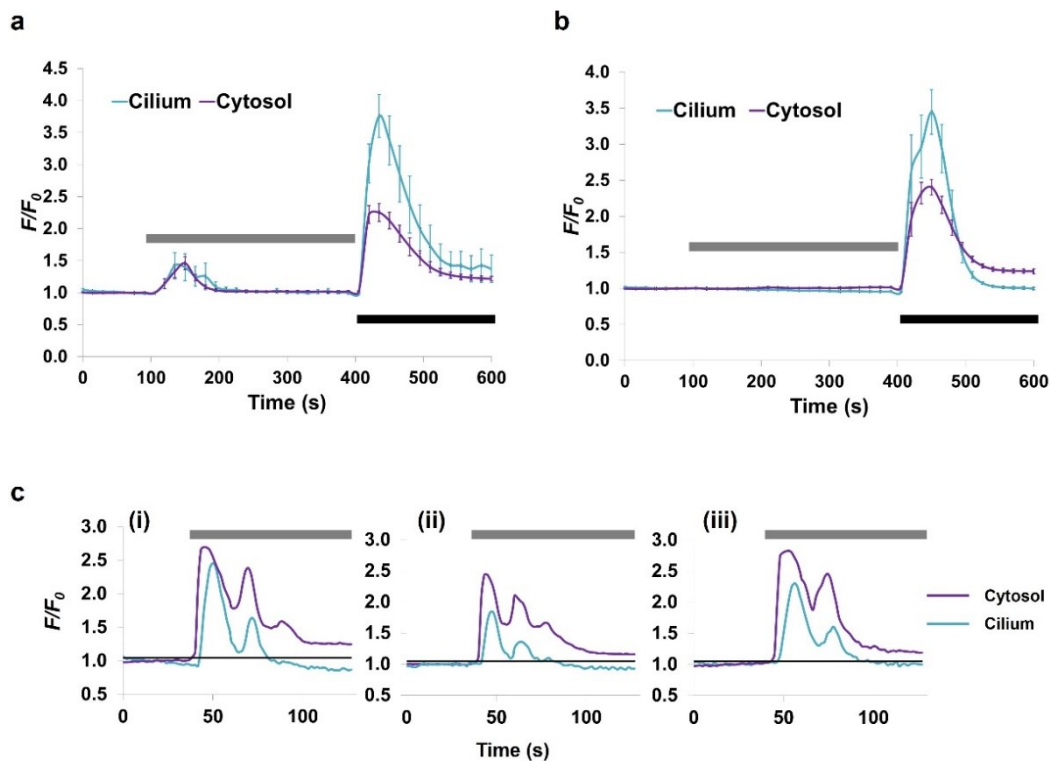


**Figure 3-12. 5HT<sub>6</sub>-G-GECO1.0 can detect ciliary Ca<sup>2+</sup> fluxes due to ATP.**

NIH-3T3 cells expressing 5HT<sub>6</sub>-G-GECO1.0 in cilia and R-GECO1 in cytosol were treated with various chemical agonists. **(A)** An increase in both ciliary and cytosolic Ca<sup>2+</sup> can be observed following the addition of 10  $\mu$ M ATP (indicated by grey bar) and then 1  $\mu$ M Ionomycin (indicated by black bar). Error bars are SEM. ( $n=11$ , 3 independent trials) **(B)** The addition of DMSO (0.1% v/v, indicated by grey bar) does not cause a detectable increase in ciliary or cytosolic Ca<sup>2+</sup>. However, subsequent addition of 1  $\mu$ M Ionomycin (indicated by black bar) does produce the expected increases in both cytosolic and ciliary Ca<sup>2+</sup>. Error bars are SEM. ( $n=15$ , 3 independent trials). Data for **(A,B)** captured at 0.067 Hz. **(C)** High speed imaging reveals oscillations in cytosolic and ciliary Ca<sup>2+</sup> levels in response to 10  $\mu$ M ATP (indicated by grey bar). Increases in cytosolic Ca<sup>2+</sup> can be seen to precede increases in ciliary Ca<sup>2+</sup>. The black lines represent the normalized fluorescence equaling 1.05. The average delay time between cytosolic and ciliary Ca<sup>2+</sup> increases was computed as the average difference in time between the cytosolic

and ciliary  $\text{Ca}^{2+}$  exceeding 1.05. Plot (i) corresponds to the images in Figure 3-11c. Data was captured at 0.63 Hz.

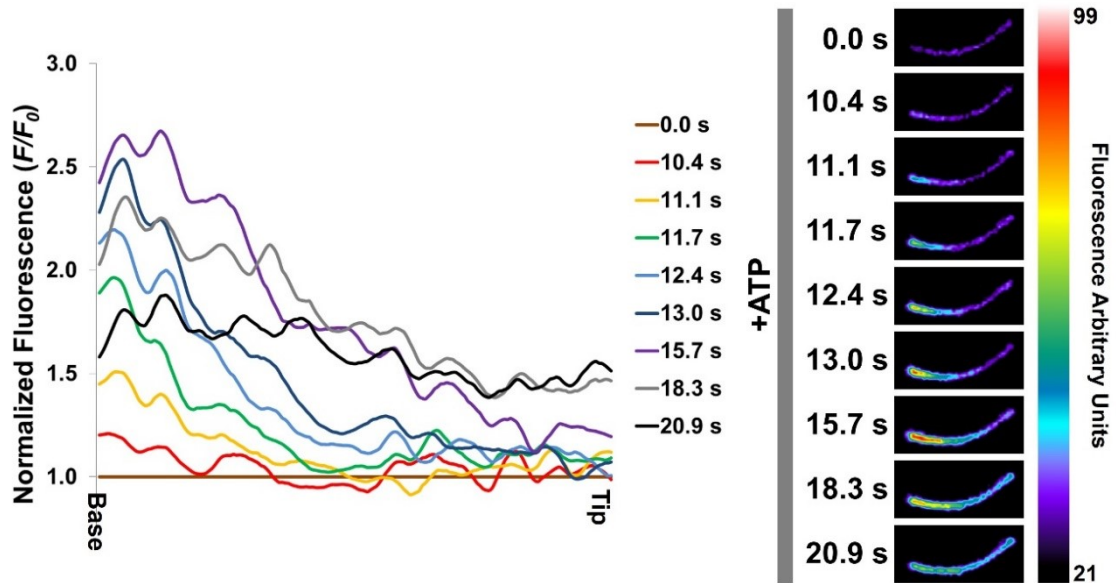


**Figure 3-13.  $\text{Ca}^{2+}$  enters from the base of cilia following ATP stimulation.**

Line scans of a representative NIH-3T3 cilium show a base to tip increase in ciliary  $\text{Ca}^{2+}$  over time as detected by 5HT<sub>6</sub>-G-GECO1.0 in response to the addition of 10  $\mu\text{M}$  ATP. GFP fluorescence was normalized to baseline values as measured at  $t=0$  s. Corresponding images for the representative cilium are shown on the right. (Time lapse images and data in plot were captured at 1.5 Hz)

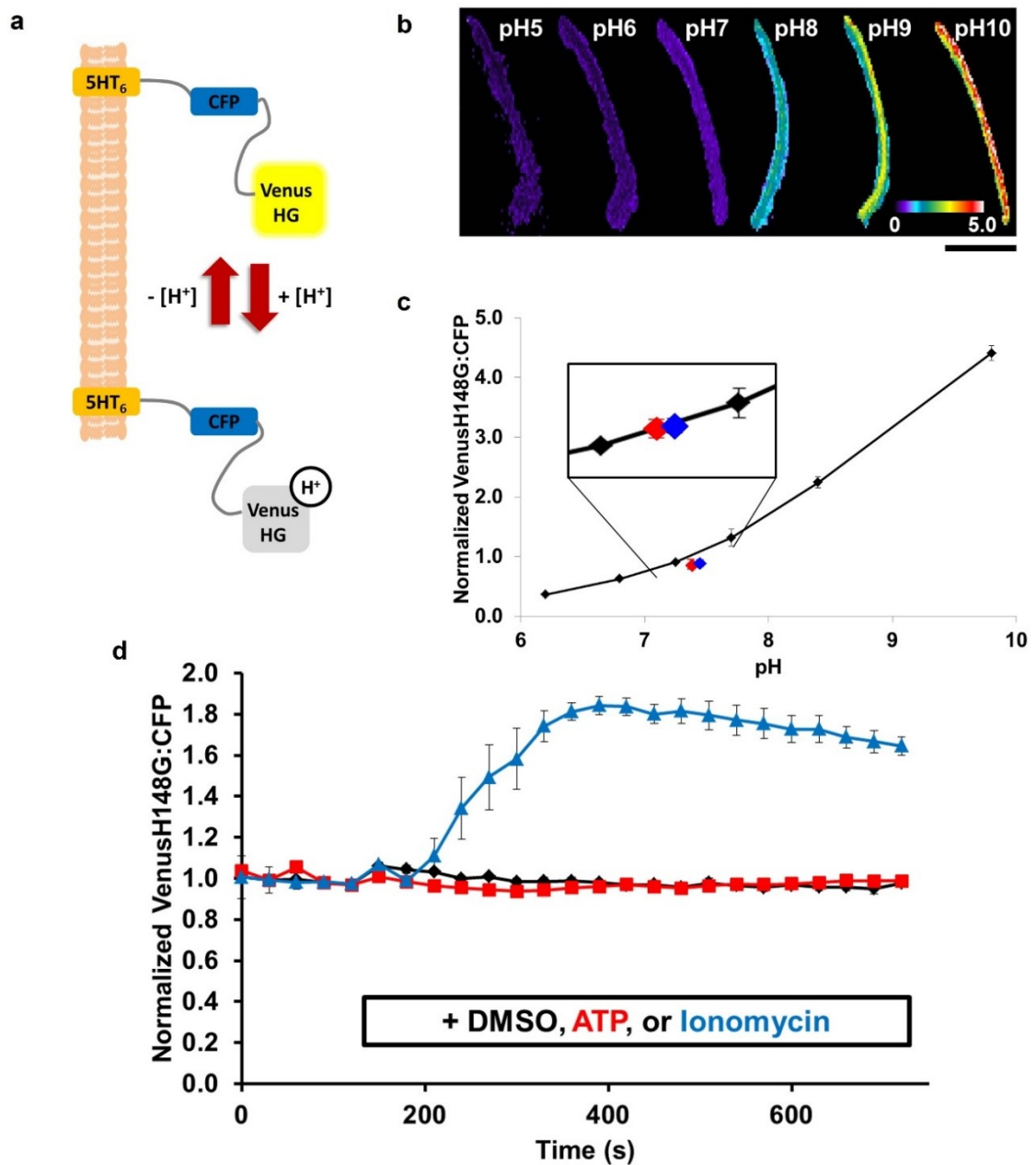


**Figure 3-14. 5HT<sub>6</sub>-CFP-Venus(H148G) detects no change in ciliary pH in response to ATP.**

(A) Schematic of 5HT<sub>6</sub>-CFP-Venus(H148G), showing the increase/decrease in YFP/Venus fluorescence in response to an increase/decrease in [H<sup>+</sup>]. (B) A single cilium of a NIH-3T3 cell transfected with 5HT<sub>6</sub>-CFP-VenusH148G was imaged at different pHs. False color is used to indicate the ratio of Venus fluorescence to CFP fluorescence. Scale bar is 5 μm. (C) A



calibration curve of the VenusH148G:CFP fluorescence ratio (normalized to pH 7.4=ratio of 1.0) was established in cilia using buffers of indicated pH (black diamonds). Fluorescence ratios were then measured in native cilia (red) and in cytoplasm (blue). Points on curve represent mean  $\pm$  SD, approximately 8-10 cilia per point. **(D)** Ciliated NIH-3T3 cells expressing 5HT<sub>6</sub>-CFP-VenusH148G were placed in DMEM plus HEPES at pH 7.4 with no H<sup>+</sup> ionophores. After equilibration, either DMSO (0.1% v/v), ATP (10  $\mu$ M), or Ionomycin (1  $\mu$ M) was added and cells were observed an additional 10 minutes. Addition of DMSO control (black) or ATP (red) has no effect on ciliary pH, while stimulation with Ionomycin (blue) causes a large increase in ciliary pH as seen by the change in Venus over CFP fluorescence ratio. Each graph shows the mean  $\pm$  SD for 8-10 cells per experimental condition.

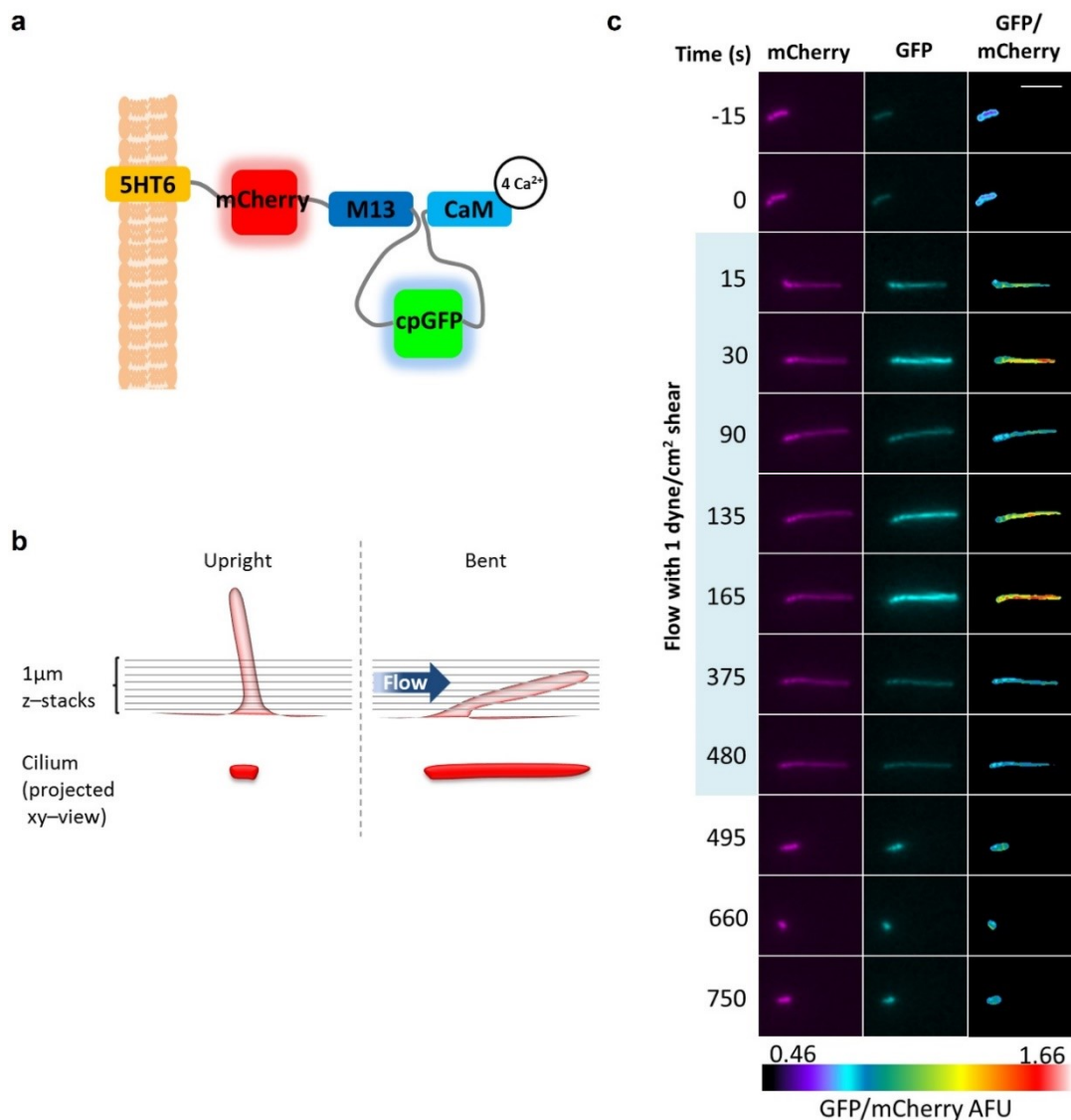


**Figure 3-15. 5HT<sub>6</sub>-mCherry-G-GECO1.0 detects ciliary Ca<sup>2+</sup> fluxes in response to laminar flow.**

(A) Schematic of 5HT<sub>6</sub>-mCherry-G-GECO1.0. In this case only the calcium bound conformation is represented. (B) An upright positioned primary cilium becomes bent in response to laminar fluid flow. Each primary cilium was imaged in the xy-plane with nine z-stacks (separated by 1 μm). Fluorescence images in (C) are z-projections of the nine consecutive xy-planes. (C) Time lapse imaging of a primary cilium subjected with laminar flow. 5HT<sub>6</sub>-mCherry-G-GECO1.0 was

expressed in mIMCD3 cells. The mCherry marker (left column) illustrates spatial movement of the cilium. GFP fluorescence intensity changes (middle column) correspond with changes in calcium signals within the cilium. GFP/mCherry images (right column) are presented in pseudocolor (scale indicator below). Time points highlighted in blue indicate the presence of laminar flow. Bar represents 5  $\mu\text{m}$ . AFU stands for arbitrary fluorescence unit.

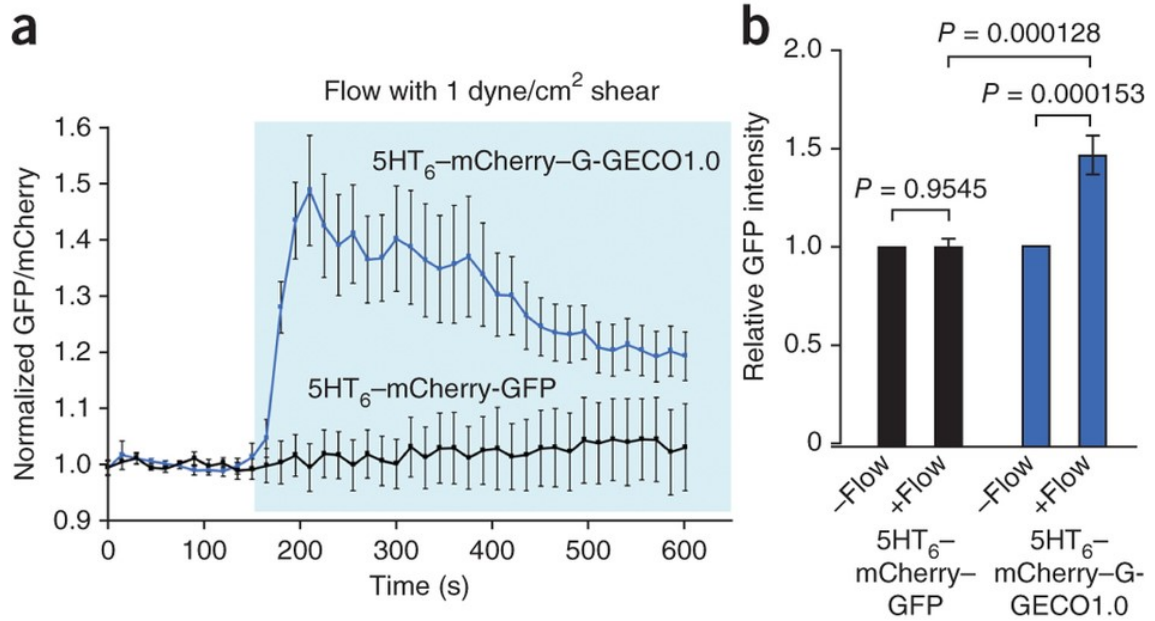


**Figure 3-16. Laminar fluid flow induces dynamic calcium signals in primary cilia.**

(A) Fluorescence intensity of GFP divided by that of mCherry before and after (light blue box) administration of flow. 5HT<sub>6</sub>-mCherry-G-GECO1.0 activity was measured for 18 primary cilia from 7 independent experiments and 5HT<sub>6</sub>-mCherry-GFP (control) activity was measured in 9 primary cilia from 3 independent experiments. Fluorescence signals were normalized against baseline fluorescence before induction of flow. Error bars, s.e.m. ( $n = 18$  for 5HT<sub>6</sub>-mCherry-G-GECO1.0 and  $n = 9$  for 5HT<sub>6</sub>-mCherry-GFP). (B) Comparison of relative GFP intensities between 5HT<sub>6</sub>-mCherry-G-GECO1.0 and 5HT<sub>6</sub>-mCherry-GFP before and after 1 min of flow induction. Error bars, s.e.m. ( $n = 18$  for 5HT<sub>6</sub>-mCherry-G-GECO1.0 and  $n = 9$  for 5HT<sub>6</sub>-mCherry-GFP).

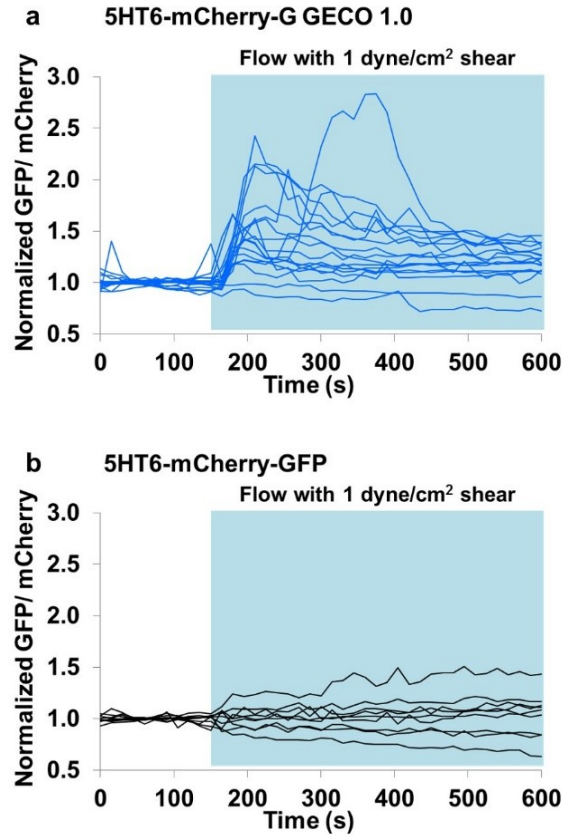


**Figure 3-17. Quantification of 5HT<sub>6</sub>-mCherry-G-GECO 1.0 activity in primary cilia under flow.**

(A) Quantification of changes in 5HT<sub>6</sub>-mCherry-G-GECO1.0 activity with time. Each line represents the normalized 5HT<sub>6</sub>-mCherry-G-GECO1.0 activity quantified from a primary cilium with time, and a total of eighteen cilia from seven independent experiments are represented. (B) Quantification of changes in GFP fluorescence intensity of 5HT<sub>6</sub>-mCherry-GFP with time. Each line represents the normalized GFP signal quantified from a primary cilium with time, and a total of nine cilia from three independent experiments are represented. In both cases, the region highlighted in light blue indicates time points with flow, and flow rate corresponding to approximately 1 dyne/cm<sup>2</sup> wall shear stress was provided during this period. Fluorescence signals have been normalized against baseline fluorescence before flow induction. Corresponding averaged responses are shown in Figure 3-16D.

<b>Genetically Encoded Calcium Indicator</b>	<b>Targeting Efficiency</b>	<b>Cytosolic Signal Dynamic Range (Maximum Percent Change in Fluorescence or FRET [SEM])</b>	<b>Ciliary Signal Dynamic Range (Maximum Percent Change in Fluorescence or FRET [SEM])</b>
5HT <sub>6</sub> -YC3.60	80%	58.2% [11.9%]	74.6% [8.8%]
5HT <sub>6</sub> -GCaMP5G	0%	65.1% [7.9%]	-
5HT <sub>6</sub> -G-GECO1.0	75%	136.1% [42.4%]	360.0% [62.1%]
5HT <sub>6</sub> -GFP	90%	-	-
IA-GECO1.0	65%	175.6% [42.3%]	443.1% [39.5%]
GFP	0%	-	-
TNXXL-CTS20	5%	69.5% [18.4%]	-
TNXXL-CTS68	0%	61.2% [8.2%]	-

**Table 3-1. Complete list of all CTS-tagged GECI and characterization of their targeting ability and functionality in the cytosol and cilia of NIH-3T3 cells.**

To determine the targeting efficiency of each CTS-tagged GECI, cells expressing each construct were serum starved to induce ciliogenesis and stained with anti-acetylated tubulin as a cilia marker. The targeting efficiency for each CTS-tagged GECI was computed as the percentage of acetylated tubulin positive cilia expressing co-localization of the given construct. The computed percentages for each CTS-tagged GECI were based on  $n \geq 20$ , from 2 independent trials, for each construct. To determine the cytosolic signal dynamic range of each CTS-tagged GECI, cells expressing each construct were treated with 1  $\mu$ M ionomycin and their response was recorded.

The average maximum percentage change in fluorescence/FRET in the cytosol of cells was calculated based on n=7, n=2, n=6, n=6, n=6, and n=4, all from 2 independent trials, for 5HT<sub>6</sub>-YC3.60, 5HT<sub>6</sub>-GCaMP, 5HT<sub>6</sub>-G-GECO1.0, IA-G-GECO1.0, TNXXL-CTS20, and TNXXL-CTS68, respectively. To determine the ciliary signal dynamic range of each CTS-tagged GECI, cells expressing each of the selected constructs in cilia were treated with 2  $\mu$ M Ionomycin and their response was measured. All fluorescence/FRET values were normalized to average baseline values measured prior to Ionomycin addition. The average maximum percentage change in fluorescence/FRET in cilia was calculated based on n=10, n=13, and n=9, respectively for 5HT<sub>6</sub>-YC3.60, 5HT<sub>6</sub>-G-GECO1.0, and IA-G-GECO1.0.

# Chapter 4 Phosphoinositides dictates function and structure identity of primary cilia

## 4.1 Overview

The association of phosphoinositide phosphatases and kinases with primary cilia suggests that phosphoinositides could play an integral role in cilia physiology. We first determined the phosphoinositide composition in primary cilia of several mammalian cell types. Whilst PI(4,5)P<sub>2</sub> is a major molecular identifier of the plasma membrane, we discovered that PI(4,5)P<sub>2</sub> is strictly restricted at the proximal base of the ciliary membrane. We found that this sharp PI(4,5)P<sub>2</sub> gradient is established by cilia-enriched Inpp5e (Section 4.2.1) (Garcia-Gonzalo et al., 2015). In a collaborative work with Jeremy Reiter's laboratory at University of California, San Francisco, we found that PI(4,5)P<sub>2</sub> depletion in ciliary membrane is required for proper ciliary transduction of Hh signals (Section 4.2.2) (Garcia-Gonzalo et al., 2015). Since Inpp5e has been implicated in cilia stability and extracellular vesicle formation through genetic studies, we proceed to study the role of phosphoinositides in regulating ciliary vesicle release and cilia disassembly (Section 4.2.3 onwards). We demonstrate that basal restriction of ciliary structure dynamics is established by the cilia-enriched phosphoinositide 5-phosphatase, Inpp5e. Growth induction displaces ciliary Inpp5e and accumulates PI(4,5)P<sub>2</sub> in distal cilia. This change triggers otherwise-forbidden actin polymerization in primary cilia, which excises cilia tips in a process we call cilia decapitation. While cilia disassembly is traditionally thought to occur solely through resorption, we show that an acute loss of IFT-B through cilia decapitation precedes resorption. Finally, we propose that cilia decapitation induces mitogenic signaling and constitutes a molecular link between the cilia life cycle and cell-division cycle. This newly defined ciliary mechanism may find significance in cell proliferation control during normal development and cancer (Phua et al., 2017). More



fundamentally, these works demonstrate that phosphoinositides play pivotal roles in defining the function and structure identity of primary cilia.

## 4.2 Results

### 4.2.1 Inpp5e regulates ciliary phosphoinositides

To investigate whether specific phosphoinositides localize to cilia, we expressed phosphoinositide-binding domains fused to fluorescent proteins in ciliated cells (Hammond and Balla, 2015). Unlike sensors for PI(3)P, PI(5)P, PI(3,4)P<sub>2</sub>, PI(3,5)P<sub>2</sub> and PI(3,4,5)P<sub>3</sub>, a PI(4)P-specific sensor, EGFP-2×P4M<sup>SidM</sup> (Hammond et al., 2014), was enriched in cilia (**Figure 4-1A** and data not included). EGFP-2×P4M<sup>SidM</sup> was present in 74±4% of IMCD3 cilia. Linescans of ten such cilia reflect the presence of PI(4)P throughout the ciliary membrane (**Figure 4-1B**). Whereas PI(4)P was present along the length of cilia, a PI(4,5)P<sub>2</sub> sensor (EYFP-PH<sup>PLCδ1</sup>) (Stauffer et al., 1998) localized to the proximal end of NIH 3T3 and IMCD3 cilia (**Figures 4-1C,E**). EYFP-PH<sup>PLCδ1</sup> fluorescence ceased at a sharp boundary near the ciliary base (**Figure 4-1D**). To confirm that EYFP-PH<sup>PLCδ1</sup> fluorescence reflected PI(4,5)P<sub>2</sub> distribution, we targeted Inp54p, a yeast enzyme that specifically converts PI(4,5)P<sub>2</sub> to PI(4)P, to cilia by fusing it to a ciliary GPCR (Serotonin Receptor 6, 5HT<sub>6</sub>) (Johnson et al., 2008; Lin et al., 2013; Suh et al., 2006; Tsujishita et al., 2001). Coexpression of 5HT<sub>6</sub>-EYFP-Inp54p with a PI(4,5)P<sub>2</sub> sensor (mCerulean3-PH<sup>PLCδ1</sup>) reduced mCerulean fluorescence at the ciliary base (**Figures 4-1E-F**). A catalytically inactive version, 5HT<sub>6</sub>-EYFP-Inp54p(D281A), did not affect mCerulean3-PH<sup>PLCδ1</sup> localization (**Figures 4-1E-F**) (Suh et al., 2006). Conversely, targeting PI(4)P 5-kinase, type Iγ (PIPK) to cilia by fusing it to 5HT<sub>6</sub> expanded mCerulean3-PH<sup>PLCδ1</sup> localization to the length of the cilium (**Figures 4-1E-F**) (Suh et al., 2006; Ueno et al., 2011). A catalytically inactive version, 5HT<sub>6</sub>-EYFP-PIPK(D253A), had no effect on mCerulean3-PH<sup>PLCδ1</sup> localization (**Figures 4-1E-F**) (Ueno et al.,

2011). Together, these data indicate that the ciliary membrane contains PI(4)P along its length, and PI(4,5)P<sub>2</sub> proximally.

Because Inpp5e can convert PI(4,5)P<sub>2</sub> into PI(4)P, we hypothesized that Inpp5e affects the relative levels of these lipids in the ciliary membrane. To test this hypothesis, we derived mouse embryonic fibroblasts (MEFs) from *Inpp5e*<sup>+/-</sup> and *Inpp5e*<sup>-/-</sup> embryos (Jacoby et al., 2009). As expected, Inpp5e was present in the cilia of *Inpp5e*<sup>+/-</sup> but not *Inpp5e*<sup>-/-</sup> MEFs (**Figure 4-1H**). To assess whether Inpp5e affects PI(4)P distribution, we examined the localization of the PI(4)P probe, EGFP-2×P4M<sup>SidM</sup>, in *Inpp5e*<sup>+/-</sup> and *Inpp5e*<sup>-/-</sup> MEFs. EGFP-2×P4M<sup>SidM</sup> localization to cilia was severely reduced in *Inpp5e*<sup>-/-</sup> MEFs, further suggesting that EGFP-2×P4M<sup>SidM</sup> distribution accurately reflects PI(4)P distribution and indicating that Inpp5e is important for generating ciliary PI(4)P (**Figures 4-1I-J**).

As Inpp5e has the ability to remove the 5-phosphate from PI(4,5)P<sub>2</sub>, we hypothesized that it regulates ciliary PI(4,5)P<sub>2</sub> levels. To test this, we expressed mCerulean3-PHPLCδ1, a PI(4,5)P<sub>2</sub> probe, in *Inpp5e*<sup>+/-</sup> and *Inpp5e*<sup>-/-</sup> MEFs. Similar to NIH-3T3 and IMCD3 cells, *Inpp5e*<sup>+/-</sup> MEFs localized mCerulean3-PHPLCδ1 at the proximal cilium (**Figures 4-1K-L**). In contrast, *Inpp5e*<sup>-/-</sup> MEFs localized mCerulean3-PHPLCδ1 along the entire length of the ciliary membrane (**Figures 4-1K-L**). Thus, Inpp5e limits ciliary PI(4,5)P<sub>2</sub> and generates ciliary PI(4)P, consistent with a role in converting PI(4,5)P<sub>2</sub> to PI(4)P within cilia.

To test whether the expanded ciliary PI(4,5)P<sub>2</sub> in *Inpp5e*<sup>-/-</sup> MEFs reflects loss of ciliary PI(4,5)P<sub>2</sub> 5-phosphatase activity, we examined whether targeting the yeast PI(4,5)P<sub>2</sub> 5-phosphatase Inp54p to cilia lacking Inpp5e restored normal ciliary PI(4,5)P<sub>2</sub> levels. 5HT<sub>6</sub>-EYFP-Inp54p, but not the catalytically inactive 5HT<sub>6</sub>-EYFP-Inp54p(D281A), restored the ciliary exclusion of mCerulean3-PHPLCδ1 in *Inpp5e*<sup>-/-</sup> MEFs (**Figure 4-1M**). These results further suggest that Inpp5e dephosphorylates ciliary PI(4,5)P<sub>2</sub> to restrict it to the proximal cilium.

#### **4.2.2 Phosphoinositides regulate ciliary protein trafficking to modulate Hedgehog signaling**

Using the results presented in section 4.2.1, we collaborated with Hh signaling experts, Francesc Garcia-Gonzalo and Jeremy Reiter at UCSF to study the role of *Inpp5e* and phosphoinositides in regulating ciliary transduction of Hh signals. In the absence of *Inpp5e*, we found that Hh signaling is disrupted. *Inpp5e* limits ciliary levels of the orphan GPCR, *Gpr161*, and the PI(4,5)P<sub>2</sub>-binding protein, *Tulp3*, both of which are negative regulators of Hh signaling. Increasing ciliary PI(4,5)P<sub>2</sub> levels via (i) *Inpp5e* genetic ablation or (ii) expressing 5HT<sub>6</sub>-EYFP-PIPK (which constitutively converts PI(4)P to PI(4,5)P<sub>2</sub> in ciliary membrane) increases the ciliary localization of *Tulp3*. Similarly, conferring the ability to bind PI(4)P on *Tulp3* via fusion EGFP-P4M<sup>SidM</sup> promotes the accumulation of *Tulp3* in primary cilia. The lower level of *Tulp3* in cells lacking *Inpp5e* reduces ciliary *Gpr161* levels and restores Hh signaling. Overall, a depletion of PI(4,5)P<sub>2</sub> in primary cilia is essential for proper ciliary transduction of Hh signals (**Figure 4-2**), and this demonstrates a role for phosphoinositides in defining the function identity of primary cilia. Details of this work are published in (Garcia-Gonzalo et al., 2015).

#### **4.2.3 *Inpp5e* loss and growth stimulation promote ciliary vesicle release**

Since *Inpp5e* is implicated in cilia stability and extracellular vesicle formation (Bielas et al., 2009; Jacoby et al., 2009), we compared ciliary vesicle release in *Inpp5e*<sup>+/-</sup> and *Inpp5e*<sup>-/-</sup> mouse embryonic fibroblasts (MEFs) (Garcia-Gonzalo et al., 2015). Fluorescent protein (FP)-tagged ciliary membrane markers (5HT<sub>6</sub> or *Arl13b*) enabled live-cell visualization of ciliary vesicle release, and primary cilia were induced by culturing cells in 0-0.1% fetal bovine serum (FBS) for 24-48 hours to attain quiescence. We first looked at NIH/3T3, hTERT RPE-1 and mIMCD-3, and occasionally observed release of ciliary vesicles from distal cilia of these cell lines (**Figures 4-3A-B and 4-4A**). In quiescent *Inpp5e*<sup>+/-</sup> and *Inpp5e*<sup>-/-</sup> MEFs, the length of *Inpp5e*<sup>-/-</sup> cilia was

shorter than *Inpp5e*<sup>+/-</sup> cilia and displayed a higher tendency of bulging at ciliary tips (**Figures 4-4B, D-F**). The percentage of ciliation was also lower in *Inpp5e*<sup>-/-</sup> MEF, which displayed an accelerated cilia disassembly rate than *Inpp5e*<sup>+/-</sup> MEF (**Figures 4-4B-C, G**). Ciliary vesicle release was observed in quiescent *Inpp5e*<sup>+/-</sup> MEF with a low three-hour occurrence of  $23.8 \pm 1.5\%$  (mean  $\pm$  SEM), while a complete loss of Inpp5e resulted in a higher three-hour occurrence of  $68.3 \pm 6.3\%$  (mean  $\pm$  SEM) (**Figures 4-3C-D**). Released ciliary vesicles frequently associate with the cell surface and could be traced in fixed cell samples as Arl13b-positive and acetylated tubulin (Ac tub)-negative particles which were harbored by a higher proportion of *Inpp5e*<sup>-/-</sup> MEF than *Inpp5e*<sup>+/-</sup> MEF (**Figures 4-3E-G, 4-4H**). These data demonstrate a role of Inpp5e in modulating ciliary vesicle release.

We next assessed the effect of growth stimulation on ciliary vesicle release. A three-hour 10% FBS treatment on *Inpp5e*<sup>+/-</sup> MEF stimulated ciliary vesicle release in  $65.5 \pm 5.3\%$  of total cells (mean  $\pm$  SEM), but the same treatment on *Inpp5e*<sup>-/-</sup> MEF did not additionally induce a higher occurrence of ciliary vesicle release (**Figures 4-3C-D**). To further demonstrate the effect of growth signals on extracellular ciliary vesicle release, culture media conditioned for twenty-four hours with quiescent (0-0.1% FBS) or growth-stimulated (10% FBS) mIMCD-3 cells were analyzed for ciliary markers (**Figure 4-11D**). Growth stimulation of mIMCD-3 resulted in significantly larger amounts of Arl13b detected in conditioned culture media, whereas extracellular levels of  $\alpha$ -tubulin and GADPH were low and unaffected by growth stimulation (**Figures 4-3H-I, 4-4I-J**). Ciliary vesicle release is thus promoted by Inpp5e loss and growth stimulation. Since this process occurs through an excision of primary cilia tips, we hereon refer to this process as cilia decapitation.

#### **4.2.4 Growth-stimulated cilia decapitation entails ciliary Inpp5e depletion and PI(4,5)P<sub>2</sub> re-distribution**

We next investigated growth stimulation-Inpp5e interplay. A four-hour 10% FBS stimulation to quiescent *Inpp5e*<sup>+/-</sup> MEF depleted endogenous Inpp5e in primary cilia (**Figures 4-5A-B**). To probe the functional role of Inpp5e on cilia decapitation, we targeted exogenous Inpp5e to primary cilia through fusion with a ciliary membrane marker and assessed the effect on cilia decapitation. As compared with 5HT<sub>6</sub>-YFP, 5HT<sub>6</sub>-YFP-Inpp5e(WT) reduced the proportion of *Inpp5e*<sup>+/-</sup> MEF harboring extracellular YFP-labeled ciliary vesicles over a four-hour 10% FBS stimulation, while 5HT<sub>6</sub>-YFP-Inpp5e(D477N; phosphatase-dead(PD)) did not exert similar effect (**Figures 4-6A-B**). In quiescent *Inpp5e*<sup>-/-</sup> MEF, 5HT<sub>6</sub>-YFP-Inpp5e(WT) also exerted a stronger repressive effect on ciliary vesicle formation than 5HT<sub>6</sub>-YFP-Inpp5e(PD) (**Figures 4-6A-B**). Overall, these results show that Inpp5e functions as a decapitation repressor in primary cilia.

Since AurA is essential for cilia disassembly (Pugacheva et al., 2007), we examined if inhibition of AurA and its downstream effector, HDAC6, could affect ciliary Inpp5e. AurA inhibition using alisertib (Ast) countered growth-stimulated ciliary Inpp5e depletion, whereas HDAC6 inhibition using tubacin (Tub) did not (**Figures 4-6E-F**). In addition, AurA was responsible for cilia decapitation, with alisertib treatment suppressing growth-stimulated ciliary vesicle release in *Inpp5e*<sup>+/-</sup> MEF (**Figure 4-6G**). Although HDAC6 does not regulate Inpp5e localization, tubacin treatment did exert a mild effect on ciliary vesicle release in *Inpp5e*<sup>+/-</sup> MEF (**Figure 4-6G**), implying that HDAC6-mediated deacetylation of ciliary microtubules could indirectly affect cilia decapitation. Notably, neither alisertib nor tubacin inhibited ciliary vesicle release in *Inpp5e*<sup>-/-</sup> MEF (**Figure 4-6G**). The concomitant Inpp5e absence and AurA-independent cilia decapitation in *Inpp5e*<sup>-/-</sup> MEF supports that cilia tip excision requires ciliary Inpp5e depletion. Thus, growth-stimulated AurA activity drives Inpp5e depletion in primary cilia as well as cilia decapitation.

A net Inpp5e reduction in primary cilia could result in a lower capacity to deplete PI(4,5)P<sub>2</sub>. Whilst PI(4,5)P<sub>2</sub> was confined within the proximal half of cilia in quiescent *Inpp5e*<sup>+/-</sup> MEF

(**Figures 4-5C-D and 4-6H** (Garcia-Gonzalo et al., 2015)), a 10% FBS stimulation for two hours or more led to PI(4,5)P<sub>2</sub> accumulation in distal half of *Inpp5e*<sup>+/-</sup> cilia, concomitant with cilia decapitation (**Figures 4-5E-F and 4-6I-K**). Decapitation primarily occurred in cilia with PI(4,5)P<sub>2</sub> accumulating to the distal half of ciliary length, and the position of cilia excision was correlated with the maximal ciliary PI(4,5)P<sub>2</sub> accumulation prior to decapitation (**Figures 4-5G-H**). Interestingly, cilia decapitation was often followed by wide oscillations in ciliary PI(4,5)P<sub>2</sub> accumulation, which suggests bi-directional regulation between PI(4,5)P<sub>2</sub> and cilia decapitation (**Figures 4-5E-F and 4-6J-K**). Thus, growth-stimulated PI(4,5)P<sub>2</sub> redistribution in primary cilia could organize signalling events leading to cilia decapitation.

#### 4.2.5 Ciliary PI(4,5)P<sub>2</sub> induces F-actin in ciliary lumen

Since PI(4,5)P<sub>2</sub> re-organization could affect ciliary localization of actin regulators, we inspected F-actin formation in primary cilia of *Inpp5e*<sup>+/-</sup> and *Inpp5e*<sup>-/-</sup> MEF using mCerulean3(mCeru3)-Lifeact biosensor. Of note, an elevated steady state of ciliary PI(4,5)P<sub>2</sub> in *Inpp5e*<sup>-/-</sup> MEF was associated with a tenfold increase in the probability of detecting Lifeact-positive structures in primary cilia of quiescent cells (**Figures 4-7A-B**). We also performed three-dimensional super-resolution structured illumination microscopy on cells stained with phalloidin, and detected similar phalloidin-labelled structures within ciliary lumen that was juxtaposed with the microtubule axoneme (**Figure 4-8A**). Direct PI(4,5)P<sub>2</sub> amplification by targeting constitutively active PI(4)P 5-kinase I $\gamma$  (PIPK) to cilia (5HT<sub>6</sub>-FP-PIPK (Garcia-Gonzalo et al., 2015)) was similarly associated with a higher frequency of intraciliary F-actin than cilia-targeted kinase-dead PIPK (5HT<sub>6</sub>-FP-PIPK (D253A; KD)) (**Figures 4-7A-B and 4-8B-C**). Therefore, ciliary PI(4,5)P<sub>2</sub> exerts direct control on intraciliary F-actin assembly. A screen for actin regulators further revealed PI(4,5)P<sub>2</sub>-dependent ciliary localization of cofilin-1, fascin and Kras small GTPase that could work together to induce actin polymerization in primary cilia (**Figures 4-8B-G**).

#### 4.2.6 Intraciliary actin polymerization is required for cilia decapitation

We investigated F-actin involvement in cilia decapitation. By monitoring *Inpp5e*<sup>+/-</sup> and *Inpp5e*<sup>-/-</sup> MEF over two-hour periods during quiescence, or between zero and six hours of growth stimulation, we detected F-actin assembly at the site of cilia excision (**Figures 4-7C-D and 4-9A-I**). These intraciliary actin polymerization events were acute and transient, occurring a few minutes prior to each decapitation event (**Figures 4-7C-D and 4-9H-I**). Furthermore, growth-stimulated *Inpp5e*<sup>-/-</sup> MEF tend to assemble larger intraciliary F-actin foci than quiescent *Inpp5e*<sup>-/-</sup> MEF and growth-stimulated *Inpp5e*<sup>+/-</sup> MEF, suggesting stronger actin polymerization that was associated with cilia excision occurring at more proximal positions (**Figures 4-9B-C**).

Next, we determined the essentiality of F-actin in cilia decapitation. Latrunculin A restricted growth-stimulated ciliary vesicle release in *Inpp5e*<sup>+/-</sup> and *Inpp5e*<sup>-/-</sup> MEF, indicating that whole-cell F-actin turnover affects membrane excision in primary cilia (**Figures 4-7E-F**). Additionally, we devised a genetic strategy to suppress intraciliary F-actin by targeting thymosin  $\beta$ 4 (T $\beta$ 4) to primary cilia, which sequesters G-actin from incorporation into actin filaments (Van Troys et al., 1996). As compared with 5HT<sub>6</sub>-YFP, 5HT<sub>6</sub>-YFP-T $\beta$ 4(WT) expression robustly suppressed ciliary vesicle formation in quiescent *Inpp5e*<sup>-/-</sup> MEF, as well as in *Inpp5e*<sup>+/-</sup> MEF over a four-hour growth stimulation period (**Figures 4-7G-H**). In contrast, 5HT<sub>6</sub>-YFP-T $\beta$ 4(KK18,19EE; actin-binding mutant MT (Van Troys et al., 1996)) expression did not exert similar effect. Thus, intraciliary actin polymerization is essential for cilia decapitation, and suppression could be achieved via a genetically-encoded ciliary actin inhibitor.

We then attempted to determine factors that regulate F-actin to promote ciliary membrane excision. Myosin II Inhibition with blebbistatin suppressed growth-stimulated ciliary vesicle release in *Inpp5e*<sup>+/-</sup> and *Inpp5e*<sup>-/-</sup> MEF (**Figures 4-7E-F**). We also explored sorting nexin 9 (SNX9), as the molecule was detected in the proteomic profile of ciliary vesicles described in the following section. Previous reports demonstrate SNX9 as a PI(4,5)P<sub>2</sub> and PI(3,4)P<sub>2</sub> binder which couples actin assembly with membrane remodelling at endocytic sites (Posor et al., 2013; Yazar et

al., 2007). Accordingly, we observed accumulation of YFP-SNX9 in the vicinity of cilia excision site, shortly before cilia decapitation occurred in *Inpp5e*<sup>+/-</sup> MEF (23/23; 100% of decapitation events) (**Figures 4-9J-K**). These results suggest a role of actomyosin contractility and SNX9-mediated actin nucleation in cilia decapitation.

#### **4.2.7 Released ciliary vesicles contain IFT-B and related cargoes**

We dissected the contents of ciliary vesicles released into the extracellular milieu. Global proteomic profiling and comparative analyses were performed on culture media conditioned for twenty-four hours with quiescent (0.1% FBS) and growth-stimulated (10% FBS) wild-type (WT) or cilia-deficient *Ift88*-knockout (*Ift88*-KO) mIMCD-3 (**Figures 4-10 and 4-11A-E**), and we identified 1376 proteins that were detected two times or more in conditioned media of at least one experiment condition (**Figure 4-10A; Table 4-1**). Within this list, 477 represent proteins that were extracellularly released with growth stimulation, and 71 are indicative of proteins that were extracellularly released depending on functional cilia (**Figure 4-10A**; see legend for details). A 57-protein overlap between these two categories revealed putative ciliary vesicle components, which consist of a large majority of intraflagellar transport-related proteins, a subset of ciliary proteins, and Hedgehog signaling effectors (**Figure 4-10B; Table 4-1**). On average, identified IFT-B components were ranked higher than IFT-A components in terms of the relative abundance between growth-stimulated WT and *Ift88*-KO mIMCD-3 culture media pellets (**Figures 4-10C-D; Table 4-2**). At the protein level, larger amounts of Arl13b, Ift88 and Ift81 (IFT-B components) were indeed detected in conditioned media pellets from growth-stimulated WT mIMCD-3 than from quiescent WT mIMCD-3 or growth-stimulated *Ift88*-KO mIMCD-3, whereas Ift122 and Ift140 (IFT-A components) were scarcely detected in conditioned media pellets from both conditions (**Figures 4-10E-F**). This confirms that growth-stimulated ciliary vesicle release removes IFT-B, rather than IFT-A, from primary cilia. We also validated extracellular accumulation of Sufu and full-length Gli3 (Gli3FL) in conditioned media pellets of



growth-stimulated WT mIMCD-3, while Gli2 and a truncated form of Gli3 (Gli3R) were hardly detected (**Figures 4-10E-F**).

We proceeded to understand the mechanism for relative IFT-B enrichment in released ciliary vesicles. In quiescent cells, Ift140(IFT-A) and Ift81(IFT-B) were detected along ciliary shafts of *Inpp5e*<sup>+/-</sup> and *Inpp5e*<sup>-/-</sup> MEF, with *Inpp5e*<sup>-/-</sup> primary cilia harboring high enrichment of Ift140 as previously reported (**Figures 4-11F-G**) (Garcia-Gonzalo et al., 2015). Interestingly, a four-hour 10% FBS stimulation led to increased ciliary Ift81 in *Inpp5e*<sup>+/-</sup> and *Inpp5e*<sup>-/-</sup> MEF, while ciliary Ift140 underwent reduction in both cell types (**Figures 4-11F-G**). In a mIMCD-3 cell line with endogenous Ift81 tagged with yellow Nano-lantern (YNL) (**Figures 4-11H-J**), Ift81-YNL signals were detected throughout the ciliary shaft at quiescence, with stronger accumulation in proximal cilia (**Figure 4-11K**). A four-hour growth stimulation not only elevated the overall Ift81-YNL in primary cilia, but also slightly shifted Ift81-YNL distribution towards the distal cilia (**Figures 4-11K-O**). Thus, an IFT-B increase with a complementary IFT-A decrease could potentially account for the selective release of IFT-B from primary cilia upon ciliary vesicle release.

#### 4.2.8 Cilia decapitation is required for cilia disassembly

Cilia decapitation culminates in an acute loss of ciliary proteins that may compromise cilia stability. Likewise, *Inpp5e* loss triggers accelerated cilia instability upon growth stimulation (**Figure 4-4G**) (Bielas et al., 2009; Jacoby et al., 2009). We therefore investigated the functional consequences of decapitation in *Inpp5e*<sup>+/-</sup> and *Inpp5e*<sup>-/-</sup> MEF ciliary resorption. In growth-stimulated *Inpp5e*<sup>+/-</sup> MEF expressing 5HT<sub>6</sub>-YFP, the lengths of intact primary cilia were maintained (Decap<sup>-</sup> in 10% FBS; **Figures 4-12A-B**), while decapitated cilia underwent significant resorption within three hours post-decapitation (Decap<sup>+</sup> in 10% FBS; **Figures 4-12A-B**). Consistently, growth-stimulated *Inpp5e*<sup>+/-</sup> primary cilia inhibited for decapitation via 5HT<sub>6</sub>-YFP-Tβ4(WT) expression were also suppressed for resorption (Decap<sup>+</sup> in 10% FBS Tβ4(WT); **Figures 4-12A-B**). Thus, decapitation is necessary for cilia resorption induced by growth

stimulation. In *Inpp5e* absence, growth-stimulated cilia decapitation in *Inpp5e*<sup>-/-</sup> MEF was accompanied with a greater extent of cilia resorption as compared with *Inpp5e*<sup>+/-</sup> counterpart (Decap+ in 10% FBS; **Figures 4-12A-C**). Cilia decapitation in quiescent *Inpp5e*<sup>-/-</sup> MEF was also sufficient to activate cilia resorption within three hours post-decapitation, albeit to a smaller extent than in growth stimulated events (Decap+ in 0% FBS; **Figures 4-12A-C**). Thus, cilia resorption post-decapitation was amplified in the absence of *Inpp5e*.

We further probed the role of decapitation on the extent of ciliation in *Inpp5e*<sup>+/-</sup> and *Inpp5e*<sup>-/-</sup> MEF expressing 5HT<sub>6</sub>-YFP, 5HT<sub>6</sub>-YFP-Tβ4(WT) and 5HT<sub>6</sub>-YFP-Tβ4(MT) at zero, six and twenty hours of 10% FBS stimulation. While a similar proportion of cells were ciliated at zero hour across all three conditions, a larger proportion of 5HT<sub>6</sub>-YFP-Tβ4(WT)-expressing cells harbored primary cilia at six and twenty hours of growth stimulation (**Figures 4-12D-G**). Thus, ciliary actin inhibition suppressed cilia decapitation that was required for cilia disassembly. Moreover, the observed role of 5HT<sub>6</sub>-YFP-*Inpp5e*(WT) in suppressing growth-stimulated cilia disassembly underscores how *Inpp5e* controls the disassembly process (**Figures 4-6C-D**).

#### 4.2.9 Cilia decapitation ensures timely quiescence exit

Since growth stimulation of quiescent cells would induce cell cycle entry, we determined the timing of cilia decapitation in relation to cell cycle. Co-expression of Venus-p27K<sup>-</sup> (a G<sub>0</sub> marker) and mCherry-hCdt1(30/120) (a G<sub>0</sub>/G<sub>1</sub> marker) enables cells in G<sub>0</sub>, G<sub>1</sub> or S phase to be respectively labelled with Venus/mCherry, mCherry only, or null nuclear fluorescence (Oki et al., 2014). G<sub>0</sub>-G<sub>1</sub> transit will be manifested as a steep decrease in Venus-p27K<sup>-</sup>, while G<sub>1</sub>-S transit will be marked by a subsequent abrupt decrease in mCherry-hCdt1(30/120). By considering the relative expression ratio of Venus-p27K<sup>-</sup> and mCherry-hCdt1(30/120), we arbitrarily defined Venus-p27K<sup>-</sup>/mCherry-hCdt1(30/120) = 0.5 as the mid-point of G<sub>0</sub>-G<sub>1</sub> transit.

We expressed these cell cycle probes in *Inpp5e*<sup>+/-</sup> MEF with either 5HT<sub>6</sub>-mCeru3 or 5HT<sub>6</sub>-mCeru3-Tβ4(WT), and subjected quiescent cells to a ten-hour growth stimulation. In 5HT<sub>6</sub>-mCeru3-expressing cells, 20/25 (80%) cells underwent at least a single cilia decapitation event (**Figures 4-13A-B and 4-14A-B**). Out of these 20 cells, 19 (95%) of them exhibited the first cilia decapitation event prior to G<sub>0</sub>-G<sub>1</sub> transit, while one cell underwent cilia decapitation during the transit (**Figures 4-13A-B and 4-14A**). Thus, growth stimulation at quiescence induces cilia decapitation in G<sub>0</sub> phase. We further compared the time taken by cells with intact or decapitated primary cilia to reach the G<sub>0</sub>-G<sub>1</sub> transit midpoint upon growth stimulation. Within the cell population which exhibited at least one cilia decapitation event at quiescence, 15/20 (75%) cells were determined to exit quiescence within ten hours of growth stimulation (i.e. these cells demonstrated a sharp decrease in Venus-p27K<sup>-</sup> at some point), and they took an average time of  $5.7 \pm 0.4$  hours to reach the G<sub>0</sub>-G<sub>1</sub> transit mid-point (**Figures 4-13A, B, E and 4-14A**). In contrast, 7/10 (70%) of 5HT<sub>6</sub>-mCeru3-Tβ4(WT)-expressing cells suppressed for cilia decapitation were either not determined for quiescence exit (43% (3/7)), or took a prolonged time of  $8.9 \pm 0.4$  hours to reach G<sub>0</sub>-G<sub>1</sub> transit mid-point (57% (4/7)) (**Figures 4-13C-E and 4-14D**). Thus, cilia decapitation is required by quiescent cells for timely G<sub>1</sub> entry.

#### **4.2.10 Cilia decapitation modulates Gli transcription factor activity**

We speculated that cilia decapitation might promote quiescence exit through mitogenic Hedgehog (Hh) signaling (Roy and Ingham, 2002). We established an NIH/3T3 cell line stably expressing a GFP reporter driven by a minimal promoter and 8xGli-Binding-Site (GBS) sequence to measure Gli1/2 (but not Gli3) transcription activity in single cells (Sasaki et al., 1997; Stamatakis et al., 2005). This reporter cell line was transfected with either 5HT<sub>6</sub>-tagRFP, 5HT<sub>6</sub>-tagRFP-Tβ4(WT) or 5HT<sub>6</sub>-tagRFP-Tβ4(MT) prior to quiescence induction, and Gli1/2 activity in these cells was measured in response to growth stimulation (20% FBS) or Smoothed (Smo)-dependent Hh activation (SAG; Smo agonist). All three groups of cells similarly expressed a low basal level of

GFP at quiescence (**Figures 4-15A-B**). In SAG positive controls, a modest increase in GFP fluorescence was detected at eight hours post-stimulation across these cells, which robustly increased by twenty-four hours (**Figures 4-15A-B**). Remarkably, an eight-hour growth stimulation induced an intermediate GFP fluorescence increase in 5HT<sub>6</sub>-tagRFP-expressing cells that was accompanied by an average decrease in cilia length (**Figures 4-15A-C**). Similar observations were made for 5HT<sub>6</sub>-tagRFP-Tβ4(MT)-expressing cells, whereas 5HT<sub>6</sub>-tagRFP-Tβ4(WT)-expressing cells, which were suppressed for cilia decapitation, exhibited neither comparable changes in GFP fluorescence nor cilia length (**Figures 4-15A-C**). Moreover, Smo inhibitor, Vismodegib was able to abolish the GFP fluorescence increase in SAG-induced conditions but not in FBS-treated conditions (**Figures 4-15D-E**). We also verified that an eight-hour treatment with 20% FBS did not promote Smo translocation into primary cilia (**Figures 4-15F-G**). Overall, these results implied a Smo-independent role of cilia decapitation in growth-induced Gli1/2 activation. To further verify this, we assessed how the expression of general Hh targets *Gli1* and *Ptch1* were affected by growth stimulation. Control treatment with SAG induced a robust increase in *Gli1* and *Ptch1* gene expression in NIH/3T3 at eight hours. Interestingly, an approximately two-fold increase in *Ptch1* gene expression was observed in NIH/3T3 cells at eight hours post-stimulation with 10% FBS, while no change was observed for *Gli1* gene (**Figure 4-15H**). Growth-induced *Ptch1* expression supports an increase in Gli1/2 activity. Lastly, a lack of *Gli1* gene up-regulation suggests that Gli1 activation upon growth stimulation would likely occur at the post-transcriptional level.

### 4.3 Discussion

Phosphoinositides are principal molecular identifiers in many intracellular compartments (Shewan et al., 2011). Here, we demonstrate that the function and structure identities of primary cilia are established by an active depletion of PI(4,5)P<sub>2</sub>. Inpp5e establishes a basal restriction of PI(4,5)P<sub>2</sub> for a proper distribution of ciliary proteins required to transduce Hedgehog signals

(**Figure 4-2**). Concomitantly, PI(4,5)P<sub>2</sub> restriction suppresses the capacity for primary cilia to polymerize actin filaments. We demonstrate that growth stimulation offsets this restriction for actin polymerization to occur in primary cilia. F-actin-powered cilia decapitation not only triggers resorption of the ciliary structure, but also regulates proliferative signaling which connects the cilia life cycle and cell division cycle (**Figure 4-15I**).

#### *The molecular players of cilia decapitation*

Inpp5e and HDAC6 act in complementary pathways downstream of AurA to disassemble the ciliary structure. Earlier work determined that AurA phosphorylates Inpp5e to modulate its 5-phosphatase activity (Plotnikova et al., 2014), and we discovered that AurA also dictates Inpp5e re-localization. It is therefore tempting to speculate that phosphorylated Inpp5e may have altered affinity against binding partners which coordinate its ciliary localization (Humbert et al., 2012). Within the primary cilia, Inpp5e functions as a rheostat which tunes PI(4,5)P<sub>2</sub> required for actin polymerization. The resultant assembly of F-actin in distal cilia could be attributed to the presence of a bulky microtubular axoneme which physically obstructs stable F-actin foci organization in the proximal ciliary lumen. Upon growth stimulation, concomitant HDAC6-dependent axonemal resorption and Inpp5e-dependent PI(4,5)P<sub>2</sub> re-distribution could culminate in a position in distal cilia that is devoid of microtubules while harboring PI(4,5)P<sub>2</sub>, permitting stable actin nucleation at that point. Moreover, the tip region of a primary cilium has been revealed as a sub-compartment harboring specific signaling molecules (He et al., 2014). The distal cilia may similarly possess properties promoting actin polymerization, and this is supported by our observed cofilin-1 enrichment in the tips of PI(4,5)P<sub>2</sub>-elevated cilia (**Figures 4-7B, D**).

#### *The functional role of IFT-B elimination in cilia disassembly*

Cilia decapitation could function as a ciliary outlet for IFT-B during cilia disassembly. Many components of IFT-B are associated with cilia growth; Ift81 and Ift74 constitute a tubulin-binding

module which captures and delivers  $\alpha\beta$ -tubulin dimers to the plus end of ciliary axoneme for elongation (Bhogaraju et al., 2013). During the process of cilia resorption, the large pore size (7.9-9nm) of a diffusion barrier positioned at the ciliary base would allow rapid diffusion of resorbed IFT-B constituents from the cytosol back into the ciliary lumen to result in inappropriate cilia re-growth (Breslow et al., 2013; Lin et al., 2013). Acute removal of IFT-B from primary cilia through decapitation could limit cilia re-growth, thereby playing an active, facilitating role in cilia disassembly. Up-regulation of the ciliary IFT-B/IFT-A ratio by growth stimulation could enhance IFT-B removal from ciliary tips, and could involve the serine/threonine protein kinase ICK, which is a candidate ciliary vesicle component involved in regulating the ciliary anterograde motor, Kif3a (**Figure 4-10C; Table 4-2**) (Chaya et al., 2014).

#### *Cilia decapitation as a driver of quiescence exit*

In differentiating neural progenitors, primary cilia dismantling as a result of apical abscission terminates mitogenic Hh signals for quiescence entry (Das and Storey, 2014). Conversely, we propose that cilia decapitation enhances Hh signaling to drive quiescence exit. Growth induction likely activates the mTOR signaling pathway in which S6K1 phosphorylates Gli1 to release it from Sufu inhibition (Wang et al., 2012), and active Gli1 could promote downstream cyclin D2 expression which functions in quiescence exit (Susaki et al., 2007; Yoon et al., 2002). Exploring cilia decapitation-mTOR signaling crosstalk thus holds exciting potential for understanding ciliary control of cell cycle, and is motivated by: (i) a role of primary cilia in mTOR signaling suppression via Lkb1 (Boehlke et al., 2010; Orhon et al., 2016) (ii) detection of an mTOR inhibitor, glycogen synthase kinase-3 beta (GSK3B) in ciliary vesicle proteomics (**Figure 4-10C; Table 4-2**) (Inoki et al., 2006). The Smo-independent role of growth stimulation on Gli1 activity is distinct from the Hh signaling repression caused by ciliary accumulation of Smo antagonists with complete Inpp5e loss (Chávez et al., 2015; Garcia-Gonzalo et al., 2015). Future work would

entail understanding how *Inpp5e* loss affects Smo-independent Gli1 regulation, and how growth-induced changes in ciliary PI(4,5)P<sub>2</sub> distribution could affect Smo antagonists in primary cilia.

### *Conclusion*

Taken together, our present work describes a cell-autonomous role of cilia decapitation in cell cycle regulation. Interestingly, earlier proposals characterized ciliary vesicles as signaling devices in algae and worms (Bergman et al., 1975; Cao et al., 2015; Wang et al., 2014, 2015; Wood and Rosenbaum, 2015; Wood et al., 2013). In line with these reports, mammalian primary cilia also associate with extracellular vesicles *in vivo* (Dubreuil et al., 2007; Hogan et al., 2009; Jacoby et al., 2009; Wood and Rosenbaum, 2015). Thus, the vesicles generated from cilia decapitation may engage in signal transmission in a non-cell-autonomous manner, and exhibit potential as diagnostic readouts in development and cancer.

## **4.4 Materials and Methods**

### **4.4.1 Cell culture**

We derived MEF from littermate E19.5 *Inpp5e*<sup>+/-</sup> and *Inpp5e*<sup>-/-</sup> embryonic tails using mouse protocols were approved by the Institutional Animal Care and Use Committee (IACUC) at the University of California, San Francisco. Primary MEF were maintained in DMEM, 15% FBS, and PenStrep, and immortalized by infection with a lentivirus expressing SV40 large T antigen.

Immortalized MEF and NIH/3T3 were cultured in DMEM medium containing 10% FBS. mIMCD-3 and hTERT RPE-1 cells were cultured in DMEM/F-12 (1:1; Invitrogen) medium supplemented with 10 % FBS. NIH/3T3-Flp-in: 8xGBS-GFP line was cultured in DMEM medium containing 10% FBS and 2mM GlutaMAX (Gibco). In all experiments, cells were first induced for ciliogenesis by attaining quiescent state with following conditions: NIH/3T3 and MEF were cultured in Opti-MEM® I reduced serum medium (Thermofisher Scientific) with 0% FBS for 24 hours, NIH/3T3-Flp-in: 8xGBS-GFP line was cultured in DMEM containing 2mM

GlutaMAX for 48 hours, and mIMCD-3 and hTERT-RPE1 were cultured in DMEM/F-12 (1:1; Invitrogen) medium containing 0-0.1% FBS for 24 hours. To stimulate growth in quiescent cells, 10-20% FBS were added to respective media depending on cell type. In some experiments, cells were treated with 200nM Alisertib (MedChem Express) and 2 $\mu$ M Tubacin (Cayman Chemical Company). For live cell imaging, cells were plated on poly(d-lysine)-coated borosilicate glass Lab-Tek 8-well chambers (Thermo Scientific).

#### **4.4.2 Transient and stable transfection**

For transient transfection, cells were transfected with the respective DNA constructs by plating them directly in a transfection solution containing DNA plasmids and Xtremegene 9 (Roche).

For Arl13b-GFP stable lines, cells were transfected with Arl13b-pEGFP (Clontech), and stable clones were selected in culture media containing 750 mg/ml G418. The plasmids were transfected using FuGENE HD transfection reagents (Promega) following the manufacturer's instructions.

#### **4.4.3 DNA plasmid construction**

Construction of 5HT<sub>6</sub>-YFP/mCeru3, 5HT<sub>6</sub>-YFP/mCeru3-PIPK, 5HT<sub>6</sub>-YFP/mCeru3-PIPK(KD) were previously reported (Garcia-Gonzalo et al., 2015). To construct 5HT<sub>6</sub>-YFP/mCeru3/tagRFP-T $\beta$ 4(WT), full-length thymosin $\beta$ 4 cDNA was amplified from NIH/3T3 total cDNA using fwd: 5'-TTGG GAATTCGATGTCTGACAAACCCGAT-3' and rev: 5'-CCAAGGATCCCGATTCGCCAGCTTGCTT-3' primers, and inserted into 5HT<sub>6</sub>-YFP/mCeru3/tagRFP using 5' EcoRI and 3' BamHI sites. Thymosin $\beta$ 4 KK18,19EE mutant (T $\beta$ 4(MT)) was subsequently constructed via site-directed mutagenesis using fwd: 5'-TCGATAAGTCGAAGTTGGAGGAAACAGAAACGCAAGAG-3' and rev: 5'-CTCTTGCGTTTCTGTTTC-CTCCAACCTCGACTTATCGA-3' primers. For 5HT<sub>6</sub>-YFP-Inpp5e(WT), the human Inpp5e CaaX domain was first abolished using a C641A mutation to make Inpp5e non-membrane bound, and the catalytic domain was amplified using fwd: 5'-



TTGGGAATTCGCGGATCTTGCAGACTACAAGCTC-3' and rev: 5'-AACCGGATCCTCAAGAAACGGAGGCGATGGTGC-3' primers and inserted into 5HT<sub>6</sub>-YFP using 5' EcoRI and 3' BamHI sites. Inpp5e D477N mutant was constructed via site-directed mutagenesis using fwd: 5'-AGGTGTTCTGGTTTGGAACTTCAACTTCCGCCTGAG-3' and rev: 5'-CTCAGGCGGAAGTTGAAGTTTCCAAACCAGAACACCT-3' primers. PMXs-IP-mVenus-p27K<sup>-</sup> and pCSII-EF-mCherry-hCdt1(30/120) plasmids were kind gifts from Toshio Kitamura and Atsushi Miyawaki respectively.

#### **4.4.4 Generation of *Ift88*-KO mIMCD-3**

*Ift88*-KO mIMCD-3 was generated with a CRISPR/CAS9-based genome editing technique. mIMCD-3 cells were transfected transiently by an all-in-one plasmid harboring CAS9, GFP, and guide RNA, which was available from Sigma-Aldrich. The target sequence of guide RNA was 5'-GGAGGTCTTCTGCCATGAC-3'. Cells expressing CAS9 was sorted next day with a fluorescence-activated cell sorter, ARIA (BD). The sorted cells were cloned in 96-well plate. Screening was performed with western blot analyses. Cells absent for *Ift88* protein signals were further verified by analyzing target site DNA sequence in the genome.

#### **4.4.5 Generation of *Ift81*:YNL knock-in mIMCD-3**

*Ift81*:YNL knock-in mIMCD-3 cell line was generated using CRISPR/CAS9-based genome editing technique. mIMCD-3 cells were co-transfected with an all-in-one plasmid harboring CAS9, GFP, and guide RNA, and a plasmid vector harboring the left arm (834 bp), YNL (1614bp), and right arm (715 bp). The target sequence of gRNA was selected by using an algorithm provided by Broad Institute (<http://portals.broadinstitute.org/gpp/public/analysis-tools/sgrna-design>). The target sequence of guide RNA was 5'-ACAGGGCTCAGAGAACCAGC-3'. Cells expressing CAS9 were sorted next day with a fluorescence-activated cell sorter, ARIA (BD). The sorted cells were cloned in 96-well plate.

Initial screening was performed by PCR with primers: 5'-CAGTTGGCAGTTAAGAAACGGAG-3'; 5'-GTAGTCCACATGGAACAGAGGC-3'. Expression of Ift81-YNL was verified using Western blot analyses with anti-GFP antibody (Medical & Biological Laboratories, Nagoya, Japan).

#### **4.4.6 Generation of NIH/3T3-Flp-In: 8xGBS-GFP and reporter assay**

A minimal promoter and 8xGLI-binding-site (GBS) sequences were inserted upstream of GFP within a pRRL.sin-18.PPT.GFP.pre lentiviral plasmid vector (Monje et al., 2011), and prepared lentiviruses were used to infect NIH/3T3-Flp-In cells (Life Technologies) in the presence of 4 µg/ml polybrene (Sigma). Cells were grown to confluence prior to serum starvation in the presence of 200nM SAG (Enzo Life Sciences) for 24 hours. GFP-expressing cells were single cell sorted into a 96-well plate using FACSaria II (BD Biosciences), and multiple single cell-derived clones were analyzed for SAG-induced GFP expression. For all reporter assay experiments, a specific clone with low basal GFP expression and high SAG-induced GFP expression was used. 40000 cells were seeded into one well of Lab-Tek 8-well chamber (Thermo Scientific), and cells were induced for quiescent state by culturing in serum starvation media (DMEM containing 2mM GlutaMAX) for 48 hours. Afterwards, cells were treated with serum starvation media containing 20% FBS or 200nM SAG (Enzo Life Sciences), in the presence or absence of 1µM Vismodegib (LC labs) for 8 hours or 24 hours. Cells were then fixed with 4% paraformaldehyde at room temperature for 10 mins prior to imaging of reporter GFP expression.

#### **4.4.7 Immunofluorescence**

For most experiments, cells were fixed with 4% (v/v) paraformaldehyde at room temperature for 10 min, permeabilized with 0.1% (v/v) Triton-X100 for 5 min, blocked with 2% bovine serum albumin for 1 hour. Antibodies used are as follows: rabbit anti-Inpp5e (1:500; a kind gift from *Stéphane* Schurmans), rabbit anti-Smo (1:500; as reported in (Rohatgi et al., 2007)) rabbit anti-

Arl13b (1:500; Proteintech 17711-1-AP), mouse anti-acetylated tubulin (1:1000; Sigma, T7451), mouse anti-gamma tubulin (1:1000; Sigma T6557). For immunofluorescence with rabbit anti-Ift81 (1:250; Proteintech, 11744-1-AP), cells were fixed with 4% (v/v) paraformaldehyde for 10 min, prior to -20°C methanol fixation for 3 min. For immunofluorescence with rabbit anti-Ift140 (1:100; Proteintech, 17460-1-AP), cells were fixed with -20°C methanol for 3 min. F-actin probe, Alexa Fluor 488 Phalloidin (ThermoFisher Scientific) was also used.

#### **4.4.8 Epi-fluorescence imaging**

Live-cell imaging experiments were mostly performed using an IX-71 (Olympus) microscope with a 63x oil objective (Olympus) (with additional 1.6x optical zoom) and a Cool-SNAP HQ charge-coupled device camera (Photometrics) or an ORCA-Flash4.0 LT Digital CMOS camera (Hamamatsu). Time-lapse imaging experiments were performed with either 2-min or 5-min intervals, and between 3 and 11 0.5- $\mu$ m z-stacks were taken at each time point. Images shown were mostly maximum intensity projection. Micrographs were taken and analyzed using MetaMorph 7.5 imaging software (Molecular Devices).

#### **4.4.9 Confocal imaging**

Confocal live cell imaging of NIH/3T3 cilia decapitation was performed on FV1000 (Olympus, Japan) equipped with a stage top incubator (Tokai Hit, Japan). Confocal imaging of Arl13b+Actub- particles and live cell imaging of mIMCD-3 and hTERT RPE-1 cilia decapitation were performed using a LSM710 confocal microscope (Carl Zeiss microscopy) equipped with a Plan Aplanachromat 63X oil immersion objective lens (NA 1.4) and processed using Zeiss Zen software. mIMCD-3 ciliary Ift81-YNL signals were visualized via direct 488-nm laser excitation of Venus on SP8 confocal microscope (Leica), and 3D image reconstruction were performed through volume rendering in 3D View software equipped in LAS X (Leica).

#### **4.4.10 Structured illumination microscopy imaging**

3D-SIM imaging was performed on an ELYRA S.1 microscope (Carl Zeiss microscopy) equipped with an Andor iXon 885 EMCCD camera, a 100X/1.40 NA oil-immersion objective and four laser beams (405, 488, 561, 642 nm). Serial z-stack sectioning was carried out at 101 nm intervals. Z-stacks were recorded with 3 phase-changes and 5 grating rotations for each section. The microscope was routinely calibrated with 100 nm fluorescent beads to calculate both lateral and axial limits of image resolution. Images were reconstituted with Zeiss Zen software. 3D rendering was produced by using Imaris 7.4.2 (Bitplane). Images were extracted from Imaris and then used to obtain the final images and movies used in the figures.

#### **4.4.11 Quantitative image analyses**

Inpp5e, Ift81 and Ift140 ciliary signals were quantified via subtraction of ciliary fluorescence signals from vicinity background signals; the boundary of ciliary axoneme was defined by Actub immunofluorescence, while  $\gamma$ tub immunofluorescence enables distinguishing between ciliary base and tip. For ciliary Ift81-YNL measurements, each cilium was divided into 10 equal compartments along cilia length. YNL fluorescence intensities along cilia length was obtained using a line scan spanning from base to tip of each primary cilium, and mean YNL fluorescence intensity in each compartment was obtained by averaging across entire sample. Total YNL fluorescence intensity in cilium was calculated by integrating fluorescence intensities across all 10 compartments. Mean YNL fluorescence intensity distribution along cilia length was obtained by expressing mean YNL fluorescence intensity in each compartment as a percentage of Total YNL fluorescence intensity in cilium.

For relative ciliary PH(PLC $\delta$ ) and small GTPase accumulation measurements, cilia length was measured by tracing a line along the ciliary marker signal, and PH(PLC $\delta$ )/small GTPase signal length was measured analogously and expressed as a ratio to cilia length. Probes were scored as cilia-localized if probe fluorescence signals were co-localized with 5HT<sub>6</sub> or Arl13b fluorescence signals in x-, y- and z- planes. Cell-associated ciliary vesicles were either defined as

Arl13b+Actub- particles (on fixed cells) or 5HT<sub>6</sub>/Arl13b-YFP-positive particles that were associated with cell surface. To determine mid-point of G<sub>0</sub>-G<sub>1</sub> transit, 10-hour time series of nuclear Venus-p27K<sup>-</sup> and mCherry-hCdt1(30/120) fluorescence signals were subtracted with background signals, divided to obtain Venus-p27K<sup>-</sup>/mCherry-hCdt1(30/120) signal ratio values, and further normalized with basal ratio values at T=0. 8xGBS-GFP Gli activity reporter measurements were based on quantification of average nuclear GFP signals in best-focused z-plane of each cell under specified conditions.

It is of note that we occasionally observed primary cilia of fibroblasts extending from the ventral cell surface and adhering to underlying substratum. Subsequent cellular movements could result in mechanical pulling and breaking of primary cilia (**Figure 4-4K**). Care was taken to exclude instances of passive cilia breaking throughout all experiments.

#### **4.4.12 Ciliary vesicle collection**

FBS used for vesicle collection was pre-depleted via overnight centrifugation at 100,000 xg to remove FBS-intrinsic tiny vesicles, exosomes and ectosomes. Wild-type or *Ift88*-KO mIMCD-3 cells were subjected to serum starvation by reducing FBS concentration to 0-0.1% for 12-24 hours after reaching confluence. Culture media were then replaced by fresh media containing 0-0.1% or 10% pre-depleted FBS. Conditioned culture media were collected 24 to 30 hours later. Small vesicles released from cultured cells into media were collected through a three-step centrifugation. Culture media were first centrifuged at 1,500 xg for 20 min to remove large cell debris. The supernatant of the first centrifuge was further centrifuged at 10,000 xg for 20 min. The supernatant of the second centrifuge was centrifuged at 100,000 xg for 3 hr with MLA-55 angle rotor (Beckman). Pellets were rinsed once with PBS, and then subjected to western blotting or proteomics.

#### **4.4.13 Western blotting**

Collected small vesicles were resolved in 1.5x SDS sample buffer. Cultured cells were also lysed with the same buffer. Extracted proteins were denatured at 95 °C for 5 min. Proteins were separated with SDS-PAGE, and transferred to PVDF membrane (Milipore). The membrane was blocked with 10% goat serum or 5% bovine serum albumin. The blocked membrane was incubated with primary antibodies in the blocking solution at 4 °C overnight. Primary antibodies used were as follows: anti-Ift88 (1:2000; ProteinTech, 13967-1-AP); anti-Kif3A (1:2000; BD Transduction, 611508); anti-Gli3 (1:200; R&D Systems, AF3690); anti-Gli2 (1:1000; Abcam, ab26056); anti-Sufu (1:2500; as reported in (Humke et al., 2010)); anti-Arl13b (1:1000; ProteinTech, 17711-1-AP); anti-actin (1:2000; Sigma, A2066); anti-Ift122 (1:2000; ProteinTech, 19304-1-AP); anti-Ift140 (1:2000; ProteinTech, 17460-1-AP); anti- $\gamma$ -tubulin (1:10000; Sigma, T9026). The primary antibodies were labeled with horseradish peroxidase-conjugated secondary antibodies (Jackson Immuno Lab). Signals were developed with enhanced chemiluminescent substrate (GE) and detected with a cooled CCD camera system, LAS-3000 mini (Fuji film). Band intensities were quantified with free software, ImageJ.

#### **4.4.14 LC-MS/MS of proteins in pelleted conditioned culture media**

Collected vesicles were lysed in 50 mM Tris, pH 8.0, containing 1.5% Triton X-100 with vigorous vortexing. Detergent and salt were removed with 2-D Clean-Up kit (GE Healthcare), and with cold acetone if further removal of detergent was required. Protein pellets were resolved in 50 mM  $\text{NH}_4\text{HCO}_3$  with vigorous vortexing. The proteins were subjected to reductive alkylation of sulfur group with iodoacetamide (ThermoFisher), and then digested with trypsin (ThermoFisher) at 37 °C overnight. Digested peptides were desalted by means of C-18 column (ThermoFisher) with 5% acetonitrile/0.5% trifluoroacetic acid used as wash buffer, and eluted with 70% acetonitrile. The acetonitrile was evaporated with a Speed-Vac concentrator (Tomy), and the eluted peptides were resolved in 0.1% formic acid.

The peptides were analyzed with a Q Exactive-Orbitrap mass spectrometer (ThermoFisher) connected to EASY-nLC liquid chromatography (ThermoFisher). Peptides were loaded into a micro capillary column (NTCC-360; Nikkyo Technos, Japan) of 75  $\mu\text{m}$  inner diameter, and separated with a linear gradient of acetonitrile from 0 to 35% in 0.1% formic acid at a flow rate of 325 nL/min. Separated peptides were ionized with Nanospray Flex Ion Source, NSI (ThermoFisher) at spray voltage of 2.0 kV. Full mass spectra were acquired with a resolution of 70,000, a maximum injection time of 60 msec, and a scan range between  $m/z$  350 to 1800, at positive ion mode. dd-MS<sup>2</sup> was acquired with a resolution of 17,500, a maximum injection time of 60 msec, and an isolation window of 2.0  $m/z$ . All processes were operated with software Xcalibur<sup>TM</sup> (ThermoFisher).

#### **4.4.15 Proteomic analyses**

Data acquired with LC-MS/MS were analyzed with Proteome Discoverer 1.4 software (ThermoFisher). All parameters for Spectrum Selector were set to default values. Identification of peptide/protein was carried out by means of MASCOT (MatrixScience) with Swiss-Prot used as database. Mass tolerances were 10 ppm for precursor mass and 0.02 Da for fragment mass. A miscleavage was allowed. Obtained peptide lists were validated by Percolator (Käll et al., 2007) based on q-values with a stringent threshold of target false discovery rate (FDR) of 1% using reverse decoy database (Elias and Gygi, 2007). The label-free semi-quantification was performed by using the precursor ions area detector (PIAD) node mounted in Proteome Discoverer 1.4.

Proteins that were detected at least two times in 9 independent experiments for serum-stimulated wild-type or *Ift88*-KO mIMCD-3 cells or 6 independent experiments for serum-starved wild-type mIMCD-3 cells were selected. The protein list and area values were exported as a table for further analyses in Microsoft Excel. Zero area values were replaced with one tenth of minimal area value of each sample for calculating fold changes. Ratio of mean area values were calculated for serum-stimulated wild type versus *Ift88*-KO cells (WT/*Ift88*-KO) and for serum-stimulated

versus serum-starved wild-type cells (10%/0.1%). Ratios were converted to logarithm to the base 2 ( $\log_2$ ), and Z-scores were calculated.

#### **4.4.16 Quantitative real-time PCR**

NIH/3T3 cells were seeded in OptiMEM (Thermo Fisher Scientific) for 24 hours to induce ciliogenesis at quiescent state. Cells were subsequently treated with DMEM containing 10% FBS for 0, 1, 2, 4, and 8 hr prior to sample collection. As a positive control, cells were also treated with 200 nM SAG (Cayman Chemicals) for 8hr. Cells were lysed with Buffer RLT, and RNA samples were isolated with the RNeasy Mini Kit with DNase I digestion (Qiagen). Samples were reverse transcribed using the iScript cDNA synthesis kit (BioRad). *Gli1* (F: 5'-GGATGAAGAAGCAGTTGGGA-3'; R: 5'-ATTGGATTGAACATGGCGTC-3') and *Ptch1* (F: 5'-CTCTGGAGCAGATTTCCAAGG-3'; R: 5'-TGCCGCAGTTCTTTTGAATG-3') primers were used to test for Hedgehog signaling activation. *Ubc* primers (F: 5'-TCCAGAAAGAGTCCACCCTG-3'; R: 5'-GACGTCCAAGGTGATGGTCT-3') were used to normalize *Gli1* and *Ptch1* transcript levels. Transcripts were quantified using SYBR-GreenER (Thermo Fisher Scientific) on a 7900HT Fast Real-Time PCR system (Thermo Fisher Scientific).

#### **4.4.17 Quantification and statistical analysis**

Statistical parameters including the definitions and exact values of n (number of cells and experiments), distributions and deviations are reported in figures and corresponding legends. Most data are represented as mean  $\pm$  SEM using two-tailed Student's T tests. Probability data in Figures 4-5 and 4-6 were analyzed using statistical risk ratio analyses. Mass spectrometry signal area ratios were presented with Z-scores in Table 4-2. Z-scores in Figure 4-12D were analyzed using Mann-Whitney U-test. Quantitative real-time PCR assays in Figure 4-15H were analyzed using one-way ANOVA. Statistical analyses were performed in Microsoft Excel, MedCalc or GraphPadPrism.



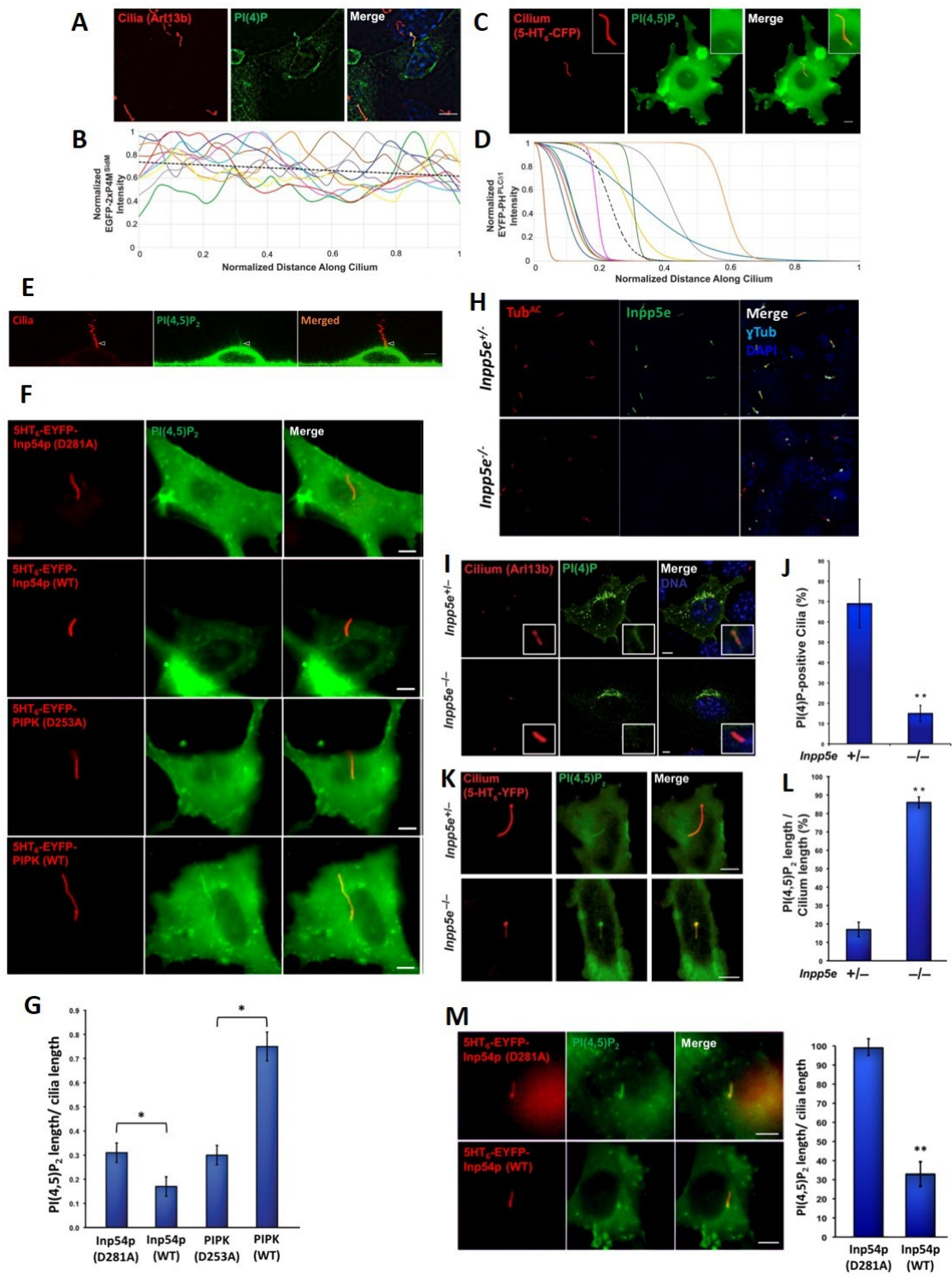


**Figure 4-1. PI(4)P and PI(4,5)P<sub>2</sub> are present in distinct ciliary compartments regulated by Inpp5e.**

- (A) IMCD3 cells transfected with EGFP-2xP4M<sup>SidM</sup>, a PI(4)P sensor, were stained with antibodies against the ciliary protein Arl13b (red) and EGFP (green). Nuclei were marked by DAPI (blue).
- (B) Normalized EGFP-2xP4M<sup>SidM</sup> intensity for ten IMCD3 cilia was plotted against normalized distance along the cilium. The black dotted line is the linear regression of all cilia.
- (C) Cilia of live NIH 3T3 cells were visualized by 5HT<sub>6</sub>-CFP fluorescence (false-colored red). PH<sup>PLCδ1</sup>-EYFP, a PI(4,5)P<sub>2</sub> sensor, accumulated in the proximal ciliary region (false-colored green).
- (D) Normalized EYFP-PH<sup>PLCδ1</sup> intensity for 11 NIH 3T3 cilia was plotted against normalized distance along the cilium, and the data were fitted to sigmoidal curves. The black dotted line is the average of all curves.
- (E) XZ optical section of live IMCD3 cells expressing 5HT<sub>6</sub>-CFP (red) and EYFP-PHPLCδ1 (green).
- (F) Live imaging of NIH-3T3 cells cotransfected with plasmids expressing the PI(4,5)P<sub>2</sub> sensor mCerulean3-PHPLCδ1 (green) and the indicated ciliary fusion proteins (red) containing the catalytically active and inactive forms of Inp54p, a yeast PI(4,5)P<sub>2</sub> 5-phosphatase, and PIPK, a mouse PI(4)P 5-kinase.
- (G) Quantitation of the extension of the mCerulean3-PHPLCδ1 fluorescence relative to ciliary length. The catalytically active phosphatase and kinase decreased and increased, respectively, the extent of ciliary mCerulean3-PHPLCδ1 fluorescence.
- (H) MEFs derived from littermate *Inpp5e*<sup>+/-</sup> and *Inpp5e*<sup>-/-</sup> embryos were stained for TubAc (red), Inpp5e (green), γ-Tub (cyan) and DNA (blue).

- (I) *Inpp5e*<sup>+/-</sup> and *Inpp5e*<sup>-/-</sup> MEFs expressing the PI(4)P sensor EGFP-2xP4M<sup>SidM</sup> were stained for Arl13b (red) and EGFP (green). Nuclei were marked by DAPI (blue).
- (J) Quantitation of the proportion of *Inpp5e*<sup>+/-</sup> and *Inpp5e*<sup>-/-</sup> MEF cilia that display ciliary localization of EGFP-2xP4M<sup>SidM</sup>.
- (K) Cilia of live *Inpp5e*<sup>+/-</sup> and *Inpp5e*<sup>-/-</sup> MEFs were visualized by 5HT<sub>6</sub>-YFP fluorescence (false-colored red). The PI(4,5)P<sub>2</sub> sensor PHPLCδ1-mCerulean3 (false-colored green) localized to a restricted proximal domain of cilia of *Inpp5e*<sup>+/-</sup> MEFs but localized throughout cilia of *Inpp5e*<sup>-/-</sup> MEFs.
- (L) Quantitation of the extent of the ciliary PHPLCδ1-mCerulean3 fluorescence (PI(4,5)P<sub>2</sub> length) relative to the extent of 5HT<sub>6</sub>-YFP fluorescence (cilium length) in *Inpp5e*<sup>+/-</sup> and *Inpp5e*<sup>-/-</sup> MEFs.
- (M) Live imaging of *Inpp5e*<sup>-/-</sup> MEFs co-transfected with plasmids expressing the PI(4,5)P<sub>2</sub> sensor mCerulean3-PHPLCδ1 (green) and the indicated ciliary fusion proteins (red) of catalytically inactive (D281A) or wild type Inp54p. Scale bars, 5μm. Quantitation of the extent of ciliary mCerulean3-PHPLCδ1 fluorescence (PI(4,5)P<sub>2</sub> length) relative to the cilium length in *Inpp5e*<sup>-/-</sup> MEFs.

In (G), (J), (L), (M), Data are shown as means ± SEM. \* < 0.05 \*\*p < 0.01 in unpaired t tests. Scale bars, 5 μm.

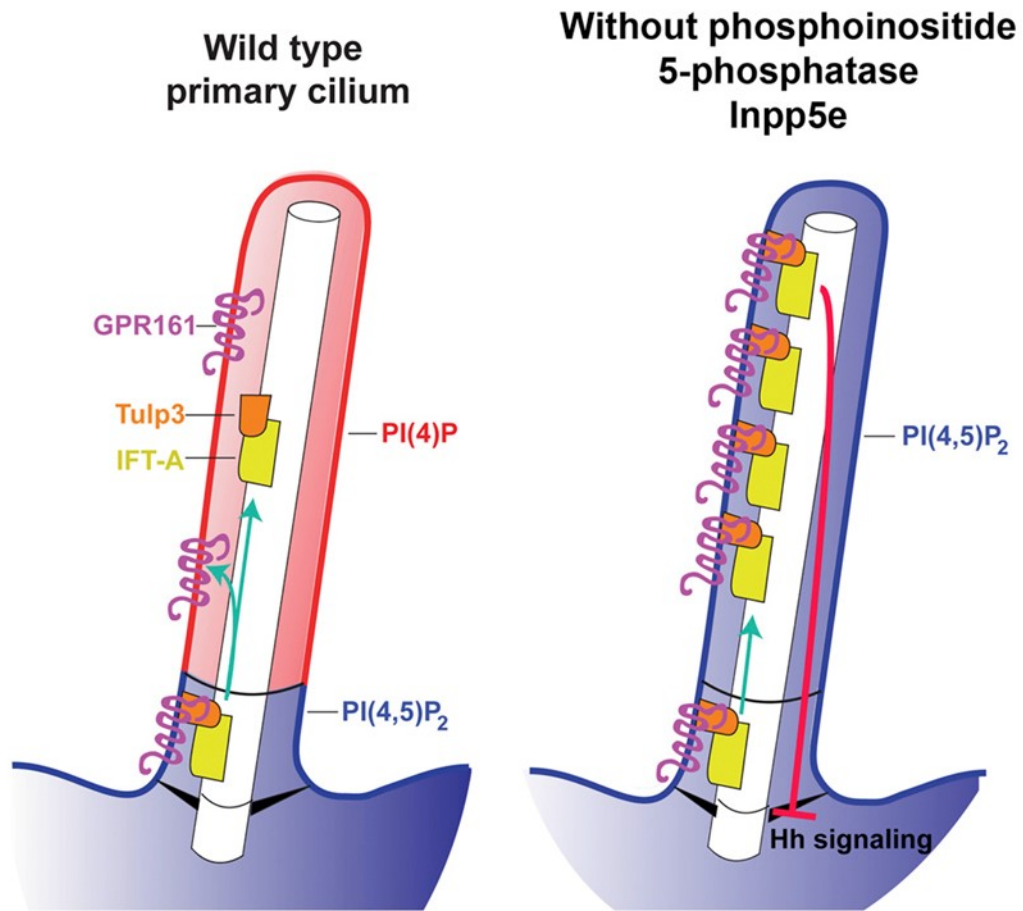


**Figure 4-2. Model of the role of ciliary phosphoinositides in Hh signaling.**

Inpp5e restricts PI(4,5)P<sub>2</sub> levels in the ciliary membrane. The ability of Tulp3 to interact with PI(4,5)P<sub>2</sub> but not PI(4)P is critical for limiting its accumulation and that of its interactors IFT-A and Gpr161 within the cilium. In the absence of Inpp5e, ciliary PI(4,5)P<sub>2</sub> levels increase, increasing the amount of negative regulators of Hh signaling, Tulp3, IFT-A, and Gpr161, within the cilium and restricting the ability of the cilium to transduce Hh signals.

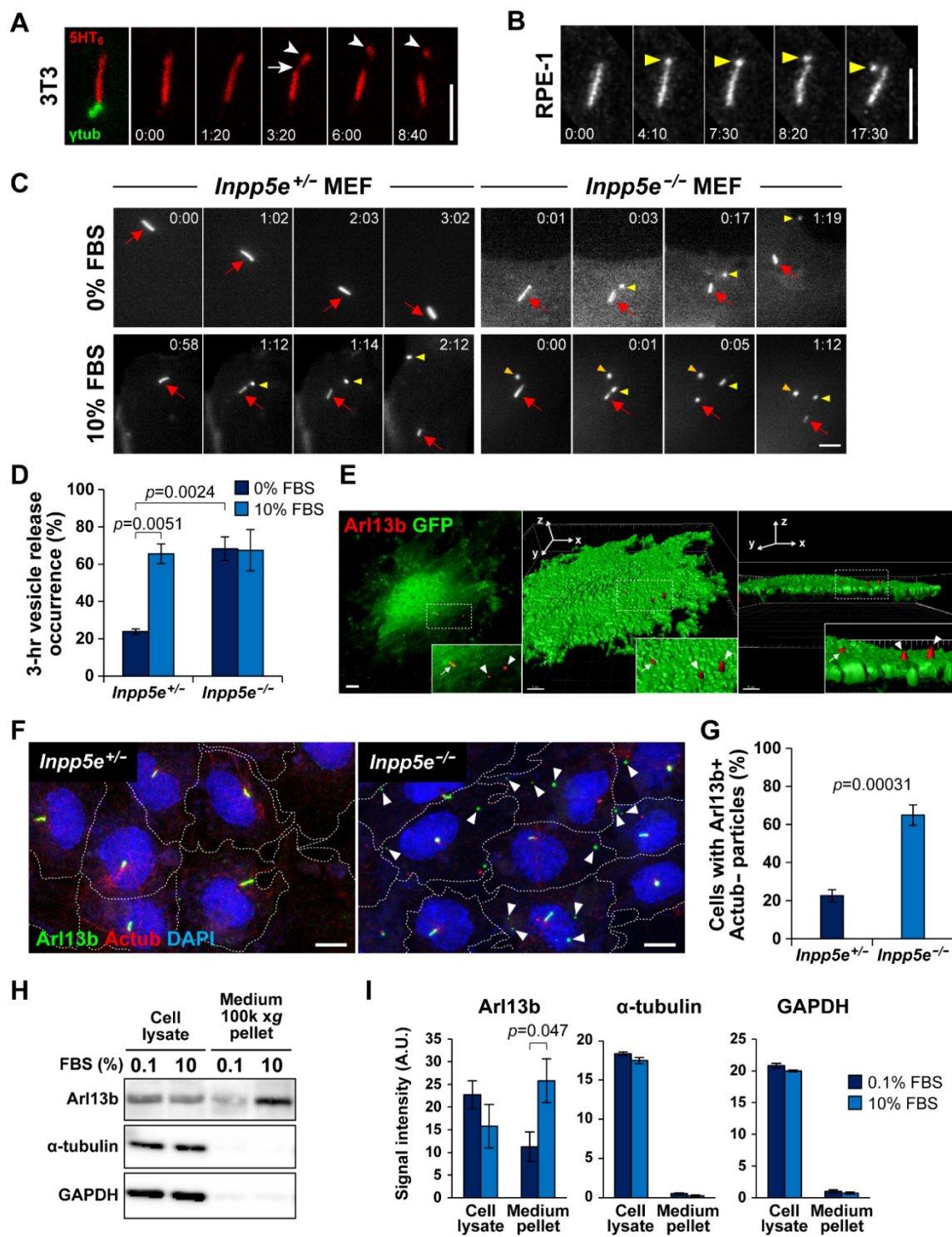


**Figure 4-3. Growth stimulation induces ciliary vesicle release regulated by *Inpp5e*.**

- (A) Time-lapse images of a NIH/3T3 primary cilium expressing 5HT<sub>6</sub>-mCherry and  $\gamma$ -tub-GFP at quiescent state. Arrow: ciliary membrane thinning prior to excision. Arrowheads: excised cilium tip.
- (B) Time-lapse images of an hTERT RPE-1 primary cilium expressing Arl13b-GFP at quiescent state. Note ciliary tip bulging prior to excision (yellow arrowheads).
- (C) Time-lapse images of *Inpp5e*<sup>+/+</sup> and *Inpp5e*<sup>-/-</sup> MEF primary cilia expressing 5HT<sub>6</sub>-YFP at quiescent or growth-stimulated states. Red arrows: cilia. Yellow arrows: excised cilia tips. Orange arrow: YFP+ particles present from beginning.
- (D) Scoring % of cells displaying ciliary vesicle release over 3 hours, as in (C). (n= 51, 49, 28, 34 cells from left to right; 3-5 experiments)
- (E) Maximum intensity projection of Arl13b immunofluorescence and GFP in *Inpp5e*<sup>-/-</sup> MEF. Middle and right panels are 3D reconstructions of confocal image on left panel. Insets are magnifications of dotted regions. Arrows: cilia. Arrowheads: Arl13b+ particles residing on cell surface.
- (F) Arl13b/Ac tub immunofluorescence and nuclear staining (DAPI) of quiescent *Inpp5e*<sup>+/+</sup> and *Inpp5e*<sup>-/-</sup> MEF. Arrowheads: Arl13b+Ac tub- particles.
- (G) Scoring % of cells with associated Arl13b+Actub- particles, as in (F). (n= 344, 376 cells from left to right; 3 experiments)
- (H) Representative Western blots in cell lysates and conditioned culture media pellets from mIMCD-3 cells treated with 0.1% or 10% FBS for 24 hours.
- (I) Quantification of band signal intensities in (H). (n = 4 experiments for Arl13b, n = 3 experiments for  $\alpha$ -tubulin and GAPDH)

Data are shown as mean  $\pm$  SEM; Student's T-tests were performed with  $p$  values indicated. Time in min:sec for (A) and (B), and hr:min for (C). Scale bars: 5 $\mu$ m in (A), (B), (C) and (E), and 10 $\mu$ m in (F).



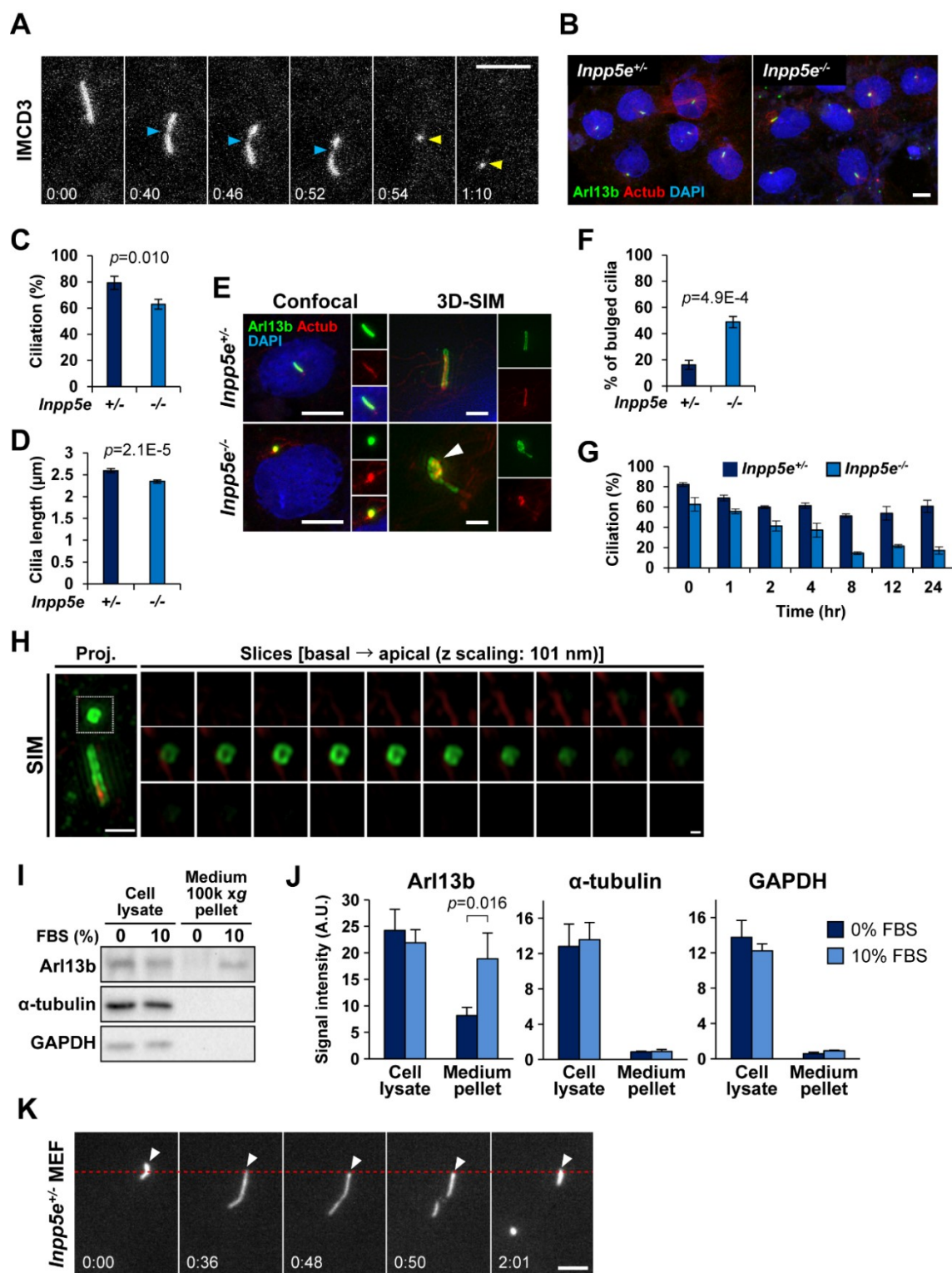




**Figure 4-4. Characterization of cilia decapitation and *Inpp5e*<sup>+/-</sup> and *Inpp5e*<sup>-/-</sup> MEF.**

- (A) Time-lapse images of a mIMCD-3 primary cilium expressing Arl13b-GFP at quiescent state (0% FBS). Blue arrows indicate membrane thinning prior to excision. Yellow arrowheads indicate excised cilium tip.
- (B) Representative confocal images of Arl13b and Ac-tub immunofluorescence in *Inpp5e*<sup>+/-</sup> MEF and *Inpp5e*<sup>-/-</sup> MEF at quiescent state. Nuclei labeled with DAPI.
- (C) Quantification of % ciliation in quiescent *Inpp5e*<sup>+/-</sup> and *Inpp5e*<sup>-/-</sup> MEF. A primary cilium is defined by positive labeling with Arl13b and Ac tub immunofluorescence. Data are represented as mean  $\pm$  SEM. A two-tailed Student's T-test was performed with *p* values indicated. (n=323, 374 cells; 3 experiments)
- (D) Quantification of Arl13b-labeled cilia lengths in quiescent *Inpp5e*<sup>+/-</sup> and *Inpp5e*<sup>-/-</sup> MEF. Data are represented as mean  $\pm$  SEM. A two-tailed Student's T-test was performed with *p* values indicated. (n=271, 353 cells; 3 experiments)
- (E) Confocal and SR-SIM images of Arl13b and Ac-tub immunofluorescence in *Inpp5e*<sup>+/-</sup> MEF and *Inpp5e*<sup>-/-</sup> MEF. Insets are magnified images of respective cilia. White arrowhead indicates bulged ciliary tip in *Inpp5e*<sup>-/-</sup> MEF.
- (F) Quantification of % cells displaying bulged ciliary tips as in (E). Data are represented as mean  $\pm$  SEM. A two-tailed Student's T-test was performed with *p* values indicated. (n=323, 374 cells; 3 experiments as in (B))
- (G) Quantification of % ciliation in *Inpp5e*<sup>+/-</sup> and *Inpp5e*<sup>-/-</sup> MEF at indicated time points post-stimulation with 10% FBS. Data are represented as mean  $\pm$  SEM. (n=271, 353 cells; 3 experiments)
- (H) Z-series of SR-SIM images of an Arl13b+ and Ac tub particle.

- (I) Representative Western blots of Arl13b,  $\alpha$ -tubulin and GAPDH proteins in collected cell lysates and pelleted conditioned culture media from mIMCD-3 cells treated with 0% or 10% FBS for 12 hours. Related to Figure 1H.
- (J) Quantification of respective band signal intensities in (I). Data were shown as mean  $\pm$  SEM. A two-tailed Student's T-test was performed with  $p$  values indicated. ( $n = 4$  experiments)
- (K) Representative time-lapse images of a ventral-positioned *Inpp5e*<sup>+/-</sup> MEF primary cilium passively breaking as a result of non-specific adhesion and immobilization to underlying substratum. Cell was expressed with 5HT<sub>6</sub>-YFP. Arrowheads indicate cilia tip. Red dotted line marks position of immobilization. See also Methods under "Quantitative image analyses".

Time in min:sec in (A), hr:min in (K). Scale bars indicate 5  $\mu$ m in (A) and (K), 10  $\mu$ m in (E) left panel, 1  $\mu$ m in (E) right panel, 1  $\mu$ m in (H) left panel and 0.2  $\mu$ m in (H) right panel.

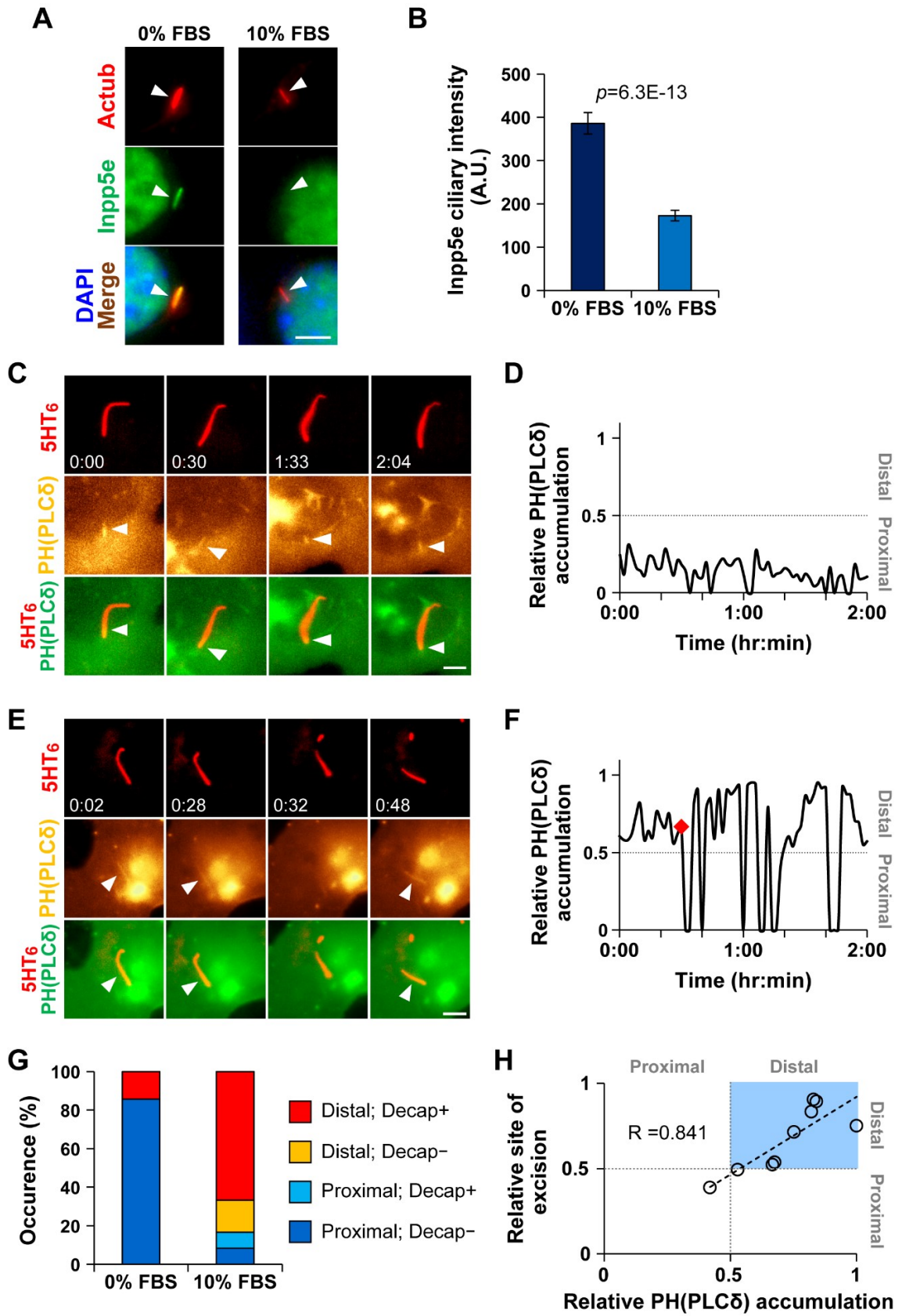


**Figure 4-5. Growth stimulation regulates ciliary Inpp5e and PI(4,5)P<sub>2</sub> localization.**

- (A) Ac tub/Inpp5e immunofluorescence and nuclear staining (DAPI) of *Inpp5e*<sup>+/-</sup> MEF treated with 0% FBS or 10% FBS for 4 hours. Images of each wavelength are scaled to same intensity range. Arrowheads mark cilia positions.
- (B) Inpp5e immunofluorescence signal intensity measurements in primary cilia, as in (A). Data shown as mean  $\pm$  SEM. Student's T-test was performed with *p* values indicated. (n= 131, 148 cells from left to right; 2 experiments)
- (C) Time-lapse images of *Inpp5e*<sup>+/-</sup> MEF primary cilium expressing 5HT<sub>6</sub>-mCerule3 and YFP-PH(PLC $\delta$ ) (a PI(4,5)P<sub>2</sub> sensor) at quiescent state. Arrows marks PH(PLC $\delta$ ) at proximal cilia.
- (D) Time-lapse measurements of PH(PLC $\delta$ ) proximal-distal accumulation in cilium in (C), given as relative ratio of cilium length.
- (E) Time-lapse images of *Inpp5e*<sup>+/-</sup> MEF primary cilium expressing 5HT<sub>6</sub>-mCerule3 and YFP-PH(PLC $\delta$ ) at 4-6 hours of 10% FBS stimulation. Arrows marks ciliary PH(PLC $\delta$ ).
- (F) Time-lapse measurements of PH(PLC $\delta$ ) accumulation in cilium in (E), given as relative ratio of cilium length. Red diamond marks cilia decapitation time point.
- (G) Classifying ciliary PH(PLC $\delta$ ) accumulation with cilia decapitation. "Distal" or "proximal" indicates PH(PLC $\delta$ ) accumulating to distal or proximal half of ciliary length. "Decap+" or "Decap-" indicates presence or absence of cilia decapitation over 2-hour imaging periods. (n= 7,12 cells from left to right; 2-3 experiments)
- (H) Correlation plot of ciliary PH(PLC $\delta$ ) accumulation with site of excision, each given as a relative ratio of ciliary length. In each case, the maximal ciliary PH(PLC $\delta$ ) accumulation value within ten minutes prior to excision is shown. Light blue box highlights distal location of ciliary PH(PLC $\delta$ ) accumulation and site of cilia excision. Linear regression is drawn in dashed line, with Pearson correlation coefficient R value indicated. (n=9 cells from 10% FBS data in (G))

Time in hr:min for (C) and (E). Scale bars: 5 $\mu$ m.

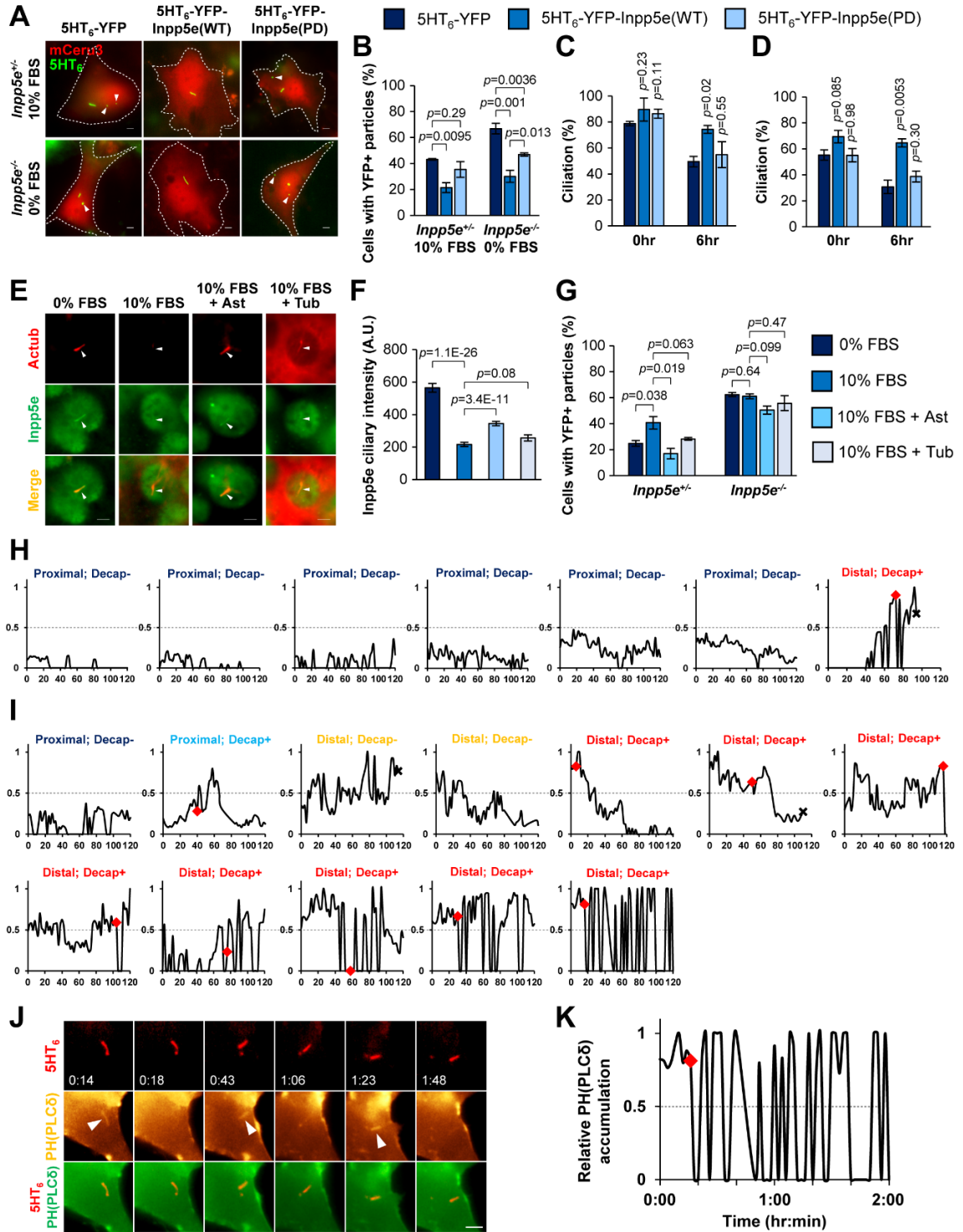


**Figure 4-6. AurA-dependent ciliary Inpp5e depletion re-organizes ciliary PI(4,5)P<sub>2</sub>.**

- (A) Live fluorescence images of *Inpp5e*<sup>+/-</sup> MEF or *Inpp5e*<sup>-/-</sup> MEF expressing 5HT<sub>6</sub>-YFP, 5HT<sub>6</sub>-YFP-Inpp5e(WT) or 5HT<sub>6</sub>-YFP-Inpp5e(CD) with cytosolic mCerule3 respectively after 4 hours of 10% FBS stimulation or at quiescent state (0% FBS). White dashed lines delineate cells. White arrowheads indicate cell-associated YFP+ particles that were likely vesicles released from primary cilia.
- (B) Quantification of % cells with associated extracellular YFP+ particles under indicated conditions, as in (A). Color coding as in panel above. Data are represented as mean ± SEM. Two-tailed Student's T-tests were performed with *p* values indicated. (n= 111, 73, 92, 94, 88, 74 cells for respective data from left to right; 4 experiments)
- (C) Quantification of % ciliation in *Inpp5e*<sup>+/-</sup> MEF expressing 5HT<sub>6</sub>-YFP, 5HT<sub>6</sub>-YFP-Inpp5e(WT) or 5HT<sub>6</sub>-YFP-Inpp5e(CD) with cytosolic mCerule3 at 0 hour and 6 hours of 10% FBS stimulation. Color coding as in panel above. Data are represented as mean ± SEM. Two-tailed Student's T-tests were performed with respect to each 5HT<sub>6</sub>-YFP condition, *p* values indicated. (n=88, 54, 49, 66, 35, 44 cells for respective data from left to right; 2 experiments)
- (D) Quantification of % ciliation in *Inpp5e*<sup>-/-</sup> MEF expressing 5HT<sub>6</sub>-YFP (control), 5HT<sub>6</sub>-YFP-Inpp5e(WT) or 5HT<sub>6</sub>-YFP-Inpp5e(CD) with cytosolic mCerule3 at 0 hour and 6 hours of 10% FBS stimulation. Color coding as in panel above. Data are represented as mean ± SEM. Two-tailed Student's T-tests were performed with respect to each 5HT<sub>6</sub>-YFP condition, *p* values indicated. (n=94, 49, 57, 100, 55, 70 cells for respective data from left to right; 3 experiments)
- (E) Ac tub and Inpp5e immunofluorescence of *Inpp5e*<sup>+/-</sup> MEF treated with 0% FBS, 10% FBS, 10% FBS +200nM Alisertib (Ast), or 10% FBS + 2μM Tubacin (Tub) for 4 hours. Images within Ac tub and Inpp5e image panels are scaled to same intensity range, while Ac tub signals are adjusted in Merge to visualize axoneme. Arrowheads indicate cilia.

- (F) Signal intensity measurements of Inpp5e immunofluorescence in primary cilia (cilia - vicinity background) under indicated conditions, as in (E). Color coding as in panel on the right. Data are represented as mean  $\pm$  SEM. A two-tailed Student's T-test was performed with *p* values indicated. (n= 190, 169, 173, 106 cells for respective data from left to right; 3 experiments)
- (G) Quantification of % cells with associated extracellular YFP+ particles in *Inpp5e*<sup>+/-</sup> MEF and *Inpp5e*<sup>-/-</sup> MEF expressing 5HT<sub>6</sub>-YFP with cytosolic mCerule3 after 4 hours in 0% FBS, 10% FBS, 10% FBS + 200nM Ast, or 10% FBS + 2 $\mu$ M Tub. Color coding as in panel on the right. Data are represented as mean  $\pm$  SEM. A two-tailed Student's T-test was performed with *p* values indicated. (n= 124, 131, 112, 121, 48, 54, 47, 37 cells for respective data from left to right; 2-3 experiments)
- (H-I) Time-lapse measurements of ciliary PH(PLC $\delta$ ) accumulation in *Inpp5e*<sup>+/-</sup> MEF at (H) quiescent state (as shown in Figure 2D) or (I) growth-stimulated state (as shown in Figure 2F). Horizontal axes indicate time(min); vertical axes indicate ciliary PH(PLC $\delta$ ) accumulation expressed as a ratio of cilium length. Color coding as used in Figure 2G. Dotted line divide proximal half (0-0.5) and distal half (0.5-1.0) of cilium. "X" indicates end of imaging period. Data for (I) were between 2hrs and 4hrs, or 4hrs and 6hrs post-stimulation with 10% FBS.
- (I) An example of growth-stimulated primary cilia exhibiting PI(4,5)P<sub>2</sub> oscillation post-decapitation. White arrowheads indicate ciliary PH(PLC $\delta$ ).
- (J) Time-lapse measurements of PH(PLC $\delta$ ) accumulation in cilium in (C), expressed as relative ratio of cilium length. Red diamond marks time point of decapitation.

Time in hr:min. Scale bars indicate 5 $\mu$ m.



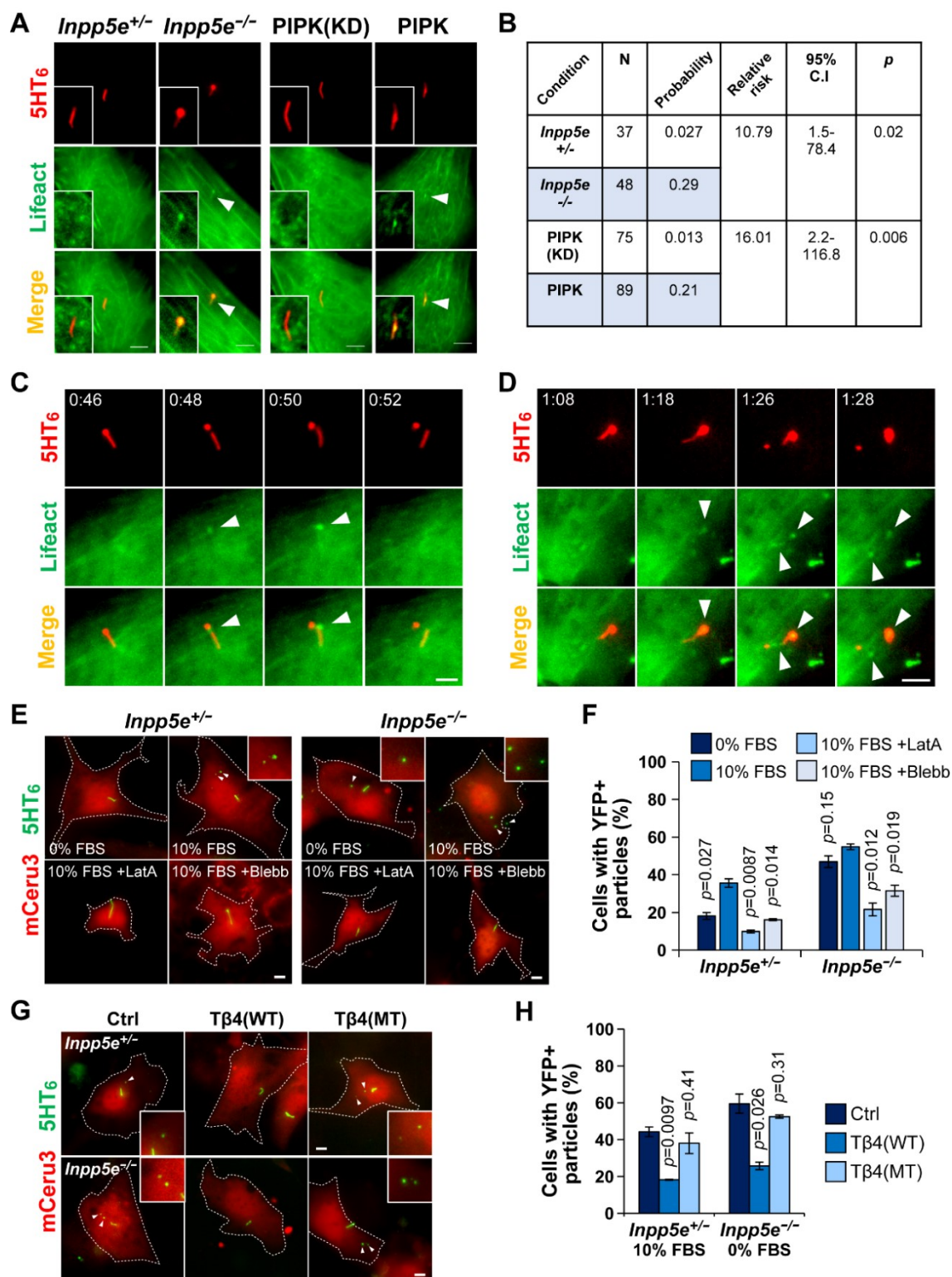


**Figure 4-7. Ciliary PI(4,5)P<sub>2</sub> induces intraciliary F-actin assembly which executes cilia decapitation.**

- (A) Live fluorescence images of (two leftmost columns) *Inpp5e*<sup>+/-</sup> and *Inpp5e*<sup>-/-</sup> MEF primary cilia expressing 5HT<sub>6</sub>-YFP and mCeru3-Lifeact, and (two rightmost columns) NIH/3T3 primary cilia expressing 5HT<sub>6</sub>-YFP-PIPK or 5HT<sub>6</sub>-YFP-PIPK(KD) and mCeru3-Lifeact. Insets are magnifications of respective cilia. Arrowheads mark ciliary Lifeact signals.
- (B) Relative risk ratio analyses on the effect of ciliary PI(4,5)P<sub>2</sub> in influencing intraciliary F-actin incidence, as in (A).
- (C) Time-lapse images of a primary cilium from *Inpp5e*<sup>+/-</sup> MEF expressing 5HT<sub>6</sub>-YFP and mCeru3-Lifeact at 4-6 hours of 10% FBS stimulation. Arrowheads mark F-actin at site of cilia excision.
- (D) Time-lapse images of primary cilium from *Inpp5e*<sup>-/-</sup> MEF expressing 5HT<sub>6</sub>-YFP and mCeru3-Lifeact at 0-2 hours of 10% FBS stimulation. Arrowheads mark F-actin at site of cilia excision. Note that F-actin first appeared in bulged cilia tip before expanding to proximal cilia region. F-actin was also detected in excised cilia tip.
- (E) Live fluorescence images of *Inpp5e*<sup>+/-</sup> and *Inpp5e*<sup>-/-</sup> MEF expressing 5HT<sub>6</sub>-YFP with mCeru3 after 3 hours in 0% FBS, 10% FBS, 10% FBS + 200nM latrunculin A (LatA), or 10% FBS + 50μM blebbistatin (Blebb). Arrowheads indicate cell-associated YFP<sup>+</sup> particles that were likely vesicles released from primary cilia, and insets are respective magnified images.
- (F) Quantification of % cells with associated extracellular YFP<sup>+</sup> particles, as in (E). (n=99, 82, 70, 62, 75, 69, 73, 67 cells from left to right; 2 experiments)
- (G) Live fluorescence images of *Inpp5e*<sup>+/-</sup> MEF and *Inpp5e*<sup>-/-</sup> MEF expressing 5HT<sub>6</sub>-YFP (control), 5HT<sub>6</sub>-YFP-Tβ4(WT) or 5HT<sub>6</sub>-YFP-Tβ4(MT) with mCeru3 respectively after 3 hours of 10% FBS stimulation or at quiescence (0% FBS). Arrowheads indicate cell-associated YFP<sup>+</sup> particles, and insets are respective magnified images.

(H) Quantification of % cells with associated extracellular YFP<sup>+</sup> particles, as in (G). (n=83, 88, 96, 69, 95, 76 cells from left to right; 2 experiments)

Data shown as mean  $\pm$  SEM. Student's T-tests were performed with respect to (E) each 10% FBS condition and (F) each control condition, *p* values indicated. Time in hr:min for (A) and (B). Scale bars: 5 $\mu$ m.

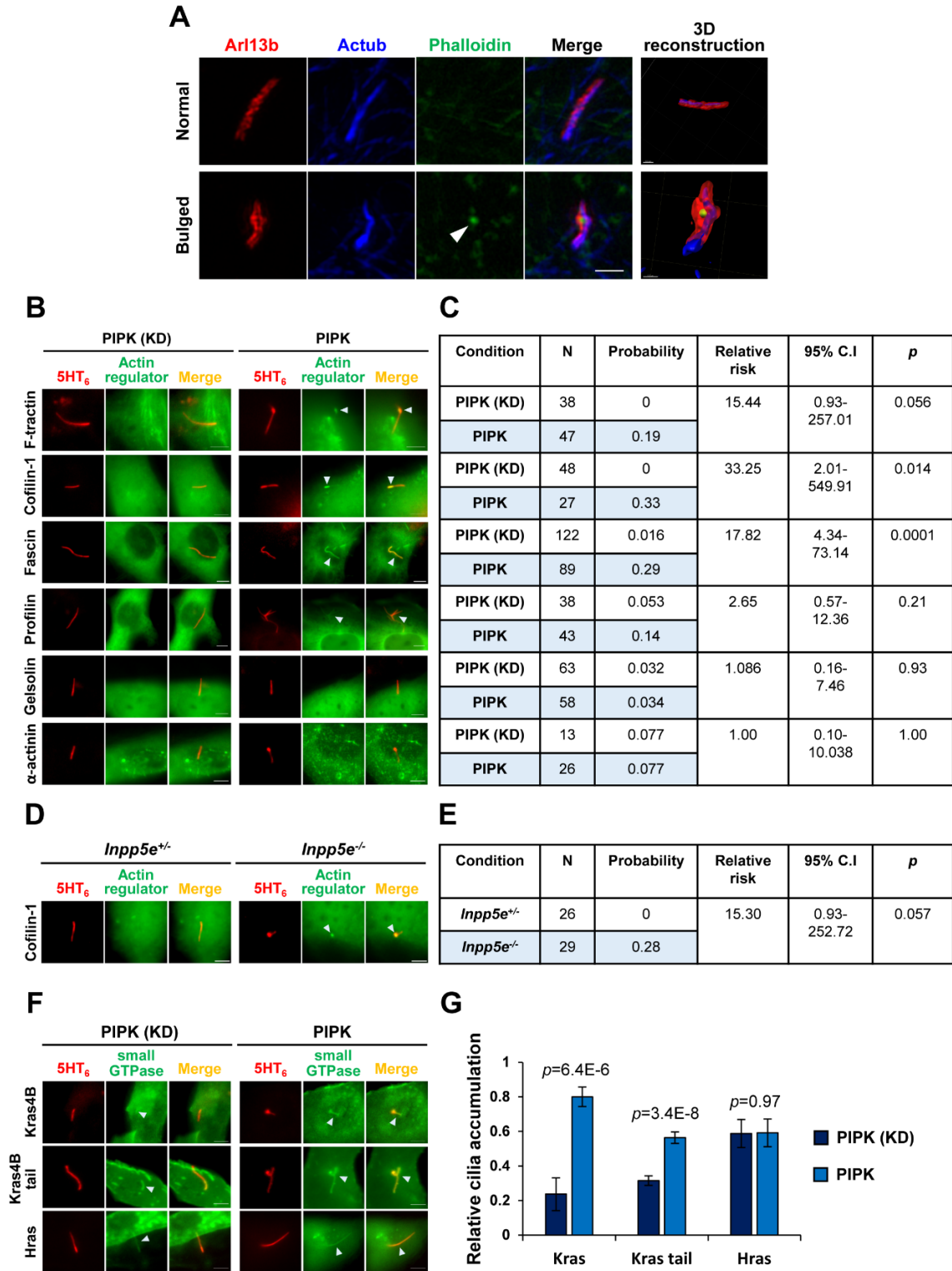


**Figure 4-8. PI(4,5)P<sub>2</sub> regulates ciliary localization of F-actin, actin regulatory proteins and small GTPases.**

- (A) SR-SIM images of Arl13b, Ac tub and phalloidin immunofluorescence in normal and bulged cilia of *Inpp5e*<sup>-/-</sup> MEF. Rightmost panel are IMARIS 3D reconstructions of “Merge” images. Arrowhead indicates ciliary phalloidin signals.
- (B) Live fluorescence images of NIH/3T3 expressing 5HT<sub>6</sub>-mCerule3-PIPK or 5HT<sub>6</sub>-mCerule3-PIPK(KD) and respective YFP-tagged F-actin sensor (F-tractin) or actin regulatory proteins. White arrowheads indicate ciliary localization of respective proteins. Cofilin-1 was generally observed to accumulate at ciliary tip, while fascin was detected along ciliary length.
- (C) Relative risk ratio analyses on the effect of differential ciliary PI(4,5)P<sub>2</sub> in influencing intraciliary F-actin or actin regulatory protein incidence, for corresponding horizontal image rows in (A).
- (D) Live fluorescence images of *Inpp5e*<sup>+/-</sup> and *Inpp5e*<sup>-/-</sup> MEF expressing 5HT<sub>6</sub>-mCerule3 and cofilin1-YFP. White arrowhead indicates tip accumulation of cofilin-1.
- (E) Relative risk ratio analyses on the effect of differential ciliary PI(4,5)P<sub>2</sub> in influencing intraciliary cofilin-1 incidence, as in (C).
- (F) Live fluorescence images of NIH/3T3 expressing 5HT<sub>6</sub>-mCerule3-PIPK or 5HT<sub>6</sub>-mCerule3-PIPK(KD) and respective YFP-tagged (top) phosphoinositide-binding Kras small GTPase, (middle) Kras tail anchor harboring phosphoinositide-binding module, or (bottom) non-phosphoinositide-binding Hras small GTPase. White arrowheads indicate ciliary localization. While Kras was restricted to the proximal cilia in 5HT<sub>6</sub>-FP-PIPK(KD)-expressing cells, 5HT<sub>6</sub>-FP-PIPK expression was sufficient to accumulate Kras into distal cilia. In contrast, Hras accumulated to distal cilia regardless of ciliary PI(4,5)P<sub>2</sub>.
- (G) Quantification of small GTPase or tail anchor accumulation in cilia, expressed as a relative ratio of cilium length. Data are represented as mean ± SEM. Two-tailed Student’s T-tests

were performed with respect to each PIPK (KD) condition, *p* values indicated. (n=12, 20, 71, 84, 25, 24 cells; 2-3 experiments)

Scale bars indicate 1μm in (A) and 5μm in (B), (D) and (G).

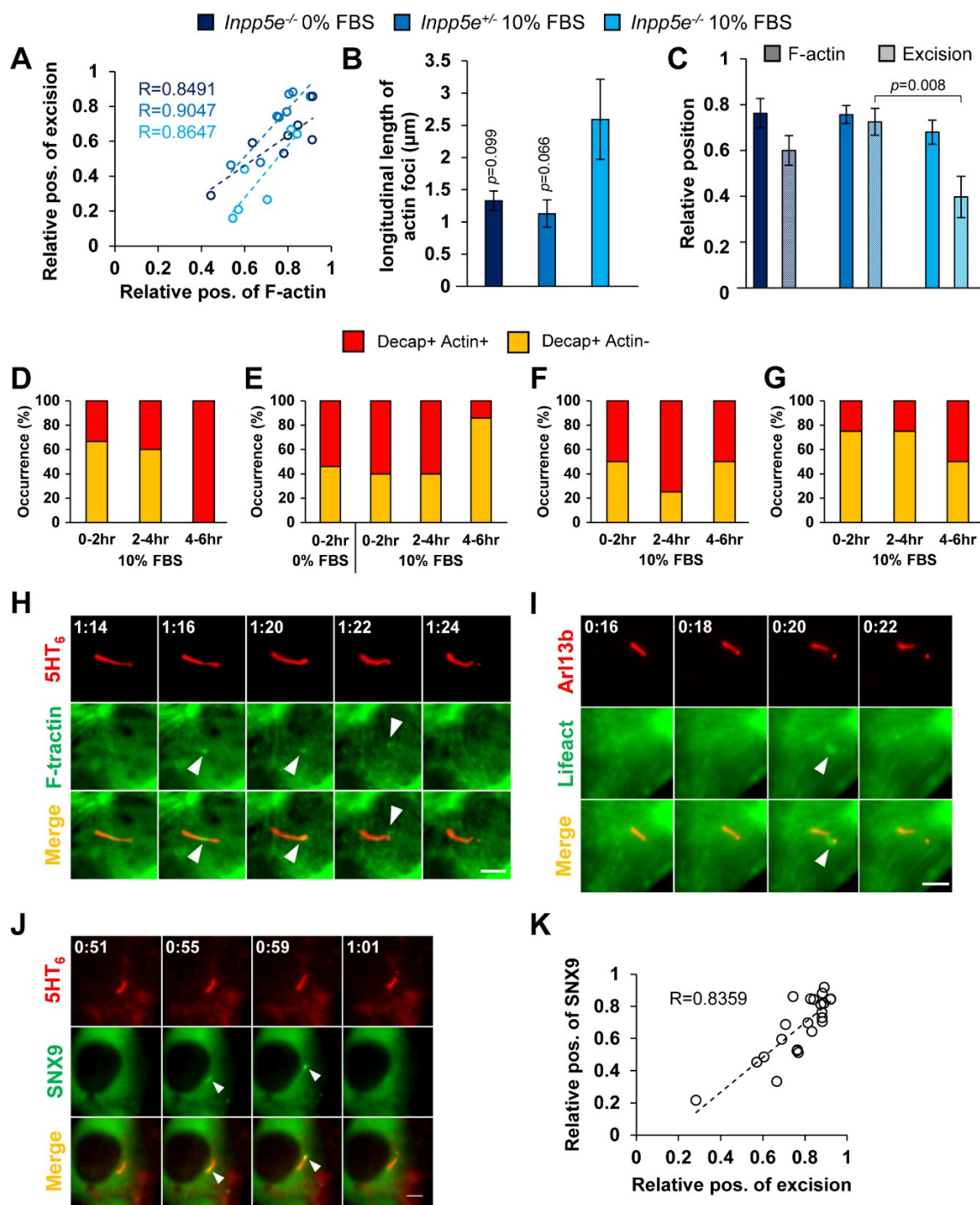


**Figure 4-9. F-actin and SNX9 localize in primary cilia prior to decapitation.**

- (A) Correlation plot of intraciliary F-actin position with excision position, each expressed as relative ratio of cilia length. Color coding as in panel above. Position of F-actin was measured at estimated centroid position of F-actin foci prior to excision. In each case, linear regression is drawn in dashed line, with Pearson correlation coefficient  $R$  value indicated. (n=7, 8, 6 cells from left to right; 2-3 experiments from (D) and (E))
- (B) Quantification of actin foci longitudinal length just prior to excision. Color coding as in panel above. Data shown as mean  $\pm$  SEM. Student's T-tests were performed with respect to *Inpp5e*<sup>-/-</sup> 10% FBS condition,  $p$  values indicated. (n= 7, 8, 6 cells from left to right; 2-3 experiments from (D) and (E))
- (C) Quantification of relative position of cilia excision and F-actin. Color coding as in panel above. Data shown as mean  $\pm$  SEM. Student's T-test was performed with  $p$  value indicated. (n= 7, 8, 6 cells from left to right; 2-3 experiments from (D) and (E))
- (D) Percentage of cilia decapitation events with or without co-observed intraciliary F-actin in *Inpp5e*<sup>+/-</sup> MEF expressing 5HT<sub>6</sub>-YFP and mCerule3-Lifeact between 0-2, 2-4 and 4-6 hours of 10% FBS stimulation, related to Figure 3C. Of note, the transient nature of intraciliary F-actin could render inefficient capturing by the two-minute experimental imaging intervals, and a high F-actin marker intensity in the cell body could also limit visualization of specific signals in primary cilia; also applies to (E-G). Color coding as in panel above. (n=6, 5, 4 cells; 2-3 experiments (D) and (E))
- (E) Percentage of cilia decapitation events with or without co-observed intraciliary F-actin in *Inpp5e*<sup>-/-</sup> MEF 5HT<sub>6</sub>-YFP and mCerule3-Lifeact between 0 and 2 hours in 0% FBS, or between 0-2, 2-4 and 4-6 hours of 10% FBS stimulation, related to Figure 3D. Color coding as in panel above. (n=13, 5, 5, 7 cells; 2-3 experiments)



- (F) Percentage of cilia decapitation events with or without co-observed intraciliary F-actin in *Inpp5e*<sup>+/-</sup> MEF expressing 5HT<sub>6</sub>-mCerule3 and alternative F-actin sensor, F-tractin-Citrine, at respective time periods of 10% FBS stimulation, see (H) below. Color coding as in panel above. (n=2, 4, 2 cells; 2 experiments)
- (G) Percentage of cilia decapitation events with or without co-observed intraciliary F-actin in *Inpp5e*<sup>+/-</sup> MEF expressing Lifeact-mCerule3 and alternative ciliary membrane marker, Arl13b-YFP, at respective time periods of 10% FBS stimulation, see (I) below. Color coding as in panel above. (n=4, 4, 4 cells; 2 experiments)
- (H) Time-lapse images of *Inpp5e*<sup>+/-</sup> MEF expressing 5HT<sub>6</sub>-mCerule3 and F-tractin-citrine between 0hrs and 2hrs post-stimulation with 10% FBS, as in (F). White arrowheads indicate F-actin assembly at site of cilia excision.
- (I) Time-lapse images of *Inpp5e*<sup>+/-</sup> MEF expressing Arl13b-YFP and Lifeact-mCerule3 between 4hrs and 6hrs post-stimulation with 10% FBS, as in (G). White arrowheads indicate F-actin assembly at site of cilia excision.
- (J) Time-lapse images of *Inpp5e*<sup>+/-</sup> MEF expressing 5HT<sub>6</sub>-mCerule3 and YFP-SNX9 between 4hrs and 6hrs post-stimulation with 10% FBS. Arrowheads indicate SNX9 propagation from proximal cilia to distal site of cilia excision.
- (K) Correlation plot of SNX9 intraciliary position with position of excision, each expressed as relative ratio of cilia length. Position of SNX9 was measured at estimated centroid position of SNX9 foci just prior to excision. Linear regression is drawn in dashed line with Pearson correlation coefficient R value indicated. (n=23 cells; 2 experiments)

Time in hr:min. Scale bars indicate 5µm.

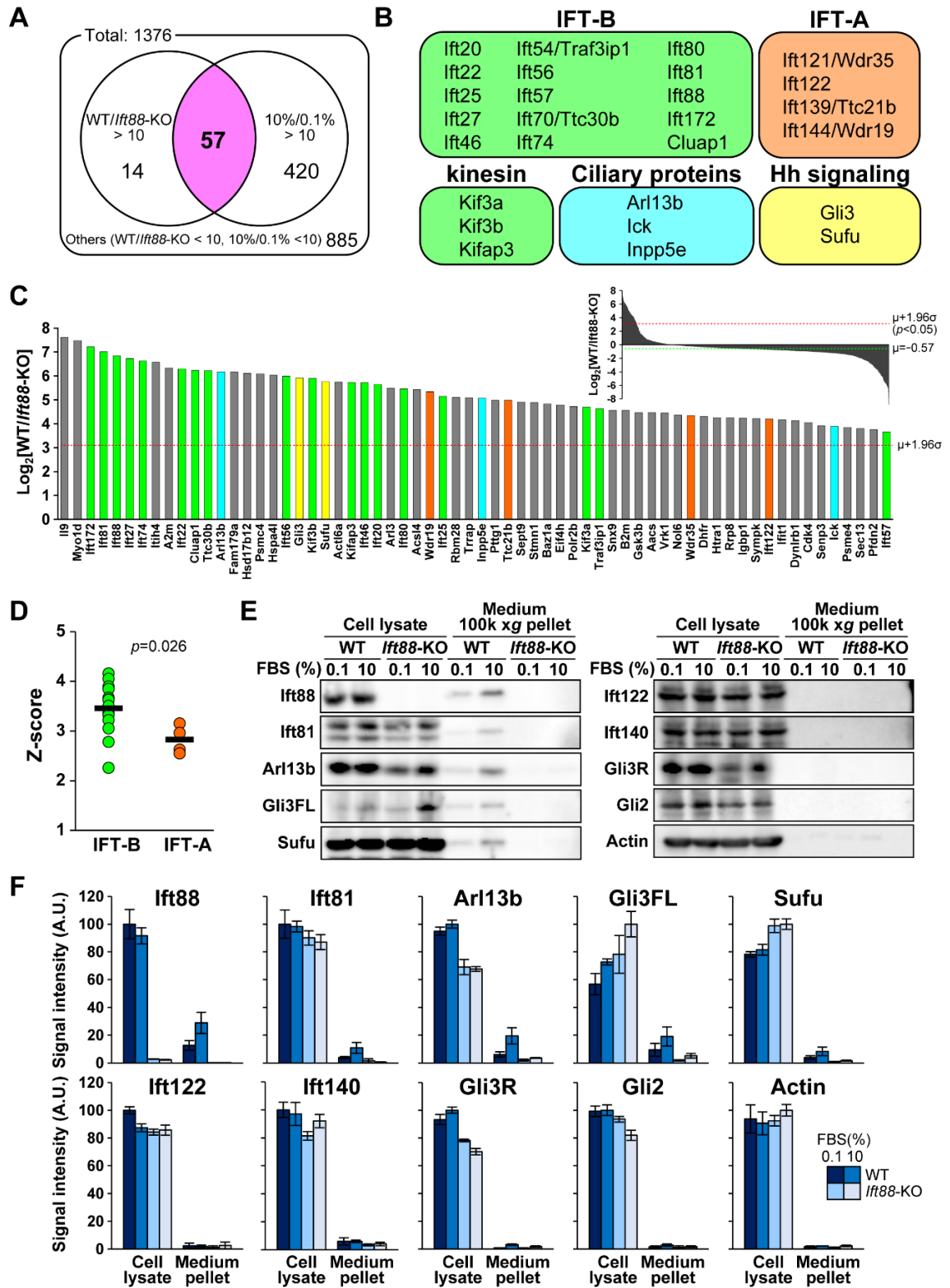


**Figure 4-10. Global proteomic profiling of conditioned culture media reveals growth-stimulated extracellular release of IFT-B dependent on primary cilia.**

- (A) Venn diagram classification of proteins detected in conditioned culture media under indicated conditions, with a threshold of false discovery rate=0.01. “10%/0.1% >10”: 477 proteins with mass spectrometry signal areas  $\geq 10$  fold higher in 10% FBS condition than in 0.1% FBS condition, in WT mIMCD-3 (growth stimulation-dependent). “WT/*Ift88*KO >10”: 71 proteins with mass spectrometry signal areas  $\geq 10$  fold higher in WT mIMCD-3 than *Ift88*-KO mIMCD-3, in 10% FBS condition (cilia-dependent). There is a 57-protein (purple) overlap, i.e. both cilia- and growth stimulation- dependent.
- (B) Classification of ciliary proteins amongst the 57 proteins highlighted in (A).
- (C) Comparative analyses of proteins extracellularly released in cilia-dependent manner (WT/*Ift88*KO). Mass spectrometry signal area ratios for respective proteins are represented as logarithm to the base 2 ( $\log_2$ ), and ranked in descending order of Z-scores. Only top 1.2% of proteins with Z-scores higher than 2.25 are shown. The mean ( $\mu$ )  $\log_2$  ratios of area values is -0.57, and standard deviation ( $\sigma$ ) is 1.87. Color coding as in (B).
- (D) Z-score comparison between IFT-B and IFT-A components identified from proteomic analysis, as in (C). *Ift88* is excluded from IFT-B group, since a high WT/*Ift88*KO ratio would occur with *Ift88*-KO. Bars indicate mean of Z-scores. A Mann-Whitney U-test was performed with *p* values indicated.
- (E) Representative Western blot analyses in total cell lysates and conditioned culture media pellets.
- (F) Quantification of respective band signal intensities in (E). Data shown as mean  $\pm$  SEM. (n=3 experiments)

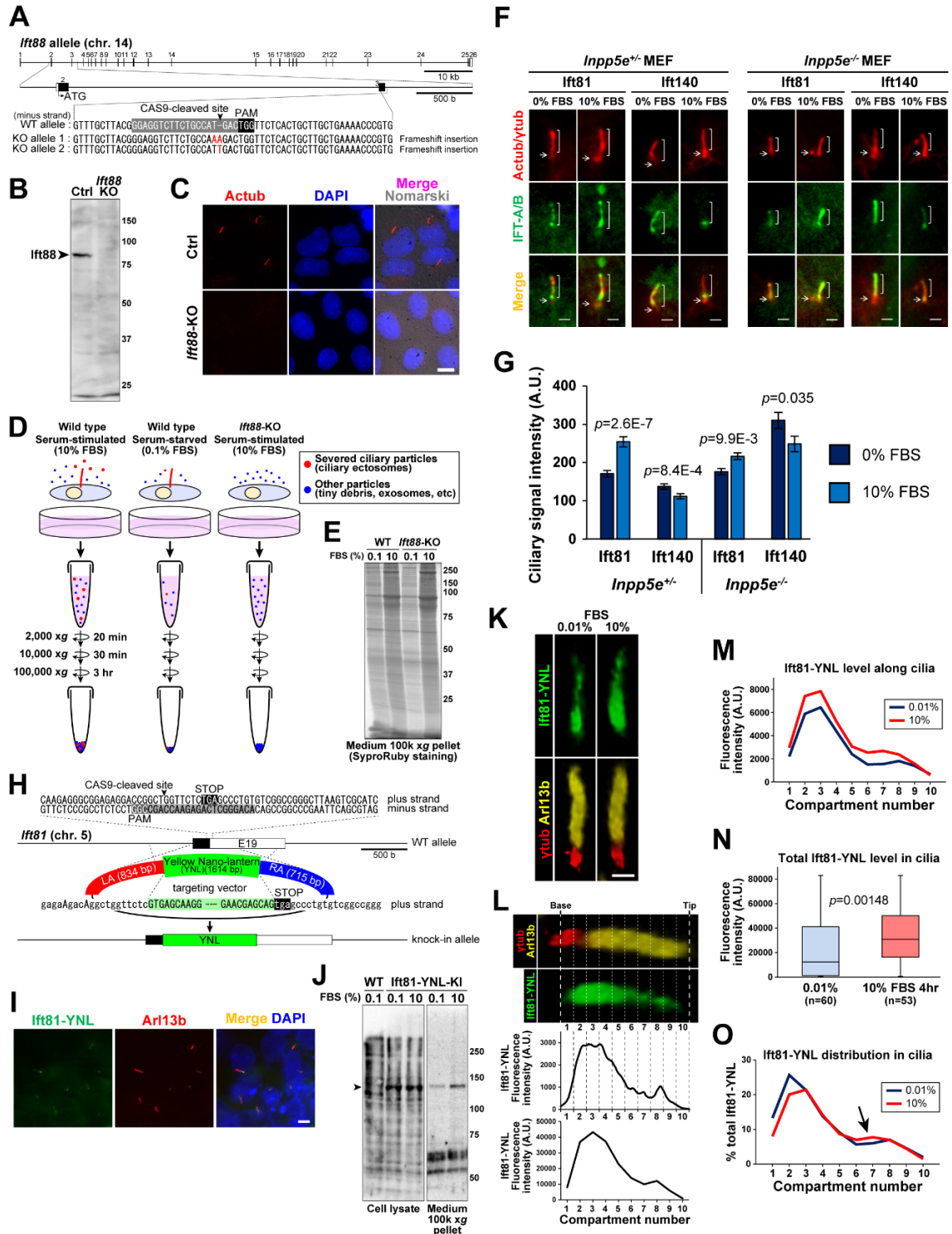


**Figure 4-11. Experimental scheme for ciliary vesicle proteomic profiling and analyses of ciliary IFT distribution.**

- (A) Generation of *Ift88*KO mIMCD-3 cell line using CRISPR/CAS9-based genome editing technique. The target sequence of guide-RNA (gRNA) used was placed on the minus strand of the genome corresponding to the exon 3 of *Ift88*. Generated *Ift88*KO mIMCD-3 cell line had bi-allelic frameshift insertion at the CAS9-cleaved site.
- (B) Loss of *Ift88* expression was verified using Western blot analysis with an anti-*Ift88* antibody.
- (C) Ac tub immunofluorescence revealed that *Ift88*KO mIMCD-3 cells lack primary cilia.
- (D) Schematic illustrating the collection and processing of conditioned culture media under indicated conditions. Culture media were first pelleted at low centrifugal force to remove large cell debris, followed by higher centrifugal forces to concentrate smaller ciliary vesicles and exosomes.
- (E) Representative SDS-PAGE of 100k xg pelleted conditioned media under conditions illustrated in (D), as visualized by SyproRuby staining.
- (F) Actub/ $\gamma$ tub and *Ift81*/*Ift140* immunofluorescence of *Inpp5e*<sup>+/+</sup> and *Inpp5e*<sup>-/-</sup> MEF treated with 0% FBS or 10% FBS for 4 hours. Images within Ac tub/ $\gamma$ tub and *Ift81*/*Ift140* image panels in each column group are scaled to same intensity range. Brackets indicate axoneme, while arrows mark centrioles.
- (G) Signal intensity measurements of *Ift81* or *Ift140* immunofluorescence in primary cilia (cilia - vicinity background) under indicated conditions, as in (F). Data are represented as mean  $\pm$  SEM. Two-tailed Student's T-tests were performed with respect to each 0% FBS condition, *p* values indicated. (n= 114, 118, 90, 88, 14, 113, 87, 79 cells for respective data from left to right; 3 experiments)
- (H) Schematic illustration of yellow Nano-lantern (YNL) knock-in into 3'-end of *Ift81* to generate *Ift81*:YNL knock-in mIMCD-3 cell line.

- (I) Ift81-YNL co-localizes with Arl13b immunofluorescence in Ift81:YNL knock-in mIMCD-3 cell line.
- (J) Western blot detection of YNL-tagged endogenous Ift81 (arrowhead) using anti-GFP polyclonal antibody in total cell lysates or particle-enriched 100k-g culture media pellets of WT or Ift81:YNL knock-in mIMCD-3 after a 24-hour stimulation with either 0.1% FBS or 10% FBS.
- (K) Fluorescence images of Ift81-YNL with Arl13b and  $\gamma$ tub immunofluorescence upon 4-hour 0.01% FBS or 10% FBS stimulation of Ift81:YNL knock-in mIMCD-3.
- (L) Schematic illustration of cilia length compartmentalization used for ciliary Ift81 analyses in (M)-(O). For each primary cilium, YNL fluorescence intensities along cilia length was first obtained using a line scan spanning from base to tip of cilium (middle), and total fluorescence intensity within each compartment was derived via signal integration (bottom).
- (M) Quantification of mean Ift81-YNL fluorescence intensities along cilia length of primary cilia subjected to 4-hour stimulation with 0.01% FBS or 10% FBS. (n = 60 for 0.01% FBS; n = 53 for 10% FBS)
- (N) Quantification of total Ift81-YNL fluorescence signals of primary cilia subjected to 4-hour stimulation of either 0.01% FBS or 10% FBS. Total Ift81-YNL level in each cilium was calculated via integration of fluorescence signals across all compartments described in (L). Data are shown as median  $\pm$  quartile (box) and 90 percentile (bars). Mann-Whitney U-test was performed with *p* values indicated. (n = 60 for 0.01% FBS; n = 53 for 10% FBS)
- (O) Quantification of mean Ift81-YNL fluorescence signal distribution along cilia length, expressed as a percentage of total Ift81-YNL fluorescence signals as in (N).
- Scale bars indicate 10 $\mu$ m in (C), 2  $\mu$ m in (F), 5 $\mu$ m in (I) and 1  $\mu$ m in (K).

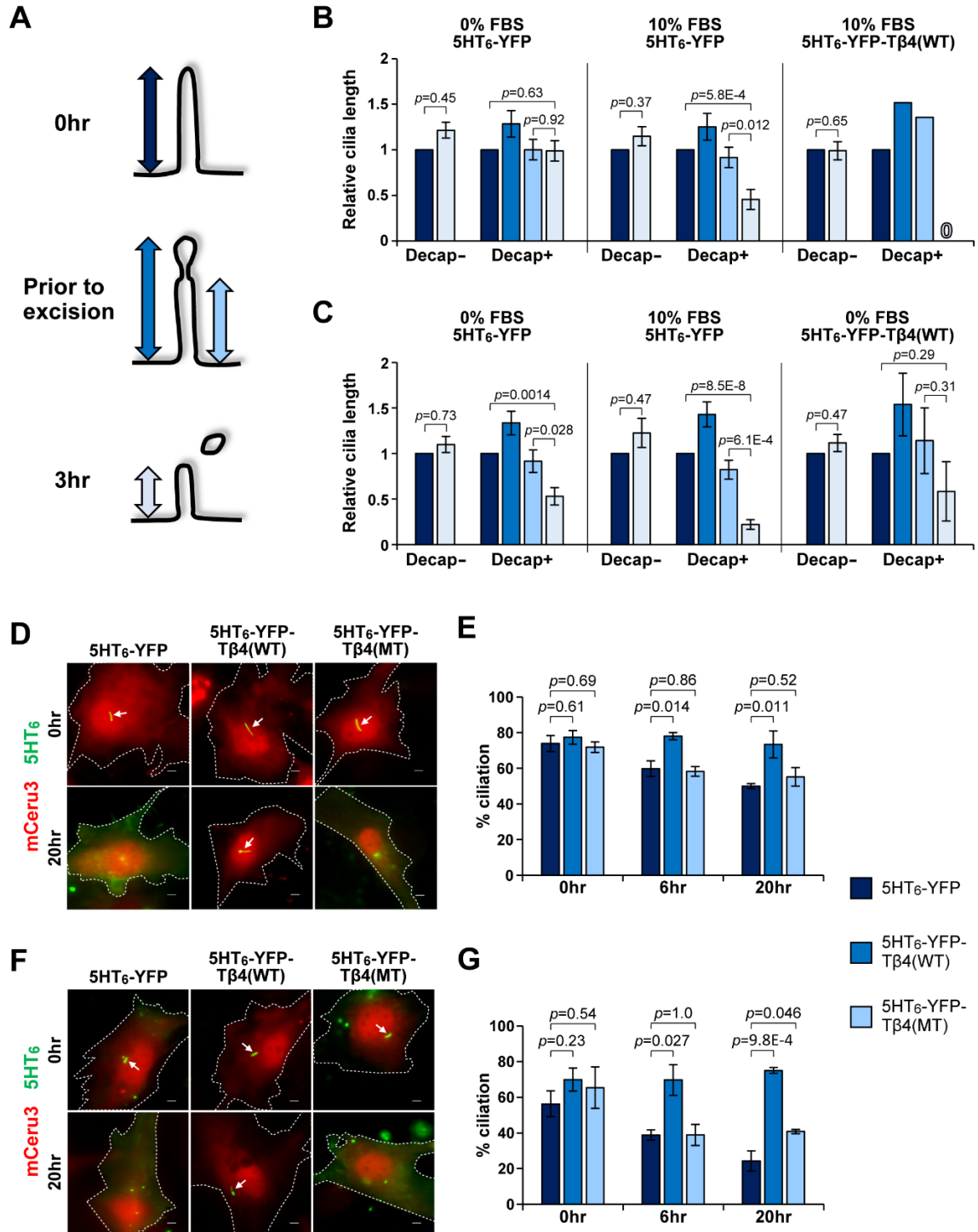


**Figure 4-12. Inhibition of cilia decapitation suppresses growth-stimulated cilia disassembly.**

(A) Schematic illustrating the time points when respective cilia lengths, indicated by double-headed arrows, were measured over a 3-hour live imaging period. Color coding for arrows applies to (B) and (C).

(B) Quantification of *Inpp5e*<sup>+/-</sup> MEF cilia lengths over 3-hour imaging period. Cilia are classified according to occurrence of cilia decapitation, and cilia lengths are given as a ratio to cilia length at T=0. Only a single cell was available for analysis under the category of “Decap+; 10% FBS Tβ4(WT)” due to high efficacy of 5HT<sub>6</sub>-YFP-Tβ4(WT) in inhibiting cilia decapitation. “0” indicates complete disassembly. Data in left and middle panels were derived from data in Figure 1D. (n=26,11,19,22,9,1 cells; 1-5 experiments)

(C) Quantification of *Inpp5e*<sup>-/-</sup> MEF cilia lengths over 3-hour imaging period, with similar data representation as in (B). Data in left and middle panels were derived from data in Figure 1D. (n=8,16,8,20,11,3 cells; 2-5 experiments)

(D) Live fluorescence images of *Inpp5e*<sup>+/-</sup> MEF under indicated conditions at 0 and 20 hours of 10% FBS stimulation. Arrows mark cilia.

(E) Quantification of % cells possessing primary cilia, as in (D). (n=167, 182, 162, 157, 153, 164, 176, 131, 139 cells from left to right; 3 experiments)

(F) Live fluorescence images of *Inpp5e*<sup>-/-</sup> MEF under indicated conditions at 0 and 20 hours of 10% FBS stimulation. Arrows mark cilia.

(G) Quantification of % cells possessing primary cilia, as in (F). (n=165, 155, 112, 156, 107, 123, 14, 136, 144 cells from left to right; 3 experiments)

Data shown as mean ± SEM; Student's T-tests were performed with *p* values indicated. In (B-C), Student's T-tests were performed on absolute cilia lengths. Scale bars: 5μm.



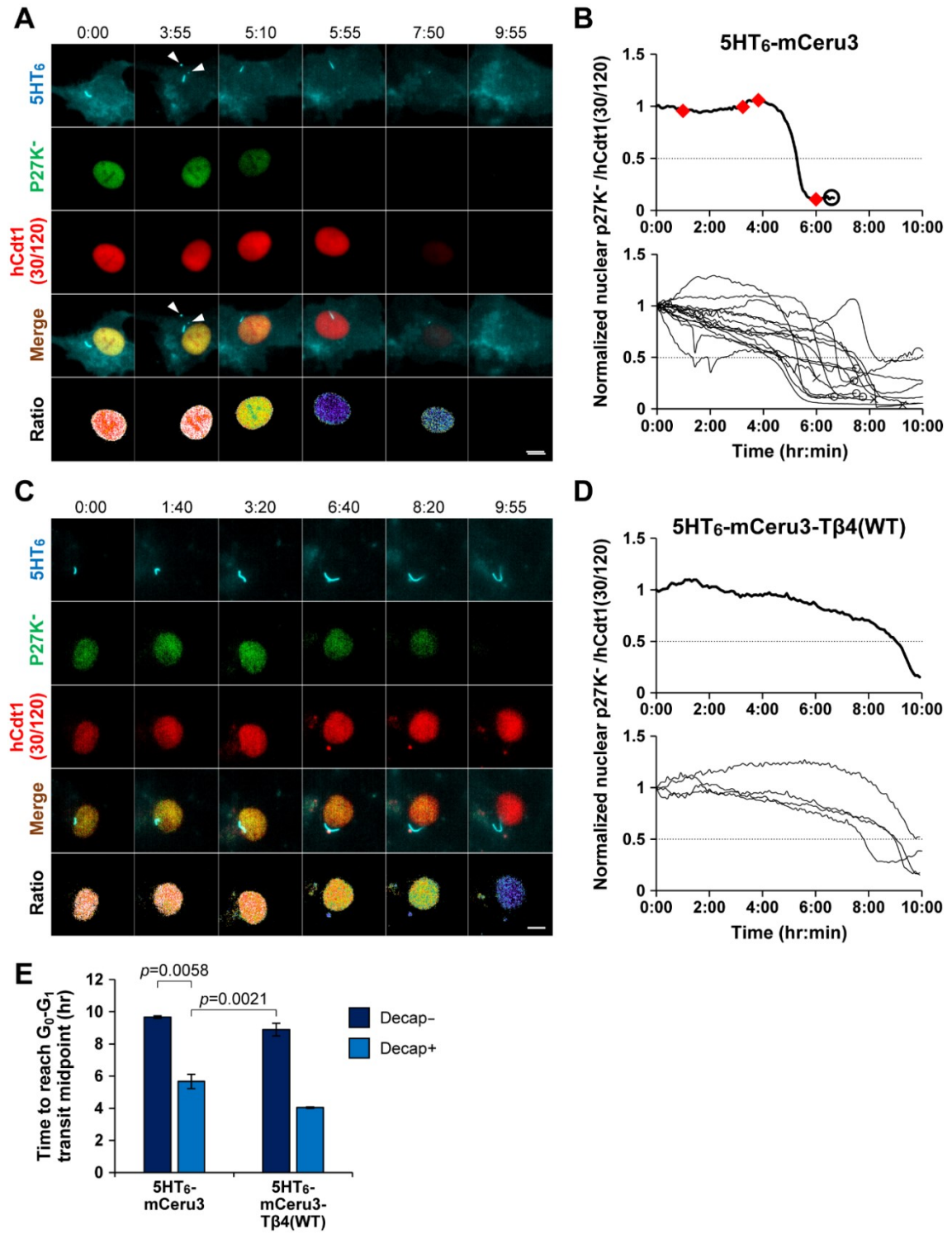


**Figure 4-13. Cilia decapitation occurs in G<sub>0</sub> and regulates G<sub>1</sub> phase entry.**

- (A) Representative time-lapse images of prompt G<sub>1</sub> entry that occurs with cilia decapitation in *Inpp5e*<sup>+/-</sup> MEF expressing 5HT<sub>6</sub>-mCeru3. Venus-p27K<sup>-</sup> was abruptly degraded at approximately 5 hours post-FBS stimulation, and rapid mCherry-hCdt1(30/120) depletion ensued by approximately 8 hours post-growth stimulation, indicating transit into G<sub>1</sub> and S phase respectively. Images of each panel are scaled to same intensity range.
- (B) Quantification of basal-normalized nuclear Venus-p27K<sup>-</sup>/mCherry-hCdt1 ratio (pseudo-colored in (A)) over 10 hours. Upper panel: plot for cell in (A). Red diamonds indicate cilia decapitation time points. Open circle marks beginning of mCherry-hCdt1(30/120) degradation. Lower panel: plot for all 15 cells that were determined for quiescence exit within the 10-hour period (i.e. these cells demonstrated a sharp decrease in Venus-p27K<sup>-</sup> at some point). Cilia decapitation events not denoted here; refer to Figure S6A for individual plots. Open circle marks beginning of mCherry-hCdt1(30/120) degradation. Crosses mark end of imaging period.
- (C) Representative time-lapse images of prolonged G<sub>1</sub> entry that occurs with suppressed cilia decapitation in *Inpp5e*<sup>+/-</sup> MEF expressing 5HT<sub>6</sub>-mceru3-Tβ4(WT). Note gradual Venus-p27K<sup>-</sup> degradation which indicates delayed G<sub>1</sub> entry. Images of each panel are scaled to same intensity range.
- (D) Quantification of basal-normalized nuclear Venus-p27K<sup>-</sup>/mCherry-hCdt1 ratio (pseudo-colored in (C)) over 10 hours. Upper panel: plot for cell in (C). No cilia decapitation was observed over the 10-hour imaging period. Lower panel: plot for all 4 cells that were determined to exit quiescence; refer to Figure S6D for individual plots.
- (E) Quantification of time duration to reach G<sub>0</sub>-G<sub>1</sub> transit mid-point, derived from time points when basal-normalized p27K<sup>-</sup>/hCdt1=0.5. Only cells that reached ratio value ≤0.5 by 10

hours were considered here. Data shown as mean  $\pm$  SEM. Student's T-tests were performed with  $p$  values indicated. (n=2, 15, 4, 2 cells; 3-7 experiments)

Time in hr:min. Scale bars: 10 $\mu$ m.

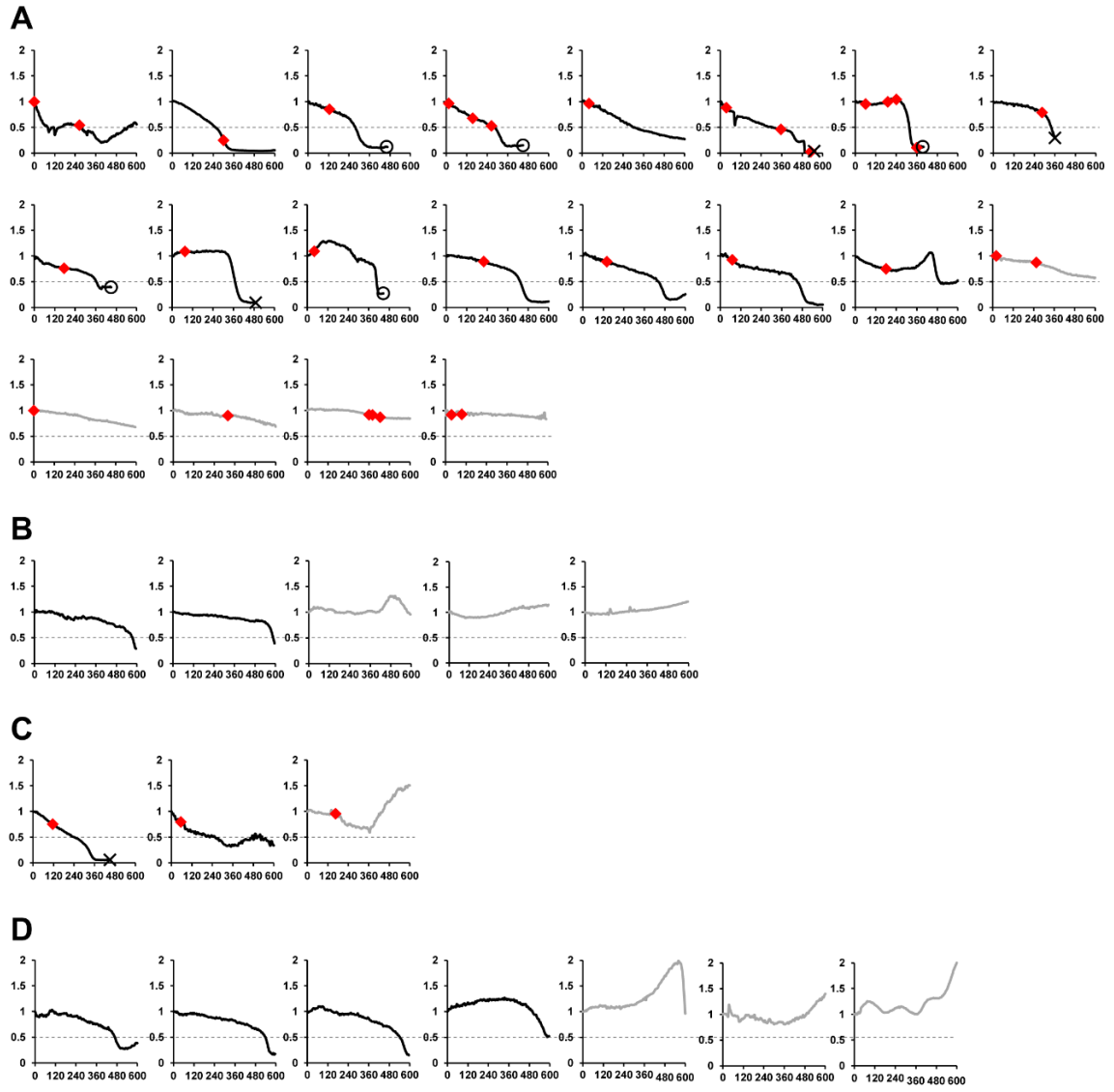


**Figure 4-14. Time-lapse measurements of nuclear Venus-p27K/mCherry-hCdt1(30/120) signal intensity ratios under growth stimulation.**

Time-lapse measurements of nuclear Venus-p27K/mCherry-hCdt1(30/120) signal intensity ratios in:

- (A) Decap<sup>+</sup> *Inpp5e*<sup>+/-</sup> MEF expressing 5HT<sub>6</sub>-mCeru3;
- (B) Decap<sup>-</sup> *Inpp5e*<sup>+/-</sup> MEF expressing 5HT<sub>6</sub>-mCeru3;
- (C) Decap<sup>+</sup> *Inpp5e*<sup>+/-</sup> MEF expressing 5HT<sub>6</sub>-mCeru3-Tβ4(WT);

(D) Decap- *Inpp5e*<sup>+/-</sup> MEF expressing 5HT<sub>6</sub>-mCeru3-Tβ4(WT).

Horizontal axes indicate time (min); vertical axes indicate basal normalized ratios of Venus-p27K<sup>-</sup>/mCherry-hCdt1. Black dashed lines indicate arbitrary G<sub>0</sub>-G<sub>1</sub> transit mid-point. Red diamonds mark time points of cilia decapitation events. Open circles indicate beginning of mCherry-hCdt1(30/120) signal decrease (signifying start of S-phase transit). Crosses indicate end of imaging period. Responses plotted in grey were cells which maintained ratio values >0.5 throughout the 10-hour imaging period (these cells did not demonstrate a sharp decrease in Venus-p27K<sup>-</sup> i.e. not determined for quiescence exit), and were excluded from time measurements in Figure 4-13E.

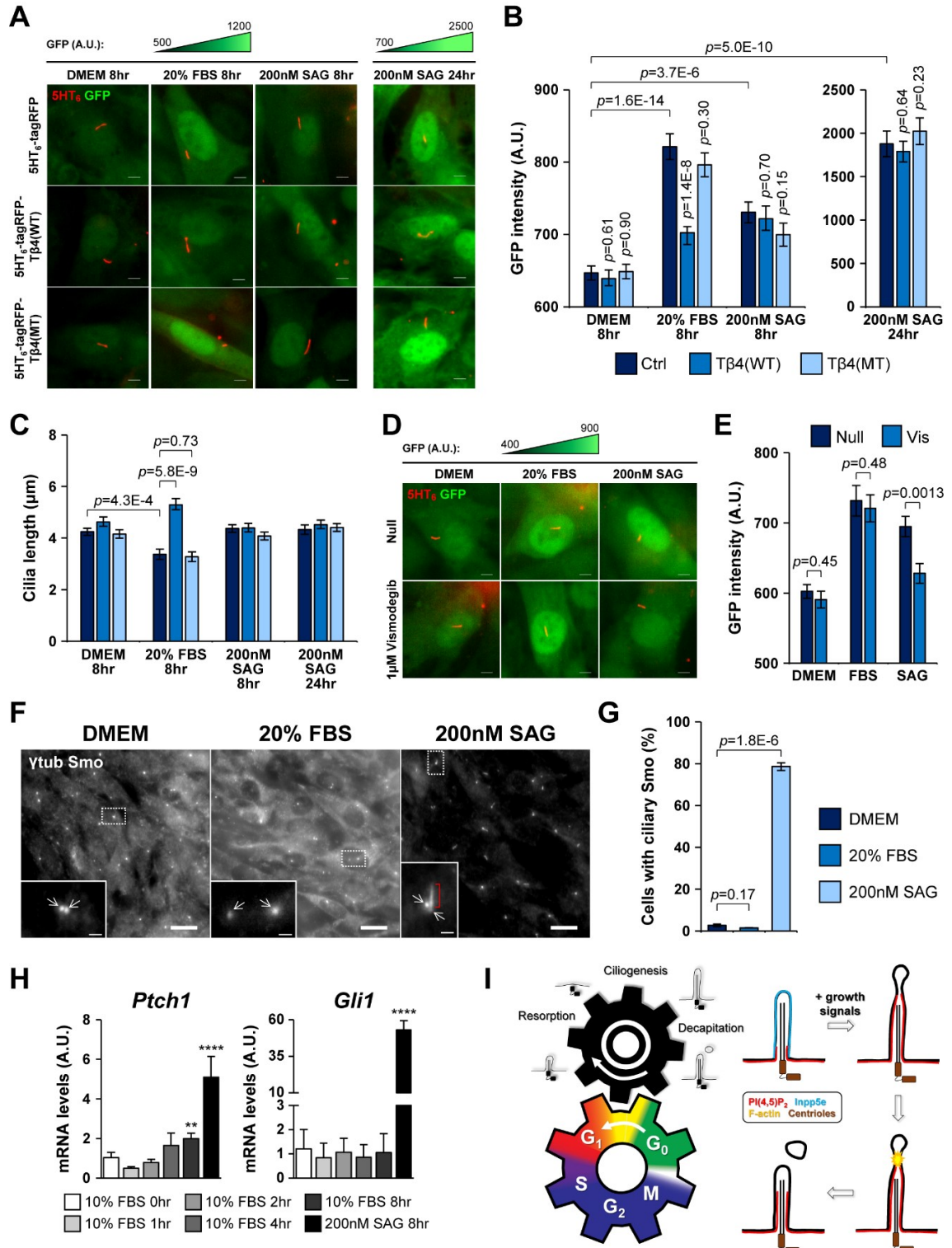


**Figure 4-15. Growth-induced Gli activation is dependent on cilia decapitation.**

- (A) Representative fluorescence images of NIH/3T3: 8xGBS-GFP reporter line under indicated conditions. GFP fluorescence intensities of the same column group are scaled to the same intensity ranges indicated above each group.
- (B) GFP fluorescence intensity measurements, as in (A). (n= 70, 89, 72, 64, 73, 70, 61, 77, 61, 39, 56 and 59 cells from left to right; 4 experiments)
- (C) Cilia length measurements in response to indicated stimuli and cilia-targeted probes; data derived from same experiments in (B).
- (D) Representative fluorescence images of NIH/3T3: 8xGBS-GFP reporter line at 8 hours under indicated conditions. GFP fluorescence intensities are scaled to the same intensity range.
- (E) GFP fluorescence intensity measurements, as in (D). (n= 39, 54, 48, 49, 43 and 44 cells from left to right; 3 experiments)
- (F)  $\gamma$ -tub and Smoothed (Smo) immunofluorescence on NIH/3T3: 8xGBS-GFP reporter line upon 8 hours with indicated conditions. Insets are magnifications of dotted regions. Arrows indicate centrioles. Red bracket indicates ciliary Smo signals.
- (G) Scoring % cells with ciliary Smo signals, as in (F). (n=249, 206, 239 cells from left to right; 3 experiments)
- (H) Quantitative real-time PCR assay for *Ptch1* and *Gli1* gene expression performed on NIH/3T3 post-stimulation with 10% FBS. An 8-hour 200nM SAG positive control for Smo-dependent Hedgehog signaling activation was included. *Ubc* was used to normalize *Ptch1* and *Gli1* transcript levels. Data shown as mean  $\pm$  SD; one-way ANOVA were performed to compare 0-hour 10% FBS samples with all other samples. \*\*  $p < 0.01$ ; \*\*\*\*  $p < 0.0001$  (n= 8 experiments)
- (I) Summary model of cilia decapitation during quiescence exit. (Left panel) Two meshing gears represent the mutual dependency between cell division cycle and primary cilium life cycle.

As known, growth induction (counterclockwise rotation of the bottom gear) promotes cilia disassembly (clockwise rotation of the top gear). The present study characterizes cilia decapitation as one of the key gear teeth enmeshing the two biological cycles. Cilia decapitation stimulates disassembly of cilia, and also modulates cell proliferation by inducing G<sub>1</sub> entry. (Right panel) Growth-stimulated cilia decapitation occurs through four major steps: (1) Inpp5e re-localization (2) PI(4,5)P<sub>2</sub> elevation (3) Actin polymerization (4) Cilia tip excision.

In (B), (C), (E), (G), data are shown as mean  $\pm$  SEM; Student's T-tests were performed between indicated sample pairs (horizontal *p* values), or with respect to each 5HT<sub>6</sub>-tagRFP condition (vertical *p* values). Scale bars indicate 5 $\mu$ m in (A) and (D), 20 $\mu$ m and 2 $\mu$ m in (F) and (F) insets respectively.



**Table 4-1. List of protein candidates detected twice or more in at least one experimental condition, Related to Figures 4-10A and B.**

Green, IFT-B components including related motor proteins; orange, IFT-A components; yellow, hedgehog signaling proteins; cyan, known ciliary proteins. Only the 57 proteins highlighted in Figure 4A are presented here. For a complete list of proteins, please refer to (Phua et al., 2017).

Protein ID	Protein Name	Times Detected			Ratio of Average Peak Area	
		WT 10%FBS (WT 10)	Ift88KO 10%FBS (KO 10)	WT 0.1%FBS (WT 0.1)	WT_10/ KO_10	WT_10/ WT_0.1
P15247	Interleukin-9 OS=Mus musculus GN=Il9 PE=1 SV=1 - [IL9_MOUSE]	2	0	0	195.40	331.77
Q5SYD0	Unconventional myosin-Id OS=Mus musculus GN=Myo1d PE=1 SV=1 - [MYO1D_MOUSE]	2	2	0	178.43	7187.72
Q6VH22	Intraflagellar transport protein 172 homolog OS=Mus musculus GN=Ifi172 PE=1 SV=1 - [IFI172_MOUSE]	9	0	1	148.59	46.78
O35594	Intraflagellar transport protein 81 homolog OS=Mus musculus GN=Ifi81 PE=1 SV=4 - [IFT81_MOUSE]	7	0	0	129.18	219.32
Q61371	Intraflagellar transport protein 88 homolog OS=Mus musculus GN=Ifi88 PE=1 SV=2 - [IFT88_MOUSE]	6	0	0	114.40	194.24
Q9D0P8	Intraflagellar transport protein 27 homolog OS=Mus musculus GN=Ifi27 PE=1 SV=1 - [IFT27_MOUSE]	3	0	0	105.81	179.65
Q8BKE9	Intraflagellar transport protein 74 homolog OS=Mus musculus GN=Ifi74 PE=1 SV=2 - [IFT74_MOUSE]	6	0	0	98.80	167.74
A6X935	Inter alpha-trypsin inhibitor, heavy chain 4 OS=Mus musculus GN=Itih4 PE=1 SV=2 - [ITIH4_MOUSE]	4	0	0	95.30	161.80
Q61838	Alpha-2-macroglobulin OS=Mus musculus GN=A2m PE=1 SV=3 - [A2M_MOUSE]	2	0	0	80.31	136.35
Q9DAI2	Intraflagellar transport protein 22 homolog OS=Mus musculus GN=Ifi22 PE=1 SV=1 - [IFT22_MOUSE]	5	0	0	78.75	133.70
Q8R3P7	Clusterin-associated protein 1 OS=Mus musculus GN=Cluap1 PE=1 SV=1 - [CLUA1_MOUSE]	5	0	0	75.16	127.60
Q9CY00	Tetratricopeptide repeat protein 30B OS=Mus musculus GN=Ttc30b PE=2 SV=1 - [TT30B_MOUSE]	5	0	0	74.63	126.72

Q640N2	ADP-ribosylation factor-like protein 13B OS=Mus musculus GN=Arl13b PE=1 SV=2 - [AR13B_MOUSE]	4	0	0	71.84	121.98
Q3TYG6	Protein FAM179A OS=Mus musculus GN=Fam179a PE=2 SV=1 - [F179A_MOUSE]	3	0	0	71.69	121.71
O70503	Estradiol 17-beta-dehydrogenase 12 OS=Mus musculus GN=Hsd17b12 PE=2 SV=1 - [DHB12_MOUSE]	3	0	0	69.12	117.36
P54775	26S protease regulatory subunit 6B OS=Mus musculus GN=Psmc4 PE=1 SV=2 - [PRS6B_MOUSE]	3	0	0	68.27	115.91
P48722	Heat shock 70 kDa protein 4L OS=Mus musculus GN=Hspa4l PE=1 SV=2 - [HS74L_MOUSE]	3	0	0	65.57	111.32
Q8BS45	Intraflagellar transport protein 56 OS=Mus musculus GN=Ttc26 PE=1 SV=1 - [IFT56_MOUSE]	3	0	0	63.78	108.29
Q61602	Transcriptional activator GLI3 OS=Mus musculus GN=Gli3 PE=1 SV=2 - [GLI3_MOUSE]	7	0	0	60.28	102.35
Q61771	Kinesin-like protein KIF3B OS=Mus musculus GN=Kif3b PE=1 SV=1 - [KIF3B_MOUSE]	7	0	0	59.74	101.43
Q9Z0P7	Suppressor of fused homolog OS=Mus musculus GN=Sufu PE=1 SV=1 - [SUFU_MOUSE]	4	0	0	54.47	92.48
P70188	Kinesin-associated protein 3 OS=Mus musculus GN=Kifap3 PE=1 SV=1 - [KIFA3_MOUSE]	5	0	1	52.97	11.48
Q9DB07	Intraflagellar transport protein 46 homolog OS=Mus musculus GN=Ifi46 PE=1 SV=1 - [IFT46_MOUSE]	4	0	0	52.68	89.45
Q61025	Intraflagellar transport protein 20 homolog OS=Mus musculus GN=Ifi20 PE=1 SV=1 - [IFT20_MOUSE]	5	0	0	50.10	85.06
Q8K057	Intraflagellar transport protein 80 homolog OS=Mus musculus GN=Ifi80 PE=1 SV=1 - [IFT80_MOUSE]	4	0	0	44.00	74.71
Q9QUJ7	Long-chain-fatty-acid--CoA ligase 4 OS=Mus musculus GN=Acs14 PE=2 SV=2 - [ACSL4_MOUSE]	3	0	0	43.02	73.03
Q3UGF1	WD repeat-containing protein 19 OS=Mus musculus GN=Wdr19 PE=1 SV=1 - [WDR19_MOUSE]	3	0	0	40.38	68.56
Q9D6H2	Intraflagellar transport protein 25 homolog OS=Mus musculus GN=Hspb11 PE=1 SV=2 - [IFT25_MOUSE]	2	0	0	35.30	59.94
Q8CGC6	RNA-binding protein 28 OS=Mus musculus GN=Rbm28 PE=1 SV=4 - [RBM28_MOUSE]	2	0	0	34.29	58.22
Q80YV3	Transformation/transcription domain-associated protein OS=Mus musculus GN=Trrap PE=1 SV=2 - [TRRAP_MOUSE]	2	0	0	33.88	57.53
Q9JII1	72 kDa inositol polyphosphate 5-phosphatase OS=Mus musculus	4	0	0	33.50	56.88

	GN=Inpp5e PE=1 SV=1 - [INP5E_MOUSE]					
Q0HA38	Tetratricopeptide repeat protein 21B OS=Mus musculus GN=Ttc21b PE=2 SV=1 - [TT21B_MOUSE]	3	0	0	31.53	53.53
P54227	Stathmin OS=Mus musculus GN=Stmn1 PE=1 SV=2 - [STMN1_MOUSE]	3	0	0	29.57	50.20
O88379	Bromodomain adjacent to zinc finger domain protein 1A OS=Mus musculus GN=Baz1a PE=1 SV=3 - [BAZ1A_MOUSE]	3	0	0	28.43	48.27
Q8CFI7	DNA-directed RNA polymerase II subunit RPB2 OS=Mus musculus GN=Polr2b PE=2 SV=2 - [RPB2_MOUSE]	2	0	0	26.40	44.82
P28741	Kinesin-like protein KIF3A OS=Mus musculus GN=Kif3a PE=1 SV=2 - [KIF3A_MOUSE]	8	1	0	26.01	862.75
Q149C2	TRAF3-interacting protein 1 OS=Mus musculus GN=Traf3ip1 PE=1 SV=2 - [MIPT3_MOUSE]	3	0	0	24.86	42.22
Q91VH2	Sorting nexin-9 OS=Mus musculus GN=Snx9 PE=1 SV=1 - [SNX9_MOUSE]	2	0	0	23.55	39.99
Q9WV60	Glycogen synthase kinase-3 beta OS=Mus musculus GN=Gsk3b PE=1 SV=2 - [GSK3B_MOUSE]	2	0	0	22.13	37.57
Q9D2R0	Acetoacetyl-CoA synthetase OS=Mus musculus GN=Aacs PE=2 SV=1 - [AACS_MOUSE]	2	0	0	22.12	37.56
Q80X41	Serine/threonine-protein kinase VRK1 OS=Mus musculus GN=Vrk1 PE=1 SV=2 - [VRK1_MOUSE]	3	0	0	21.88	37.14
Q8R5K4	Nucleolar protein 6 OS=Mus musculus GN=Nol6 PE=2 SV=2 - [NOL6_MOUSE]	2	0	0	20.51	34.83
Q8BND3	WD repeat-containing protein 35 OS=Mus musculus GN=Wdr35 PE=2 SV=3 - [WDR35_MOUSE]	2	0	0	20.38	34.59
P00375	Dihydrofolate reductase OS=Mus musculus GN=Dhfr PE=1 SV=3 - [DYR_MOUSE]	2	0	0	19.79	33.60
Q9DB85	Ribosomal RNA-processing protein 8 OS=Mus musculus GN=Rrp8 PE=1 SV=1 - [RRP8_MOUSE]	3	0	0	19.09	32.40
Q80X82	Symplekin OS=Mus musculus GN=Sympk PE=1 SV=1 - [SYMPK_MOUSE]	3	0	0	18.62	31.62
Q6NWX3	Intraflagellar transport protein 122 homolog OS=Mus musculus GN=Ifit122 PE=2 SV=1 - [IF122_MOUSE]	2	0	0	18.41	31.25
Q64282	Interferon-induced protein with tetratricopeptide repeats 1 OS=Mus musculus GN=Ifit1 PE=1 SV=2 - [IFIT1_MOUSE]	2	0	0	17.91	30.40
P30285	Cyclin-dependent kinase 4 OS=Mus musculus GN=Cdk4 PE=1 SV=1 - [CDK4_MOUSE]	3	0	0	16.61	28.20
Q9EP97	Sentrin-specific protease 3 OS=Mus	2	0	0	15.09	25.61

	musculus GN=Senp3 PE=1 SV=1 - [SEN3_MOUSE]					
Q9JKV2	Serine/threonine-protein kinase ICK OS=Mus musculus GN=Ick PE=2 SV=2 - [ICK_MOUSE]	2	0	0	14.90	25.29
Q5SSW2	Proteasome activator complex subunit 4 OS=Mus musculus GN=Psme4 PE=1 SV=1 - [PSME4_MOUSE]	3	0	0	14.38	24.42
Q9D1M0	Protein SEC13 homolog OS=Mus musculus GN=Sec13 PE=2 SV=3 - [SEC13_MOUSE]	4	3	1	13.90	291.65
Q8BXG3	Intraflagellar transport protein 57 homolog OS=Mus musculus GN=Ifi57 PE=1 SV=1 - [IFT57_MOUSE]	2	0	0	12.60	21.39
G5E870	E3 ubiquitin-protein ligase TRIP12 OS=Mus musculus GN=Trip12 PE=1 SV=1 - [TRIPC_MOUSE]	2	0	0	12.49	21.21
Q99LL5	Periodic tryptophan protein 1 homolog OS=Mus musculus GN=Pwp1 PE=1 SV=1 - [PWP1_MOUSE]	2	1	0	11.84	62.32
P42225	Signal transducer and activator of transcription 1 OS=Mus musculus GN=Stat1 PE=1 SV=1 - [STAT1_MOUSE]	3	1	0	11.36	54.39

**Table 4-2. List of protein candidates detected twice or more in growth-stimulated WT or *Ift88*-KO mIMCD-3 conditioned culture media, Related to Figures 4-10 C and D.**

Proteins were ranked according to  $\text{Log}_2[\text{WT}/\text{Ift88KO}]$  and corresponding Z-scores. Color coding as in Table 4-1. Only protein hits with Z-scores  $>1.960$  are presented here. For a complete list of proteins, please refer to (Phua et al., 2017).

Protein ID	Protein Name	Average Peak Area		Ratios		Z-score
		WT 10%FBS	Ift88KO 10%FBS	WT/Ift88KO	Log <sub>2</sub>	
P15247	Interleukin-9 OS=Mus musculus GN=Il9 PE=1 SV=1 - [IL9_MOUSE]	2.4E7	1.2E5	195.4	7.61	4.37
Q5SYD0	Unconventional myosin-Id OS=Mus musculus GN=Myo1d PE=1 SV=1 - [MYO1D_MOUSE]	5.1E8	2.9E6	178.4	7.48	4.30
Q6VH22	Intraflagellar transport protein 172 homolog OS=Mus musculus GN=Ifi172 PE=1 SV=1 - [IF172_MOUSE]	1.8E7	1.2E5	148.6	7.22	4.16
O35594	Intraflagellar transport protein 81 homolog OS=Mus musculus GN=Ifi81 PE=1 SV=4 - [IFT81_MOUSE]	1.6E7	1.2E5	129.2	7.01	4.05
Q61371	Intraflagellar transport protein 88 homolog OS=Mus musculus GN=Ifi88 PE=1 SV=2 - [IFT88_MOUSE]	1.4E7	1.2E5	114.4	6.84	3.96
Q9D0P8	Intraflagellar transport protein 27 homolog OS=Mus musculus GN=Ifi27 PE=1 SV=1 - [IFT27_MOUSE]	1.3E7	1.2E5	105.8	6.73	3.90
Q8BKE9	Intraflagellar transport protein 74 homolog OS=Mus musculus GN=Ifi74 PE=1 SV=2 - [IFT74_MOUSE]	1.2E7	1.2E5	98.8	6.63	3.84
A6X935	Inter alpha-trypsin inhibitor, heavy chain 4 OS=Mus musculus GN=Itih4 PE=1 SV=2 - [ITIH4_MOUSE]	1.2E7	1.2E5	95.3	6.57	3.82
Q61838	Alpha-2-macroglobulin OS=Mus musculus GN=A2m PE=1 SV=3 - [A2M_MOUSE]	9.7E6	1.2E5	80.3	6.33	3.68
Q9DAI2	Intraflagellar transport protein 22 homolog OS=Mus musculus GN=Ifi22 PE=1 SV=1 - [IFT22_MOUSE]	9.5E6	1.2E5	78.7	6.30	3.67
Q8R3P7	Clusterin-associated protein 1 OS=Mus musculus GN=Cluap1 PE=1 SV=1 - [CLUA1_MOUSE]	9.1E6	1.2E5	75.2	6.23	3.63
Q9CY00	Tetratricopeptide repeat protein 30B OS=Mus musculus GN=Ttc30b PE=2 SV=1 - [TT30B_MOUSE]	9.0E6	1.2E5	74.6	6.22	3.63
Q640N2	ADP-ribosylation factor-like protein 13B OS=Mus musculus GN=Arl13b PE=1 SV=2 - [AR13B_MOUSE]	8.7E6	1.2E5	71.8	6.17	3.60

Q3TYG6	Protein FAM179A OS=Mus musculus GN=Fam179a PE=2 SV=1 - [F179A_MOUSE]	8.7E6	1.2E5	71.7	6.16	3.60
O70503	Estradiol 17-beta-dehydrogenase 12 OS=Mus musculus GN=Hsd17b12 PE=2 SV=1 - [DHB12_MOUSE]	8.3E6	1.2E5	69.1	6.11	3.57
P54775	26S protease regulatory subunit 6B OS=Mus musculus GN=Psmc4 PE=1 SV=2 - [PRS6B_MOUSE]	8.2E6	1.2E5	68.3	6.09	3.56
P48722	Heat shock 70 kDa protein 4L OS=Mus musculus GN=Hspa4l PE=1 SV=2 - [HS74L_MOUSE]	7.9E6	1.2E5	65.6	6.03	3.53
Q8BS45	Intraflagellar transport protein 56 OS=Mus musculus GN=Ttc26 PE=1 SV=1 - [IFT56_MOUSE]	7.7E6	1.2E5	63.8	6.00	3.51
Q61602	Transcriptional activator GLI3 OS=Mus musculus GN=Gli3 PE=1 SV=2 - [GLI3_MOUSE]	7.3E6	1.2E5	60.3	5.91	3.46
Q61771	Kinesin-like protein KIF3B OS=Mus musculus GN=Kif3b PE=1 SV=1 - [KIF3B_MOUSE]	7.2E6	1.2E5	59.7	5.90	3.46
Q9Z0P7	Suppressor of fused homolog OS=Mus musculus GN=Sufu PE=1 SV=1 - [SUFU_MOUSE]	6.6E6	1.2E5	54.5	5.77	3.39
Q9Z2N8	Actin-like protein 6A OS=Mus musculus GN=Actl6a PE=1 SV=2 - [ACL6A_MOUSE]	6.5E6	1.2E5	53.6	5.74	3.37
P70188	Kinesin-associated protein 3 OS=Mus musculus GN=Kifap3 PE=1 SV=1 - [KIFA3_MOUSE]	6.4E6	1.2E5	53.0	5.73	3.36
Q9DB07	Intraflagellar transport protein 46 homolog OS=Mus musculus GN=Ifa46 PE=1 SV=1 - [IFT46_MOUSE]	6.4E6	1.2E5	52.7	5.72	3.36
Q61025	Intraflagellar transport protein 20 homolog OS=Mus musculus GN=Ifa20 PE=1 SV=1 - [IFT20_MOUSE]	6.0E6	1.2E5	50.1	5.65	3.32
Q9WUL7	ADP-ribosylation factor-like protein 3 OS=Mus musculus GN=Arl3 PE=1 SV=1 - [ARL3_MOUSE]	5.4E6	1.2E5	44.9	5.49	3.24
Q8K057	Intraflagellar transport protein 80 homolog OS=Mus musculus GN=Ifa80 PE=1 SV=1 - [IFT80_MOUSE]	5.3E6	1.2E5	44.0	5.46	3.22
Q9QUJ7	Long-chain-fatty-acid--CoA ligase 4 OS=Mus musculus GN=Acsl4 PE=2 SV=2 - [ACSL4_MOUSE]	5.2E6	1.2E5	43.0	5.43	3.20
Q3UGF1	WD repeat-containing protein 19 OS=Mus musculus GN=Wdr19 PE=1 SV=1 - [WDR19_MOUSE]	4.9E6	1.2E5	40.4	5.34	3.15
Q9D6H2	Intraflagellar transport protein 25 homolog OS=Mus musculus GN=Hspb11 PE=1 SV=2 - [IFT25_MOUSE]	4.3E6	1.2E5	35.3	5.14	3.05
Q8CGC6	RNA-binding protein 28 OS=Mus musculus GN=Rbm28 PE=1 SV=4 - [RBM28_MOUSE]	4.1E6	1.2E5	34.3	5.10	3.03
Q80YV3	Transformation/transcription domain- associated protein OS=Mus musculus GN=Trrap PE=1 SV=2 - [TRRAP_MOUSE]	4.1E6	1.2E5	33.9	5.08	3.02
Q9JII1	72 kDa inositol polyphosphate 5- phosphatase OS=Mus musculus	4.0E6	1.2E5	33.5	5.07	3.01

	GN=Inpp5e PE=1 SV=1 - [INP5E_MOUSE]					
Q8R143	Pituitary tumor-transforming gene 1 protein-interacting protein OS=Mus musculus GN=Pttg1ip PE=1 SV=1 - [PTTG_MOUSE]	3.8E6	1.2E5	31.6	4.98	2.97
Q0HA38	Tetratricopeptide repeat protein 21B OS=Mus musculus GN=Ttc21b PE=2 SV=1 - [TT21B_MOUSE]	3.8E6	1.2E5	31.5	4.98	2.96
Q80UG5	Septin-9 OS=Mus musculus GN=Sept9 PE=1 SV=1 - [SEPT9_MOUSE]	3.6E6	1.2E5	30.0	4.91	2.93
P54227	Stathmin OS=Mus musculus GN=Stmn1 PE=1 SV=2 - [STMN1_MOUSE]	3.6E6	1.2E5	29.6	4.89	2.91
O88379	Bromodomain adjacent to zinc finger domain protein 1A OS=Mus musculus GN=Baz1a PE=1 SV=3 - [BAZ1A_MOUSE]	3.4E6	1.2E5	28.4	4.83	2.88
Q9WUK2	Eukaryotic translation initiation factor 4H OS=Mus musculus GN=Eif4h PE=1 SV=3 - [IF4H_MOUSE]	3.3E6	1.2E5	27.7	4.79	2.86
Q8CFI7	DNA-directed RNA polymerase II subunit RPB2 OS=Mus musculus GN=Polr2b PE=2 SV=2 - [RPB2_MOUSE]	3.2E6	1.2E5	26.4	4.72	2.83
P28741	Kinesin-like protein KIF3A OS=Mus musculus GN=Kif3a PE=1 SV=2 - [KIF3A_MOUSE]	6.1E7	2.4E6	26.0	4.70	2.82
Q149C2	TRAF3-interacting protein 1 OS=Mus musculus GN=Traf3ip1 PE=1 SV=2 - [MIPT3_MOUSE]	3.0E6	1.2E5	24.9	4.64	2.78
Q91VH2	Sorting nexin-9 OS=Mus musculus GN=Snx9 PE=1 SV=1 - [SNX9_MOUSE]	2.8E6	1.2E5	23.6	4.56	2.74
P01887	Beta-2-microglobulin OS=Mus musculus GN=B2m PE=1 SV=2 - [B2MG_MOUSE]	2.8E6	1.2E5	23.5	4.56	2.74
Q9WV60	Glycogen synthase kinase-3 beta OS=Mus musculus GN=Gsk3b PE=1 SV=2 - [GSK3B_MOUSE]	2.7E6	1.2E5	22.1	4.47	2.69
Q9D2R0	Acetoacetyl-CoA synthetase OS=Mus musculus GN=Aacs PE=2 SV=1 - [AACS_MOUSE]	2.7E6	1.2E5	22.1	4.47	2.69
Q80X41	Serine/threonine-protein kinase VRK1 OS=Mus musculus GN=Vrk1 PE=1 SV=2 - [VRK1_MOUSE]	2.6E6	1.2E5	21.9	4.45	2.68
Q8R5K4	Nucleolar protein 6 OS=Mus musculus GN=Nol6 PE=2 SV=2 - [NOL6_MOUSE]	2.5E6	1.2E5	20.5	4.36	2.63
Q8BND3	WD repeat-containing protein 35 OS=Mus musculus GN=Wdr35 PE=2 SV=3 - [WDR35_MOUSE]	2.5E6	1.2E5	20.4	4.35	2.63
P00375	Dihydrofolate reductase OS=Mus musculus GN=Dhfr PE=1 SV=3 - [DYS_MOUSE]	2.4E6	1.2E5	19.8	4.31	2.61
Q9R118	Serine protease HTRA1 OS=Mus musculus GN=Htra1 PE=1 SV=2 - [HTRA1_MOUSE]	2.3E6	1.2E5	19.1	4.26	2.58
Q9DB85	Ribosomal RNA-processing protein 8 OS=Mus musculus GN=Rrp8 PE=1 SV=1 - [RRP8_MOUSE]	2.3E6	1.2E5	19.1	4.25	2.58

Q61249	Immunoglobulin-binding protein 1 OS=Mus musculus GN=[gbp1 PE=1 SV=1 - [IGBP1_MOUSE]	2.3E6	1.2E5	18.8	4.24	2.57
Q80X82	Symplekin OS=Mus musculus GN=Sympk PE=1 SV=1 - [SYMPK_MOUSE]	2.2E6	1.2E5	18.6	4.22	2.56
Q6NWV3	Intraflagellar transport protein 122 homolog OS=Mus musculus GN=Ift122 PE=2 SV=1 - [IF122_MOUSE]	2.2E6	1.2E5	18.4	4.20	2.55
Q64282	Interferon-induced protein with tetratricopeptide repeats 1 OS=Mus musculus GN=Ift1 PE=1 SV=2 - [IFIT1_MOUSE]	2.2E6	1.2E5	17.9	4.16	2.53
P62627	Dynein light chain roadblock-type 1 OS=Mus musculus GN=Dynlrb1 PE=1 SV=3 - [DLRB1_MOUSE]	2.1E6	1.2E5	17.5	4.13	2.51
P30285	Cyclin-dependent kinase 4 OS=Mus musculus GN=Cdk4 PE=1 SV=1 - [CDK4_MOUSE]	2.0E6	1.2E5	16.6	4.05	2.47
Q9EP97	Sentrin-specific protease 3 OS=Mus musculus GN=Senp3 PE=1 SV=1 - [SEN3_MOUSE]	1.8E6	1.2E5	15.1	3.92	2.40
Q9JKV2	Serine/threonine-protein kinase ICK OS=Mus musculus GN=Ick PE=2 SV=2 - [ICK_MOUSE]	1.8E6	1.2E5	14.9	3.90	2.39
Q5SSW2	Proteasome activator complex subunit 4 OS=Mus musculus GN=Psme4 PE=1 SV=1 - [PSME4_MOUSE]	1.7E6	1.2E5	14.4	3.85	2.36
Q9D1M0	Protein SEC13 homolog OS=Mus musculus GN=Sec13 PE=2 SV=3 - [SEC13_MOUSE]	1.3E8	9.2E6	13.9	3.80	2.33
O70591	Prefoldin subunit 2 OS=Mus musculus GN=Pfdn2 PE=2 SV=2 - [PFD2_MOUSE]	1.6E6	1.2E5	13.5	3.75	2.31
Q8BXG3	Intraflagellar transport protein 57 homolog OS=Mus musculus GN=Ift57 PE=1 SV=1 - [IFT57_MOUSE]	1.5E6	1.2E5	12.6	3.66	2.26
G5E870	E3 ubiquitin-protein ligase TRIP12 OS=Mus musculus GN=Trip12 PE=1 SV=1 - [TRIPC_MOUSE]	1.5E6	1.2E5	12.5	3.64	2.25
Q99LL5	Periodic tryptophan protein 1 homolog OS=Mus musculus GN=Pwp1 PE=1 SV=1 - [PWP1_MOUSE]	4.4E6	3.7E5	11.8	3.57	2.21
P42225	Signal transducer and activator of transcription 1 OS=Mus musculus GN=Stat1 PE=1 SV=1 - [STAT1_MOUSE]	3.9E6	3.4E5	11.4	3.51	2.18
Q9CX86	Heterogeneous nuclear ribonucleoprotein A0 OS=Mus musculus GN=Hnrnpa0 PE=1 SV=1 - [ROA0_MOUSE]	6.0E6	5.6E5	10.6	3.41	2.12
Q8VE37	Regulator of chromosome condensation OS=Mus musculus GN=Rcc1 PE=1 SV=1 - [RCC1_MOUSE]	1.2E6	1.2E5	10.3	3.36	2.10
Q06335	Amyloid-like protein 2 OS=Mus musculus GN=Aplp2 PE=1 SV=4 - [APLP2_MOUSE]	1.2E6	1.2E5	9.6	3.26	2.05
Q9WV70	Nucleolar complex protein 2 homolog OS=Mus musculus GN=Noc2l PE=1 SV=2 - [NOC2L_MOUSE]	1.2E6	1.2E5	9.6	3.26	2.04



P54276	DNA mismatch repair protein Msh6 OS=Mus musculus GN=Msh6 PE=1 SV=3 - [MSH6_MOUSE]	4.1E6	4.5E5	9.0	3.18	2.00
P21995	Embigin OS=Mus musculus GN=Emb PE=1 SV=2 - [EMB_MOUSE]	1.1E6	1.2E5	9.0	3.17	2.00

## Chapter 5 Overall Conclusion and Outlook

By designing and building molecular tools to visualize and manipulate signaling in primary cilia, we have achieved both technological and mechanistic advancements in cilia biology. The molecular strategies used in these studies are relevant to a broad, interdisciplinary audience in the fields of cell and developmental biology, genetics, and technology development. Targeting various probes to the ciliary membrane has been an effective strategy to actuate specific properties in primary cilia e.g. phosphoinositide metabolism and actin polymerization. This could be attributed to the femto-scale volume of the primary cilia which allow a few number of molecules achieve a high local concentration. Hence, it is possible to extend this strategy to other signaling modules in primary cilia, or even other organelles in the cell.

We have elucidated pivotal roles of PI(4,5)P<sub>2</sub> in dictating the function and structure identity of primary cilia. By recruiting Inpp5e as a rheostat, primary cilia tune the dynamics of phosphoinositides to perform unique functions (Garcia-Gonzalo et al., 2015; Phua et al., 2017). In contrast with most organelles whose identities depend on the presence of certain phosphoinositides to recruit organelle-specific proteins or modulate specific organellar protein function (Shewan et al., 2011), primary cilia entail a strict depletion of PI(4,5)P<sub>2</sub> in the ciliary membrane. The absence of PI(4,5)P<sub>2</sub> empowers primary cilia with an identity distinct from the surrounding plasma membrane, thereby ensuring a proper ciliary distribution of signaling proteins and cilia stability.

Inpp5e also neatly connects ciliary signaling with cell cycle progression through phosphoinositides and extracellular vesicles (Phua et al., 2017). Recently, Inpp5e has been reported to suppress mTOR-dependent cystogenesis in the kidney through the inhibition of PI(3,4,5)P<sub>3</sub> (Hakim et al., 2016). Interestingly, we have also determined a role of Inpp5e in suppressing cilia decapitation which could regulate mTOR-dependent Gli1 activation and

quiescence exit (Phua et al., 2017). The related conclusions from these works suggest that renal cystogenesis may entail extracellular vesicle signaling, and this is corroborated by the observation of increased urinary exosome formation in certain forms of polycystic kidney disease (Hogan et al., 2009). The same signaling pathway could also be involved in tumorigenesis since elevated PI3K and PI(3,4,5)P<sub>3</sub> are well-defined indicators of cancers (Bunney and Katan, 2010). On the other hand, it is pertinent to determine how cancerous cells may alter the membrane lipid composition and the function of primary cilia to promote survival and proliferative signaling. Therefore, phosphoinositide metabolism in primary cilia has far-reaching consequences on cell function, and it is imperative to understand the roles of other cilia-associated lipid kinases and phosphatases such as OCRL.

The launch of genetically-encoded cilia-targeted calcium indicators allows us to visualize Ca<sup>2+</sup> signals in the cilia for the first time (Su et al., 2013). The next step is to understand how the TRP channels in cilia function, such as the nature of the channel gating stimuli. Unfortunately, progress in this area has been afflicted with contradictory reports. While many reports have commonly propose primary cilia mechano-transduction of fluid flow through Ca<sup>2+</sup> signals, Delling et al. recently reported an absence of ciliary Ca<sup>2+</sup> signals in a variety of cellular systems, including dissected kidney tubules and embryonic node *ex vivo* culture, upon fluid flow induction (Delling et al., 2016). However, interpretation of ciliary Ca<sup>2+</sup> signals requires much precaution. The small volume of the primary cilia makes it especially susceptible to poor signal-to-noise ratios; it is thus challenging to detect reliable intraciliary Ca<sup>2+</sup> signals which can be very acute and transient in nature. In addition, the proximal ciliary base permits Ca<sup>2+</sup> ions to diffuse freely from cytosol into cilia (Delling et al., 2013; Lin et al., 2013), and it is pertinent to dissect and resolve ciliary membrane Ca<sup>2+</sup> influx from cytosolic Ca<sup>2+</sup> propagation, albeit both could perform meaningful functions in primary cilia. Moreover, many proposed functions of ciliary TRP channels occur in the context of embryonic development which may not be sufficiently

recapitulated using *in vitro* cultures. In conclusion, it would be the most ideal to visualize ciliary  $\text{Ca}^{2+}$  dynamics *in vivo*, as primary cilia movement dynamics in live intact kidney has already been visualized (O'Connor et al., 2013).

To ascertain the significance of ciliary  $\text{Ca}^{2+}$  signals, one strategy is to determine the factors that can regulate it. Using the cilia-targeted  $\text{Ca}^{2+}$  indicators we developed, we determined initial results that the basal  $[\text{Ca}^{2+}]$  in *Inpp5e*<sup>-/-</sup> MEF primary cilia could be higher than that of *Inpp5e*<sup>+/-</sup> MEF (**Figure 5-1**). This suggests that augmented PI(4,5)P<sub>2</sub> (and/or lower PI(4)P) in ciliary membrane could increase the open probability of TRP channels in cilia. PI(4,5)P<sub>2</sub> is an established regulator of the TRP channels through indirect and direct mechanisms (Rohacs, 2009). By acting as a substrate of phospholipase C- $\beta/\gamma$ , PI(4,5)P<sub>2</sub> is broken down into IP<sub>3</sub> and DAG, which regulates the canonical sub-family of TRP channels including TRPC1 (Abramowitz et al., 2007; Shi et al., 2014). Direct binding of TRPC1 and TRPV4 with PI(4,5)P<sub>2</sub> induces conformational changes that prime them for channel opening (Garcia-Elias et al., 2013; Shi et al., 2014). In contrast, Ma et al. reported that TRPP2 is inhibited by high levels of PI(4,5)P<sub>2</sub> in the membrane (Ma et al., 2005). It is plausible that the ciliary membrane density of PI(4,5)P<sub>2</sub> could modulate TRP channel function in primary cilia. To further pursue this direction, we propose to knock down specific TRP channel expression in *Inpp5e*<sup>-/-</sup> MEF and measure the resultant ciliary  $[\text{Ca}^{2+}]$ .

Furthermore, we determined a role of *Inpp5e* in regulating the localization of calmodulin (CaM). CaM interacts with pericentriolar proteins and localizes around the centrosome (Moisoi et al., 2002; Willingham et al., 1983). Whereas over-expressed CaM often displays pericentriolar localization in *Inpp5e*<sup>+/-</sup> MEF, we found that a complete loss of *Inpp5e* significantly reduces the occurrence of this localization (**Figure 5-1**). It is tempting to speculate that the higher basal ciliary  $[\text{Ca}^{2+}]$  in *Inpp5e*<sup>-/-</sup> cells could deliver  $\text{Ca}^{2+}$  ions to the ciliary base and regulate the binding of CaM with pericentriolar proteins. Nonetheless, more work is needed to concretely form a link

between these results, such as expressing cilia-targeted PIPK/Inp54p to directly test the involvement of ciliary PI(4,5)P<sub>2</sub>/PI(4)P. Importantly, several proteins associated with primary cilia are regulated by Ca<sup>2+</sup>/CaM action. The proximal segment of primary cilium is organized by a highly conserved protein known as inversin (Shiba et al., 2009). Loss of function of inversin is associated with left-right determination defects and renal cysts (Otto et al., 2003). Interestingly, inversin contains two IQ domains (IQ1 and IQ2). *In vitro* studies have not only demonstrated direct CaM binding by these IQ domains, but also revealed that CaM-binding with IQ2 domain is negatively regulated by Ca<sup>2+</sup> (Yasuhiko et al., 2001). Since CaM has also been reported in primary cilia of several cell types (Eley et al., 2004; Otto et al., 2005; Shiba et al., 2009), one could speculate that the Inpp5e-dependent changes in CaM pericentriolar localization could regulate inversin-CaM interaction within the primary cilia. Moreover, several ciliary TRP channels possess CaM interaction sites which modulate channel activity (Singh et al., 2002; Strotmann et al., 2003). Deciphering the functional interaction between inversin, CaM and ciliary TRP channels could reveal their role in mediating embryonic patterning and kidney morphogenesis. Moreover, the master controller of cilia disassembly, Aurora A kinase, localizes at the centrosome and exhibits Ca<sup>2+</sup>/CaM-dependent activity (Plotnikova et al., 2012). There is hence likelihood that ciliary Ca<sup>2+</sup> dynamics is involved in cilia stability. These results encourage future studies of how the ciliary [Ca<sup>2+</sup>] regulates the localization and activities of these ciliary effectors.

Extracellular vesicles could represent a common *modus operandi* for cilia-localized developmental signaling pathways, and could potentially explain why they are housed within the primary cilia. Hedgehog, Wnt and Notch are principal morphogens sensed by primary cilia which are released externally in the form of exosomes (Gross et al., 2012; Panáková et al., 2005; Sheldon et al., 2010). The reason why these morphogens are tethered on vesicles are not well understood, but one reason could be that the additional ligands presented on the surface of these

vesicles could act as co-modulators in these morphogen signaling pathways (Vyas et al., 2014). Regardless, primary cilia could possess specialized features which promote the detection of these morphogen-loaded extracellular vesicles. Structurally, the projection of primary cilia away from the planar cell surface provides a higher surface area and hence probability for encountering these vesicles (see Section 1.2). There could also be adhesive proteins on the surface of ciliary membrane that bind with these vesicles. Indeed, cilia-cilia contacts have been observed in kidney cells through a glycoprotein-dependent mechanism (Ott et al., 2012). In Chapter 4, we revealed that primary cilia could be a source of extracellular vesicles through growth-stimulated cilia decapitation (Phua et al., 2017). Signaling proteins such as Hedgehog regulators were detected within the resultant ciliary vesicles, and it would be interesting to assess the effect on cells which internalize these vesicles. This prospect is supported by our observation that the MEF ciliary vesicles tend to be sticky and associate with the cell surface upon release. Since cilia decapitation is a growth signal-dependent process, it is also worth to see if growth factor receptors can be detected in the ciliary vesicles. Accordingly, another group has recently proposed ciliary vesicle release as a specialized outlet for activated ciliary GPCRs (Nager et al., 2017). Moreover, polycystic kidney disease is associated with an exaggerated occurrence of urinary exosomes which tend to associate with the kidney primary cilia (Hogan et al., 2009). These exosomes are found to be enriched with PKD2 proteins, which suggest that they could be originally released from the primary cilia. Overall, primary cilia could dually serve as a transmitter and receiver of extracellular vesicles that are crucial for the proper execution of developmental signaling pathways (Wood and Rosenbaum, 2015). This function could be reinforced by the presence of a sophisticated intraflagellar transport system in primary cilia which may be exploited to customize the contents of ciliary vesicles (Mourão et al., 2016).

In conclusion, primary cilia exemplify a perfect model to study the cause and effect of spatiotemporal signaling. The novel principles of ciliary signaling we discovered through these

series of studies construct a solid ground for understanding the role of primary cilia in vertebrate development, as well as the disorders caused by sensory defects of the cellular antennae.

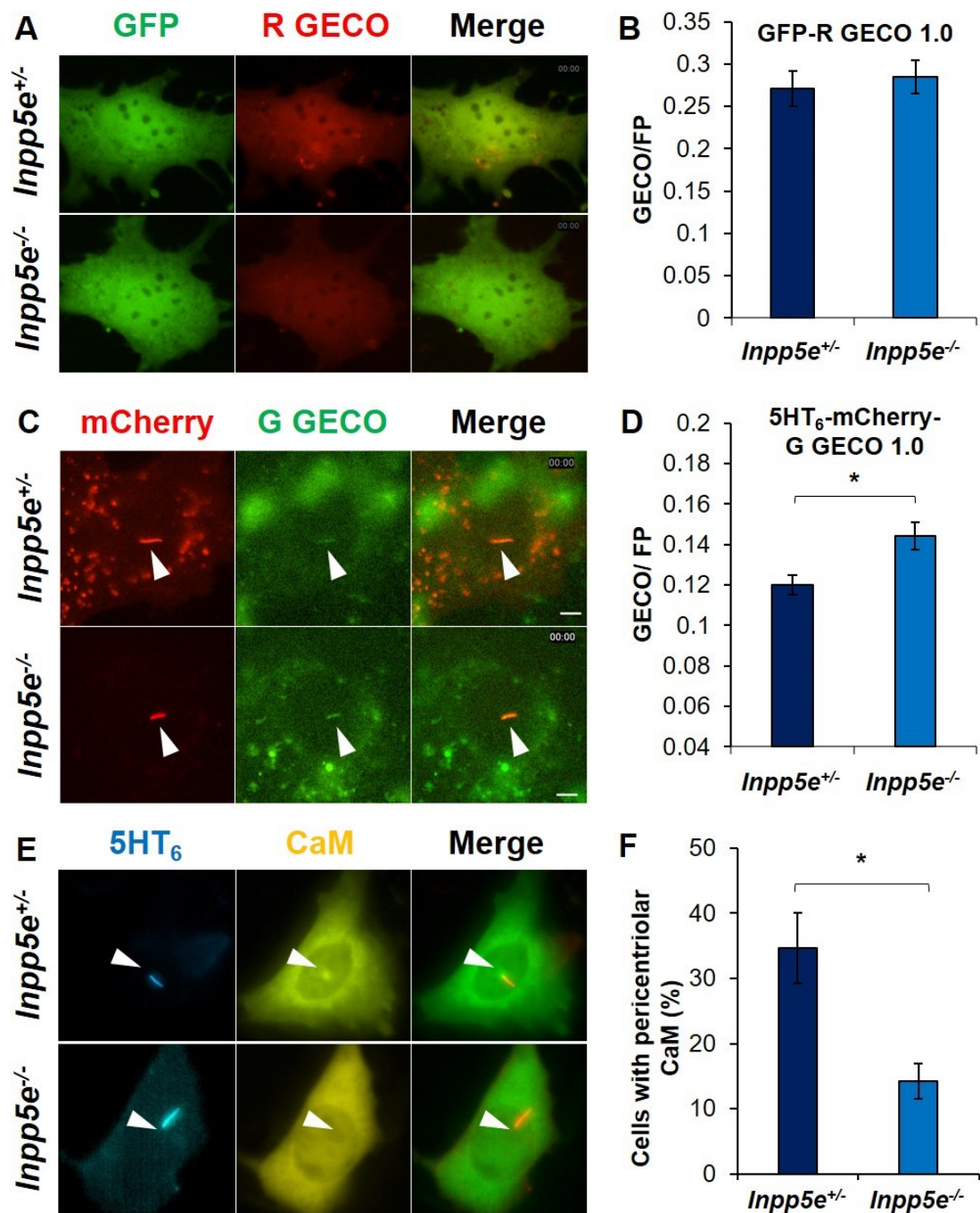




**Figure 5-1. Effect of *Inpp5e* on basal cellular and ciliary  $[Ca^{2+}]$  and pericentriolar localization of calmodulin.**

- (A) Representative live fluorescence images of quiescent *Inpp5e*<sup>+/−</sup> and *Inpp5e*<sup>−/−</sup> MEF expressing GFP-R GECO 1.0 for measurement of cytosolic  $[Ca^{2+}]$  based on RFP fluorescence intensity (see Chapter 3). Images of each wavelength are scaled to the same intensity range.
- (B) Comparison of relative cytosolic  $[Ca^{2+}]$  in quiescent *Inpp5e*<sup>+/−</sup> and *Inpp5e*<sup>−/−</sup> MEF based on  $R\ GECO\ 1.0\ intensity / GFP\ intensity$ . The cytosolic calcium indicator revealed that the basal cytosolic  $[Ca^{2+}]$  in these cells are comparable. (n= 15, 17 from left to right; 2-3 experiments).
- (C) Representative live fluorescence images of quiescent *Inpp5e*<sup>+/−</sup> and *Inpp5e*<sup>−/−</sup> MEF expressing 5HT<sub>6</sub>-mCherry-G GECO 1.0 for measurement of ciliary  $[Ca^{2+}]$  based on GFP fluorescence intensity (see Chapter 3). Arrowheads mark cilia. Images of each wavelength are scaled to the same intensity range.
- (D) Comparison of relative ciliary  $[Ca^{2+}]$  in quiescent *Inpp5e*<sup>+/−</sup> and *Inpp5e*<sup>−/−</sup> MEF based on  $G\ GECO\ 1.0\ intensity / GFP\ intensity$ . The cilia-targeted calcium indicator revealed that the basal ciliary  $[Ca^{2+}]$  in *Inpp5e*<sup>−/−</sup> MEF is significantly higher than that in *Inpp5e*<sup>+/−</sup> MEF. (n= 65, 63 from left to right; 2-3 experiments)
- (E) Representative live fluorescence images of quiescent *Inpp5e*<sup>+/−</sup> and *Inpp5e*<sup>−/−</sup> MEF expressing 5HT<sub>6</sub>-mCerule3 and Venus-calmodulin (CaM). Arrowheads mark the pericentriolar region.
- (F) Quantification of percentage of quiescent *Inpp5e*<sup>+/−</sup> and *Inpp5e*<sup>−/−</sup> MEF displaying pericentriolar localization of Venus-CaM. Complete loss of *Inpp5e* reduces the occurrence of calmodulin pericentriolar localization. (n= 62, 69 from left to right; 2-3 experiments)

## Bibliography

- Abramowitz, J., Yildirim, E., and Birnbaumer, L. (2007). The TRPC Family of Ion Channels: Relation to the TRP Superfamily and Role in Receptor- and Store-Operated Calcium Entry. In *TRP Ion Channel Function in Sensory Transduction and Cellular Signaling Cascades.*, W. Liedtke, and S. Heller, eds. (Boca Raton (FL): CRC Press/Taylor & Francis).
- Akerboom, J., Chen, T.-W., Wardill, T.J., Tian, L., Marvin, J.S., Mutlu, S., Carreras Caldéron, N., Esposti, F., Borghuis, B.G., Sun, X.R., et al. (2012). Optimization of a GCaMP Calcium Indicator for Neural Activity Imaging. *J. Neurosci.* *32*, 13819–13840.
- Babu, D., and Roy, S. (2013). Left-right asymmetry: cilia stir up new surprises in the node. *Open Biol.* *3*, 130052.
- Bai, C.-X., Giamarchi, A., Rodat-Despoix, L., Padilla, F., Downs, T., Tsiokas, L., and Delmas, P. (2008). Formation of a new receptor-operated channel by heteromeric assembly of TRPP2 and TRPC1 subunits. *EMBO Rep.* *9*, 472–479.
- Bangs, F.K., Schrode, N., Hadjantonakis, A.-K., and Anderson, K. V (2015). Lineage specificity of primary cilia in the mouse embryo. *Nat. Cell Biol.* *17*, 113–122.
- Berbari, N.F., Johnson, A.D., Lewis, J.S., Askwith, C.C., and Mykityn, K. (2008). Identification of Ciliary Localization Sequences within the Third Intracellular Loop of G Protein-coupled Receptors. *Mol. Biol. Cell* *19*, 1540–1547.
- Berbari, N.F., O'Connor, A.K., Haycraft, C.J., and Yoder, B.K. (2009). The Primary Cilium as a Complex Signaling Center. *Curr. Biol.* *19*.
- Bergman, K., Goodenough, U.W., Goodenough, D.A., Jawitz, J., and Martin, H. (1975). Gametic differentiation in *Chlamydomonas reinhardtii*. II. Flagellar membranes and the agglutination reaction. *J. Cell Biol.* *67*, 606–622.
- Bhogaraju, S., Cajanek, L., Fort, C., Blisnick, T., Weber, K., Taschner, M., Mizuno, N., Lamla, S., Bastin, P., Nigg, E.A., et al. (2013). Molecular Basis of Tubulin Transport Within the Cilium by IFT74 and IFT81. *Science.* *341*, 1009–1012.
- Bielas, S.L., Silhavy, J.L., Brancati, F., Kisseleva, M. V, Al-Gazali, L., Sztriha, L., Bayoumi, R. a, Zaki, M.S., Abdel-Aleem, A., Rosti, R.O., et al. (2009). Mutations in INPP5E, encoding inositol polyphosphate-5-phosphatase E, link phosphatidyl inositol signaling to the ciliopathies. *Nat. Genet.* *41*, 1032–1036.
- Boehlke, C., Kotsis, F., Patel, V., Braeg, S., Voelker, H., Brecht, S., Beyer, T., Janusch, H., Hamann, C., Gödel, M., et al. (2010). Primary cilia regulate mTORC1 activity and cell size through Lkb1. *Nat. Cell Biol.* *12*, 1115–1122.
- Breslow, D.K., Koslover, E.F., Seydel, F., Spakowitz, A.J., and Nachury, M. V (2013). An in vitro assay for entry into cilia reveals unique properties of the soluble diffusion barrier. *J. Cell Biol.* *203*, 129–147.
- Bunney, T.D., and Katan, M. (2010). Phosphoinositide signalling in cancer: beyond PI3K and PTEN. *Nat. Rev. Cancer* *10*, 342–352.
- Cao, M., Ning, J., Hernandez-Lara, C.I., Belzile, O., Wang, Q., Dutcher, S.K., Liu, Y., and Snell, W.J. (2015). Uni-directional ciliary membrane protein trafficking by a cytoplasmic retrograde IFT motor and ciliary ectosome shedding. *Elife* *2015*.

- Chávez, M., Ena, S., Van Sande, J., de Kerchove d'Exaerde, A., Schurmans, S., and Schiffmann, S.N. (2015). Modulation of Ciliary Phosphoinositide Content Regulates Trafficking and Sonic Hedgehog Signaling Output. *Dev. Cell* 34, 338–350.
- Chaya, T., Omori, Y., Kuwahara, R., and Furukawa, T. (2014). ICK is essential for cell type-specific ciliogenesis and the regulation of ciliary transport. *EMBO J.* 33, 1227–1242.
- Christensen, S.T., Clement, C.A., Satir, P., and Pedersen, L.B. (2012). Primary cilia and coordination of receptor tyrosine kinase (RTK) signalling. *J. Pathol.* 226, 172–184.
- Clapham, D.E. (2007). Calcium Signaling. *Cell* 131, 1047–1058.
- Das, R.M., and Storey, K.G. (2014). Apical abscission alters cell polarity and dismantles the primary cilium during neurogenesis. *Science*. 343, 200–204.
- Delling, M., DeCaen, P.G., Doerner, J.F., Febvay, S., and Clapham, D.E. (2013). Primary cilia are specialized calcium signalling organelles. *Nature* 504, 311–314.
- Delling, M., Indzhykulian, A.A., Liu, X., Xie, T., Clapham, D.E., Ca, T., Ca, C., Figs, E.D., Fig, E.D., Fig, E.D., et al. (2016). Primary cilia are not calcium-responsive mechanosensors. *Nature* 531, 656–660.
- Dubreuil, V., Marzesco, A.M., Corbeil, D., Huttner, W.B., and Wilsch-Bräuninger, M. (2007). Midbody and primary cilium of neural progenitors release extracellular membrane particles enriched in the stem cell marker prominin-1. *J. Cell Biol.* 176, 483–495.
- Dummer, A., Poelma, C., DeRuiter, M.C., Goumans, M.-J.T.H., and Hierck, B.P. (2016). Measuring the primary cilium length: improved method for unbiased high-throughput analysis. *Cilia* 5, 7.
- Eley, L., Turnpenny, L., Yates, L.M., Craighead, A.S., Morgan, D., Whistler, C., Goodship, J.A., and Strachan, T. (2004). A perspective on inversin. *Cell Biol. Int.* 28, 119–124.
- Elias, J.E., and Gygi, S.P. (2007). Target-decoy search strategy for increased confidence in large-scale protein identifications by mass spectrometry. *Nat. Methods* 4, 207–214.
- Ezratty, E.J., Stokes, N., Chai, S., Shah, A.S., Williams, S.E., and Fuchs, E. (2011). A role for the primary cilium in notch signaling and epidermal differentiation during skin development. *Cell* 145, 1129–1141.
- Field, S., Riley, K.L., Grimes, D.T., Hilton, H., Simon, M., Powles-Glover, N., Siggers, P., Bogani, D., Greenfield, A., and Norris, D.P. (2011). Pkd111 establishes left-right asymmetry and physically interacts with Pkd2. *Development* 138, 1131–1142.
- Francis, S.S., Sfakianos, J., Lo, B., and Mellman, I. (2011). A hierarchy of signals regulates entry of membrane proteins into the ciliary membrane domain in epithelial cells. *J. Cell Biol.* 193, 219–233.
- Freund, J.B., Goetz, J.G., Hill, K.L., and Vermot, J. (2012). Fluid flows and forces in development: functions, features and biophysical principles. *Development* 139, 1229 LP-1245.
- Gamper, N., and Shapiro, M.S. (2007). Target-specific PIP(2) signalling: how might it work? *J. Physiol.* 582, 967–975.
- Garcia-Elias, A., Mrkonjic, S., Pardo-Pastor, C., Inada, H., Hellmich, U.A., Rubio-Moscardó, F., Plata, C., Gaudet, R., Vicente, R., and Valverde, M.A. (2013). Phosphatidylinositol-4,5-bisphosphate-dependent rearrangement of TRPV4 cytosolic tails enables channel activation by

physiological stimuli. *Proc Natl Acad Sci USA* 110, 9553–9558.

Garcia-Gonzalo, F.R., Phua, S.C., Roberson, E.C., Garcia, G., Abedin, M., Schurmans, S., Inoue, T., and Reiter, J.F. (2015). Phosphoinositides Regulate Ciliary Protein Trafficking to Modulate Hedgehog Signaling. *Dev. Cell* 34, 400–409.

Gees, M., Colasoul, B., and Nilius, B. (2010). The role of transient receptor potential cation channels in Ca<sup>2+</sup> signaling. *Cold Spring Harb. Perspect. Biol.* 2.

Giamarchi, A., and Delmas, P. (2007). Activation Mechanisms and Functional Roles of TRPP2 Cation Channels. In *TRP Ion Channel Function in Sensory Transduction and Cellular Signaling Cascades*, W. Liedtke, and S. Heller, eds. (Boca Raton (FL): CRC Press/Taylor & Francis).

Gilbert, S. (2000). Differentiation of the Neural Tube. In *Developmental Biology*, (Sunderland (MA): Sinauer Associates), p.

Goetz, S.C., and Anderson, K. V (2010). The primary cilium: a signalling centre during vertebrate development. *Nat. Rev. Genet.* 11, 331–344.

Grecco, H.E., Schmick, M., and Bastiaens, P.I.H. (2011). Signaling from the living plasma membrane. *Cell* 144, 897–909.

Gross, J.C., Chaudhary, V., Bartscherer, K., and Boutros, M. (2012). Active Wnt proteins are secreted on exosomes. *Nat. Cell Biol.* 14, 1036–1045.

Hakim, S., Dyson, J.M., Feeney, S.J., Davies, E.M., Sriratana, A., Koenig, M.N., Plotnikova, O. V., Smyth, I.M., Ricardo, S.D., Hobbs, R.M., et al. (2016). Inpp5e suppresses polycystic kidney disease via inhibition of PI3K/Akt-dependent mTORC1 signaling. *Hum. Mol. Genet.* 25, 2295–2313.

Hammond, G.R. V, and Balla, T. (2015). Polyphosphoinositide binding domains: Key to inositol lipid biology. *Biochim. Biophys. Acta - Mol. Cell Biol. Lipids* 1851, 746–758.

Hammond, G.R. V, Machner, M.P., and Balla, T. (2014). A novel probe for phosphatidylinositol 4-phosphate reveals multiple pools beyond the Golgi. *J. Cell Biol.* 205, 113–126.

Han, Y.-G., Kim, H.J., Dlugosz, A.A., Ellison, D.W., Gilbertson, R.J., and Alvarez-Buylla, A. (2009). Dual and opposing roles of primary cilia in medulloblastoma development. *Nat. Med.* 15, 1062–1065.

Hassounah, N.B., Bunch, T.A., and McDermott, K.M. (2012). Molecular Pathways: The Role of Primary Cilia in Cancer Progression and Therapeutics with a Focus on Hedgehog Signaling. *Clin. Cancer Res.* 18, 2429 LP-2435.

He, M., Subramanian, R., Bangs, F., Omelchenko, T., Liem, K.F., Kapoor, T.M., and Anderson, K. V (2014). The kinesin-4 protein Kif7 regulates mammalian Hedgehog signalling by organizing the cilium tip compartment. *Nat. Cell Biol.* 16, 663–672.

Hildebrandt, F., Benzing, T., and Katsanis, N. (2011). Ciliopathies. *N. Engl. J. Med.* 364, 1533–1543.

Hoey, D.A., Downs, M.E., and Jacobs, C.R. (2012). The mechanics of the primary cilium: An intricate structure with complex function. *J. Biomech.* 45, 17–26.

Hogan, M.C., Manganelli, L., Woollard, J.R., Masyuk, A.I., Masyuk, T. V, Tammachote, R., Huang, B.Q., Leontovich, A.A., Beito, T.G., Madden, B.J., et al. (2009). Characterization of PKD Protein-Positive Exosome-Like Vesicles. *J Am Soc Nephrol* 20, 278–288.

- Honda, A., Hirose, M., Hatori, M., Matoba, S., Miyoshi, H., Inoue, K., and Ogura, A. (2010). Generation of induced pluripotent stem cells in rabbits: potential experimental models for human regenerative medicine. *J. Biol. Chem.* 285, 31362–31369.
- Hori, Y., Kobayashi, T., Kikko, Y., Kontani, K., and Katada, T. (2008). Domain architecture of the atypical Arf-family GTPase Arl13b involved in cilia formation. *Biochem. Biophys. Res. Commun.* 373, 119–124.
- Horikawa, K., Yamada, Y., Matsuda, T., Kobayashi, K., Hashimoto, M., Matsu-ura, T., Miyawaki, A., Michikawa, T., Mikoshiba, K., and Nagai, T. (2010). Spontaneous network activity visualized by ultrasensitive Ca<sup>2+</sup> indicators, yellow Cameleon-Nano. *Nat. Methods* 7, 729–732.
- Hui, C., and Angers, S. (2011). Gli Proteins in Development and Disease. *Annu. Rev. Cell Dev. Biol.* 27, 513–537.
- Humbert, M.C., Weihbrecht, K., Searby, C.C., Li, Y., Pope, R.M., Sheffield, V.C., and Seo, S. (2012). ARL13B, PDE6D, and CEP164 form a functional network for INPP5E ciliary targeting. *Proc. Natl. Acad. Sci. U. S. A.* 109, 19691–19696.
- Humke, E.W., Dorn, K. V., Milenkovic, L., Scott, M.P., and Rohatgi, R. (2010). The output of Hedgehog signaling is controlled by the dynamic association between Suppressor of Fused and the Gli proteins. *Genes Dev.* 24, 670–682.
- Inoki, K., Ouyang, H., Zhu, T., Lindvall, C., Wang, Y., Zhang, X., Yang, Q., Bennett, C., Harada, Y., Stankunas, K., et al. (2006). TSC2 Integrates Wnt and Energy Signals via a Coordinated Phosphorylation by AMPK and GSK3 to Regulate Cell Growth. *Cell* 126, 955–968.
- Ishikawa, H., and Marshall, W.F. (2011). Ciliogenesis: building the cell's antenna. *Nat Rev Mol Cell Biol* 12, 222–234.
- Jacoby, M., Cox, J.J., Gayral, S., Hampshire, D.J., Ayub, M., Blockmans, M., Pernot, E., Kisseleva, M. V, Compère, P., Schiffmann, S.N., et al. (2009). INPP5E mutations cause primary cilium signaling defects, ciliary instability and ciliopathies in human and mouse. *Nat. Genet.* 41, 1027–1031.
- Johnson, C.M., Chichili, G.R., and Rodgers, W. (2008). Compartmentalization of phosphatidylinositol 4,5-bisphosphate signaling evidenced using targeted phosphatases. *J. Biol. Chem.* 283, 29920–29928.
- Käll, L., Canterbury, J.D., Weston, J., Noble, W.S., and MacCoss, M.J. (2007). Semi-supervised learning for peptide identification from shotgun proteomics datasets. *Nat. Methods* 4, 923–925.
- Kang, J.J., Toma, I., Sipos, A., McCulloch, F., and Peti-Peterdi, J. (2006). Quantitative imaging of basic functions in renal (patho)physiology. *Am. J. Physiol. Renal Physiol.* 291, F495–F502.
- Kim, S., Zaghloul, N. a, Bubenshchikova, E., Oh, E.C., Rankin, S., Katsanis, N., Obara, T., and Tsiokas, L. (2011). Nde1-mediated inhibition of ciliogenesis affects cell cycle re-entry. *Nat. Cell Biol.* 13, 351–360.
- Kleene, N.K., and Kleene, S.J. (2012). A method for measuring electrical signals in a primary cilium. *Cilia* 1, 1.
- Köttgen, M., Buchholz, B., Garcia-Gonzalez, M.A., Kotsis, F., Fu, X., Doerken, M., Boehlke, C., Steffl, D., Tauber, R., Wegierski, T., et al. (2008). TRPP2 and TRPV4 form a polymodal sensory channel complex. *J. Cell Biol.* 182, 437–447.

- Kukic, I., Rivera-Molina, F., and Toomre, D. (2016). The IN/OUT assay: a new tool to study ciliogenesis. *Cilia* 5, 23.
- Kusumi, A., Fujiwara, T.K., Chadda, R., Xie, M., Tsunoyama, T. a., Kalay, Z., Kasai, R.S., and Suzuki, K.G.N. (2012). Dynamic Organizing Principles of the Plasma Membrane that Regulate Signal Transduction: Commemorating the Fortieth Anniversary of Singer and Nicolson's Fluid-Mosaic Model. *Annu. Rev. Cell Dev. Biol.* 28, 215–250.
- Lancaster, M. a, Schroth, J., and Gleeson, J.G. (2011). Subcellular spatial regulation of canonical Wnt signalling at the primary cilium. *Nat. Cell Biol.* 13, 700–707.
- Lehtreck, K.F. (2015). IFT-Cargo Interactions and Protein Transport in Cilia. *Trends Biochem. Sci.* 40, 765–778.
- Lin, Y.-C., Niewiadomski, P., Lin, B., Nakamura, H., Phua, S.C., Jiao, J., Levchenko, A., Inoue, T.T., and Rohatgi, R. (2013). Chemically inducible diffusion trap at cilia reveals molecular sieve-like barrier. *Nat. Chem. Biol.* 9, 437–443.
- Luo, N., West, C.C., Murga-Zamalloa, C.A., Sun, L., Anderson, R.M., Wells, C.D., Weinreb, R.N., Travers, J.B., Khanna, H., and Sun, Y. (2012). OCRL localizes to the primary cilium: A new role for cilia in Lowe syndrome. *Hum. Mol. Genet.* 21, 3333–3344.
- Luo, N., Kumar, A., Conwell, M., Weinreb, R.N., Anderson, R., and Sun, Y. (2013). Compensatory Role of Inositol 5-Phosphatase INPP5B to OCRL in Primary Cilia Formation in Oculocerebrorenal Syndrome of Lowe. *PLoS One* 8.
- Ma, R., Li, W.-P., Rundle, D., Kong, J., Akbarali, H.I., and Tsiokas, L. (2005). PKD2 functions as an epidermal growth factor-activated plasma membrane channel. *Mol. Cell. Biol.* 25, 8285–8298.
- Mank, M., and Griesbeck, O. (2008). Genetically encoded calcium indicators. *Chem. Rev.* 108, 1550–1564.
- Mank, M., Santos, A.F., Drenth, S., Mersic-Flogel, T.D., Hofer, S.B., Stein, V., Hendel, T., Reiff, D.F., Levelt, C., Borst, A., et al. (2008). A genetically encoded calcium indicator for chronic in vivo two-photon imaging. *Nat. Methods* 5, 805–811.
- Maroto, R., Raso, A., Wood, T.G., Kurosky, A., Martinac, B., and Hamill, O.P. (2005). TRPC1 forms the stretch-activated cation channel in vertebrate cells. *Nat. Cell Biol.* 7, 85.
- Marshall, W.F., and Nonaka, S. (2006). Cilia: Tuning in to the Cell's Antenna. *Curr. Biol.* 16.
- Mattila, P.K., and Lappalainen, P. (2008). Filopodia: molecular architecture and cellular functions. *Nat. Rev. Mol. Cell Biol.* 9, 446–454.
- Moisoi, N., Erent, M., Whyte, S., Martin, S., and Bayley, P.M. (2002). Calmodulin-containing substructures of the centrosomal matrix released by microtubule perturbation. *J. Cell Sci.* 115, 2367 LP-2379.
- Monje, M., Mitra, S.S., Freret, M.E., Raveh, T.B., Kim, J., Masek, M., Attema, J.L., Li, G., Haddix, T., Edwards, M.S.B., et al. (2011). Hedgehog-responsive candidate cell of origin for diffuse intrinsic pontine glioma. *Proc. Natl. Acad. Sci. U. S. A.* 108, 4453–4458.
- Mourão, A., Christensen, S.T., and Lorentzen, E. (2016). The intraflagellar transport machinery in ciliary signaling. *Curr. Opin. Struct. Biol.* 41, 98–108.
- Mukhopadhyay, S., Wen, X., Ratti, N., Loktev, A., Rangell, L., Scales, S.J., and Jackson, P.K.

- (2013). The ciliary G-protein-coupled receptor Gpr161 negatively regulates the sonic hedgehog pathway via cAMP signaling. *Cell* 152, 210–223.
- Nachury, M. V., Seeley, E.S., and Jin, H. (2010). Trafficking to the ciliary membrane: how to get across the periciliary diffusion barrier? *Annu. Rev. Cell Dev. Biol.* 26, 59–87.
- Nager, A.R., Goldstein, J.S., Herranz-Pérez, V., Portran, D., Ye, F., Garcia-Verdugo, J.M., and Nachury, M. V (2017). An Actin Network Dispatches Ciliary GPCRs into Extracellular Vesicles to Modulate Signaling. *Cell* 168, 252–263.e14.
- Nakamura, T., and Hamada, H. (2012). Left-right patterning: conserved and divergent mechanisms. *Development* 139, 3257–3262.
- Narita, K., Kawate, T., Kakinuma, N., and Takeda, S. (2010). Multiple primary cilia modulate the fluid transcytosis in choroid plexus epithelium. *Traffic* 11, 287–301.
- Nauli, S.M., Alenghat, F.J., Luo, Y., Williams, E., Vassilev, P., Li, X., Elia, A.E.H., Lu, W., Brown, E.M., Quinn, S.J., et al. (2003). Polycystins 1 and 2 mediate mechanosensation in the primary cilium of kidney cells. *Nat. Genet.* 33, 129–137.
- Nonaka, S., Shiratori, H., Saijoh, Y., and Hamada, H. (2002). Determination of left–right patterning of the mouse embryo by artificial nodal flow. *Nature* 418, 96–99.
- Novak, J.P. (1997). Electric potential and concentration of ion species in the proximity of a cell membrane: ab initio calculations. *J. Theor. Biol.* 185.
- O'Connor, A.K., Malarkey, E.B., Berbari, N.F., Croyle, M.J., Haycraft, C.J., Bell, P.D., Hohenstein, P., Kesterson, R. a, and Yoder, B.K. (2013). An inducible CiliaGFP mouse model for in vivo visualization and analysis of cilia in live tissue. *Cilia* 2, 8.
- Oki, T., Nishimura, K., Kitaura, J., Togami, K., Maehara, A., Izawa, K., Sakaue-Sawano, A., Niida, A., Miyano, S., Aburatani, H., et al. (2014). A novel cell-cycle-indicator, mVenus-p27K-, identifies quiescent cells and visualizes G0-G1 transition. *Sci. Rep.* 4, 4012.
- Orhon, I., Dupont, N., Zaidan, M., Boitez, V., Burtin, M., Schmitt, A., Capiod, T., Viau, A., Beau, I., Wolfgang Kuehn, E., et al. (2016). Primary-cilium-dependent autophagy controls epithelial cell volume in response to fluid flow. *Nat. Cell Biol.* i, 657–667.
- Ott, C., Elia, N., Jeong, S.Y., Insinna, C., Sengupta, P., and Lippincott-Schwartz, J. (2012). Primary cilia utilize glycoprotein-dependent adhesion mechanisms to stabilize long-lasting cilia-cilia contacts. *Cilia* 1, 3.
- Otto, E. a, Schermer, B., Obara, T., O'Toole, J.F., Hiller, K.S., Mueller, A.M., Ruf, R.G., Hoefele, J., Beekmann, F., Landau, D., et al. (2003). Mutations in INVS encoding inversin cause nephronophthisis type 2, linking renal cystic disease to the function of primary cilia and left-right axis determination. *Nat. Genet.* 34, 413–420.
- Otto, E. a, Loeys, B., Khanna, H., Hellemans, J., Sudbrak, R., Fan, S., Muerb, U., O'Toole, J.F., Helou, J., Attanasio, M., et al. (2005). Nephrocystin-5, a ciliary IQ domain protein, is mutated in Senior-Loken syndrome and interacts with RPGR and calmodulin. *Nat. Genet.* 37, 282–288.
- Pan, J., Wang, Q., and Snell, W.J. (2004). An aurora kinase is essential for flagellar disassembly in *Chlamydomonas*. *Dev. Cell* 6, 445–451.
- Panáková, D., Sprong, H., Marois, E., Thiele, C., and Eaton, S. (2005). Lipoprotein particles are required for Hedgehog and Wingless signalling. *Nature* 435, 58–65.

- Paridaen, J.T.M.L., Wilsch-Bräuninger, M., and Huttner, W.B. (2013). Asymmetric inheritance of centrosome-associated primary cilium membrane directs ciliogenesis after cell division. *Cell* 155.
- Perrimon, N., Pitsouli, C., and Shilo, B.-Z. (2012). Signaling mechanisms controlling cell fate and embryonic patterning. *Cold Spring Harb. Perspect. Biol.* 4, a005975.
- Phua, S.C., Pohlmeier, C., and Inoue, T. (2012). Rapidly relocating molecules between organelles to manipulate small gtpase activity. *ACS Chem. Biol.* 7, 1950–1955.
- Phua, S.C., Lin, Y.C., and Inoue, T. (2015). An intelligent nano-antenna: Primary cilium harnesses TRP channels to decode polymodal stimuli. *Cell Calcium* 58, 415–422.
- Phua, S.C., Chiba, S., Suzuki, M., Su, E., Roberson, E.C., Pusapati, G. V., Setou, M., Rohatgi, R., Reiter, J.F., Ikegami, K., et al. (2017). Dynamic Remodeling of Membrane Composition Drives Cell Cycle through Primary Cilia Excision. *Cell* 168, 264–279.e15.
- Plotnikova, O. V., Seo, S., Cottle, D.L., Conduit, S., Hakim, S., Dyson, J.M., Mitchell, C.A., and Smyth, I.M. (2014). INPP5E interacts with AURKA, linking phosphoinositide signalling to primary cilium stability. *J Cell Sci* 364–372.
- Plotnikova, O. V., Pugacheva, E.N., and Golemis, E.A. (2009). Primary cilia and the cell cycle. *Methods Cell Biol.* 94, 137–160.
- Plotnikova, O. V., Nikonova, a. S., Loskutov, Y. V., Kozyulina, P.Y., Pugacheva, E.N., and Golemis, E. a. (2012). Calmodulin activation of Aurora-A kinase (AURKA) is required during ciliary disassembly and in mitosis. *Mol. Biol. Cell* 23, 2658–2670.
- Posor, Y., Eichhorn-Gruenig, M., Puchkov, D., Schöneberg, J., Ullrich, A., Lampe, A., Müller, R., Zarbakhsh, S., Gulluni, F., Hirsch, E., et al. (2013). Spatiotemporal control of endocytosis by phosphatidylinositol-3,4-bisphosphate. *Nature* 499, 233–237.
- Praetorius, H.A., and Spring, K.R. (2001). Bending the MDCK cell primary cilium increases intracellular calcium. *J. Membr. Biol.* 184, 71–79.
- Pugacheva, E.N., Jablonski, S.A., Hartman, T.R., Henske, E.P., and Golemis, E.A. (2007). HEF1-dependent Aurora A activation induces disassembly of the primary cilium. *Cell* 129, 1351–1363.
- Reiter, J.F., Blacque, O.E., and Leroux, M.R. (2012). The base of the cilium: roles for transition fibres and the transition zone in ciliary formation, maintenance and compartmentalization. *EMBO Rep.* 13, 608–618.
- Reitsma, S., Slaaf, D.W., Vink, H., Van Zandvoort, M.A.M.J., and Oude Egbrink, M.G.A. (2007). The endothelial glycocalyx: Composition, functions, and visualization. *Pflugers Arch. Eur. J. Physiol.* 454, 345–359.
- Rohacs, T. (2009). Phosphoinositide regulation of non-canonical transient receptor potential channels. *Cell Calcium* 45, 554–565.
- Rohatgi, R., Milenkovic, L., and Scott, M.P. (2007). Patched1 regulates hedgehog signaling at the primary cilium. *Science*. 317, 372–376.
- Rosenbaum, J.L., and Witman, G.B. (2002). Intraflagellar transport. *Nat. Rev. Mol. Cell Biol.* 3, 813–825.
- Rosivall, L., Mirzahosseini, S., Toma, I., Sipos, A., and Peti-Peterdi, J. (2006). Fluid flow in the juxtaglomerular interstitium visualized in vivo. *Am. J. Physiol. Renal Physiol.* 291, F1241–



F1247.

Roy, S., and Ingham, P.W. (2002). Hedgehogs tryst with the cell cycle. *J. Cell Sci.* 115, 4393–4397.

Rudge, S.A., and Wakelam, M.J.O. (2017). SnapShot: Lipid Kinase and Phosphatase Reaction Pathways. *Cell* 156, 376–376.e1.

Rydholm, S., Zwart, G., Kowalewski, J.M., Kamali-Zare, P., Frisk, T., and Brismar, H. (2010). Mechanical properties of primary cilia regulate the response to fluid flow. *Am. J. Physiol. Renal Physiol.* 298, F1096-102.

Saarikangas, J., Zhao, H., and Lappalainen, P. (2010). Regulation of the actin cytoskeleton-plasma membrane interplay by phosphoinositides. *Physiol. Rev.* 90, 259–289.

Sasai, N., and Briscoe, J. (2012). Primary cilia and graded Sonic Hedgehog signaling. *Wiley Interdiscip. Rev. Dev. Biol.* 1, 753–772.

Sasaki, H., Hui, C., Nakafuku, M., and Kondoh, H. (1997). A binding site for Gli proteins is essential for HNF-3 $\beta$  floor plate enhancer activity in transgenics and can respond to Shh in vitro. *Development* 124, 1313–1322.

Satir, P., Pedersen, L.B., and Christensen, S.T. (2010). The primary cilium at a glance. *J. Cell Sci.* 123, 499–503.

Schou, K.B., Pedersen, L.B., and Christensen, S.T. (2015). Ins and outs of GPCR signaling in primary cilia. *EMBO Rep.* 16, 1099–1113.

Schwartz, E.E.A., Leonard, M.L., Bizios, R., and Bowser, S.S. (1997). Analysis and modeling of the primary cilium bending response to fluid shear. *Am. J. Physiol.* 272, F132-8.

Seeger-Nukpezah, T., Little, J.L., Serzhanova, V., and Golemis, E.A. (2013). Cilia and cilia-associated proteins in cancer. *Drug Discov. Today Dis. Mech.* 10, e135–e142.

Sheldon, H., Heikamp, E., Turley, H., Dragovic, R., Thomas, P., Oon, C.E., Leek, R., Edelmann, M., Kessler, B., Sainson, R.C.A., et al. (2010). New mechanism for Notch signaling to endothelium at a distance by delta-like 4 incorporation into exosomes. *Blood* 116, 2385–2394.

Shewan, A., Eastburn, D.J., and Mostov, K. (2011). Phosphoinositides in cell architecture. *Cold Spring Harb. Perspect. Biol.* 3, 1–17.

Shi, J., Birnbaumer, L., Large, W.A., and Albert, A.P. (2014). Myristoylated alanine-rich C kinase substrate coordinates native TRPC1 channel activation by phosphatidylinositol 4,5-bisphosphate and protein kinase C in vascular smooth muscle. *FASEB J.* 28, 244–255.

Shiba, D., Yamaoka, Y., Hagiwara, H., Takamatsu, T., Hamada, H., and Yokoyama, T. (2009). Localization of Inv in a distinctive intraciliary compartment requires the C-terminal ninein-homolog-containing region. *J. Cell Sci.* 122, 44–54.

Shimizu, T., Janssens, A., Voets, T., and Nilius, B. (2009). Regulation of the murine TRPP3 channel by voltage, pH, and changes in cell volume. *Pflügers Arch. Eur. J. Physiol.* 457, 795–807.

Singh, B.B., Liu, X., Tang, J., Zhu, M.X., and Ambudkar, I.S. (2002). Calmodulin regulates Ca<sup>2+</sup>-dependent feedback inhibition of store-operated Ca<sup>2+</sup> influx by interaction with a site in the C terminus of TrpC1. *Mol. Cell* 9, 739–750.

- Singla, V., and Reiter, J.F. (2006). The primary cilium as the cell's antenna: signaling at a sensory organelle. *Science*. *313*, 629–633.
- Stamatiki, D., Ulloa, F., Tsoni, S. V., Mynett, A., and Briscoe, J. (2005). A gradient of Gli activity mediates graded Sonic Hedgehog signaling in the neural tube. *Genes Dev*. *19*, 626–641.
- Stauffer, T.P., Ahn, S., and Meyer, T. (1998). Receptor-induced transient reduction in plasma membrane PtdIns(4,5)P<sub>2</sub> concentration monitored in living cells. *Curr Biol* *8*, 343–346.
- Strotmann, R., Schultz, G., and Plant, T.D. (2003). Ca<sup>2+</sup>-dependent Potentiation of the Nonselective Cation Channel TRPV4 Is Mediated by a C-terminal Calmodulin Binding Site \*. *J. Biol. Chem.* *278*, 26541–26549.
- Su, S., Phua, S.C., DeRose, R., Chiba, S., Narita, K., Kalugin, P.N., Katada, T., Kontani, K., Takeda, S., and Inoue, T. (2013). Genetically encoded calcium indicator illuminates calcium dynamics in primary cilia. *Nat. Methods* *10*, 1105–1107.
- Suh, B.C., Inoue, T., Meyer, T., and Hille, B. (2006). Rapid chemically induced changes of PtdIns(4,5)P<sub>2</sub> gate KCNQ ion channels. *Science*. *314*, 1454–1457.
- Susaki, E., Nakayama, K., and Nakayama, K.I. (2007). Cyclin D2 translocates p27 out of the nucleus and promotes its degradation at the G0-G1 transition. *Mol. Cell. Biol.* *27*, 4626–4640.
- Svendsen, S., Zimprich, C., McDougall, M.G., Klaubert, D.H., and Los, G. V (2008). Spatial separation and bidirectional trafficking of proteins using a multi-functional reporter. *BMC Cell Biol.* *9*, 17.
- Tobin, J.L., and Beales, P.L. (2009). The nonmotile ciliopathies. *Genet. Med.* *11*, 386–402.
- Toftgard, R. (2009). Two sides to cilia in cancer. *Nat Med* *15*, 994–996.
- Torres, V.E., Harris, P.C., and Pirson, Y. (2007). Autosomal dominant polycystic kidney disease. *Lancet* *369*, 1287–1301.
- Travaglini, L., Brancati, F., Silhavy, J., Iannicelli, M., Nickerson, E., Elkhartoufi, N., Scott, E., Spencer, E., Gabriel, S., Thomas, S., et al. (2013). Phenotypic spectrum and prevalence of INPP5E mutations in Joubert Syndrome and related disorders. *Eur J Hum Genet* *21*, 1074–1078.
- Van Troys, M., Dewitte, D., Goethals, M., Carlier, M.F., Vandekerckhove, J., and Ampe, C. (1996). The actin binding site of thymosin beta 4 mapped by mutational analysis. *EMBO J.* *15*, 201–210.
- Tsujishita, Y., Guo, S., Stolz, L.E., York, J.D., and Hurley, J.H. (2001). Specificity determinants in phosphoinositide dephosphorylation: Crystal structure of an archetypal inositol polyphosphate 5-phosphatase. *Cell* *105*, 379–389.
- Ueno, T., Falkenburger, B.H., Pohlmeier, C., and Inoue, T. (2011). Triggering Actin Comets Versus Membrane Ruffles: Distinctive Effects of Phosphoinositides on Actin Reorganization. *Sci. Signal.* *4*, ra87-ra87.
- Viola, A., and Gupta, N. (2007). Tether and trap: regulation of membrane-raft dynamics by actin-binding proteins. *Nat. Rev. Immunol.* *7*, 889–896.
- Vriens, J., Watanabe, H., Janssens, A., Droogmans, G., Voets, T., and Nilius, B. (2004). Cell swelling, heat, and chemical agonists use distinct pathways for the activation of the cation channel TRPV4. *Proc. Natl. Acad. Sci. U. S. A.* *101*, 396–401.

- Vyas, N., Walvekar, A., Tate, D., Lakshmanan, V., Bansal, D., Lo Cicero, A., Raposo, G., Palakodeti, D., and Dhawan, J. (2014). Vertebrate Hedgehog is secreted on two types of extracellular vesicles with different signaling properties. *Sci. Rep.* *4*, 7357.
- Wang, J., Silva, M., Haas, L.A., Morsci, N.S., Nguyen, K.C.Q., Hall, D.H., and Barr, M.M. (2014). *C. elegans* ciliated sensory neurons release extracellular vesicles that function in animal communication. *Curr. Biol.* *24*, 519–525.
- Wang, J., Kaletsky, R., Silva, M., Williams, A., Haas, L.A., Androwski, R.J., Landis, J.N., Patrick, C., Rashid, A., Santiago-Martinez, D., et al. (2015). Cell-Specific Transcriptional Profiling of Ciliated Sensory Neurons Reveals Regulators of Behavior and Extracellular Vesicle Biogenesis. *Curr. Biol.* *25*, 3232–3238.
- Wang, W.-J., Tay, H.G., Soni, R., Perumal, G.S., Goll, M.G., Macaluso, F.P., Asara, J.M., Amack, J.D., and Tsou, M.-F.B. (2013). CEP162 is an axoneme-recognition protein promoting ciliary transition zone assembly at the cilia base. *Nat. Cell Biol.* *15*, 591–601.
- Wang, Y., Ding, Q., Yen, C.J., Xia, W., Izzo, J.G., Lang, J.Y., Li, C.W., Hsu, J.L., Miller, S.A., Wang, X., et al. (2012). The Crosstalk of mTOR/S6K1 and Hedgehog Pathways. *Cancer Cell* *21*, 374–387.
- Willingham, M.C., Wehland, J., Klee, C.B., Richert, N.D., Rutherford, A. V, and Pastan, I.H. (1983). Ultrastructural immunocytochemical localization of calmodulin in cultured cells. *J. Histochem. Cytochem.* *31*, 445–461.
- Wong, S.Y., Seol, A.D., So, P.-L., Ermilov, A.N., Bichakjian, C.K., Epstein, E.H., Dlugosz, A. a, and Reiter, J.F. (2009). Primary cilia can both mediate and suppress Hedgehog pathway-dependent tumorigenesis. *Nat. Med.* *15*, 1055–1061.
- Wood, C.R., and Rosenbaum, J.L. (2015). Ciliary ectosomes: Transmissions from the cell's antenna. *Trends Cell Biol.* *25*, 276–285.
- Wood, C.R., Huang, K., Diener, D.R., and Rosenbaum, J.L. (2013). The cilium secretes bioactive ectosomes. *Curr. Biol.* *23*, 906–911.
- Xu, Q., Zhang, Y., Wei, Q., Huang, Y., Hu, J., and Ling, K. (2016). Phosphatidylinositol phosphate kinase PIPKI $\gamma$  and phosphatase INPP5E coordinate initiation of ciliogenesis. *Nat. Commun.* *7*, 10777.
- Yarar, D., Waterman-Storer, C.M., and Schmid, S.L. (2007). SNX9 Couples Actin Assembly to Phosphoinositide Signals and Is Required for Membrane Remodeling during Endocytosis. *Dev. Cell* *13*, 43–56.
- Yasuhiko, Y., Imai, F., Ookubo, K., Takakuwa, Y., Shiokawa, K., and Yokoyama, T. (2001). Calmodulin binds to inv protein: Implication for the regulation of inv function. *Dev. Growth Differ.* *43*, 671–681.
- Yeh, C., Li, A., Chuang, J.Z., Saito, M., Cáceres, A., and Sung, C.H. (2013). IGF-1 Activates a cilium-localized noncanonical g $\beta$ y signaling pathway that regulates cell-cycle progression. *Dev. Cell* *26*, 358–368.
- Yoder, B.K., Hou, X., and Guay-Woodford, L.M. (2002). The polycystic kidney disease proteins, polycystin-1, polycystin-2, polaris, and cystin, are co-localized in renal cilia. *J. Am. Soc. Nephrol.* *13*, 2508–2516.
- Yoon, J.W., Kita, Y., Frank, D.J., Majewski, R.R., Konicek, B.A., Nobrega, M.A., Jacob, H.,

- Walterhouse, D., and Iannaccone, P. (2002). Gene expression profiling leads to identification of GLI1-binding elements in target genes and a role for multiple downstream pathways in GLI1-induced cell transformation. *J. Biol. Chem.* 277, 5548–5555.
- Yoshida, S., Shiratori, H., Kuo, I.Y., Kawasumi, A., Shinohara, K., Nonaka, S., Asai, Y., Sasaki, G., Belo, J.A., Sasaki, H., et al. (2012). Cilia at the node of mouse embryos sense fluid flow for left-right determination via Pkd2. *Science*. 338, 226–231.
- Young, Y.N., Downs, M., and Jacobs, C.R. (2012). Dynamics of the primary cilium in shear flow. *Biophys. J.* 103, 629–639.
- Zhang, Q., Taulman, P.D., and Yoder, B.K. (2004). Cystic kidney diseases: all roads lead to the cilium. *Physiology (Bethesda)*. 19, 225–230.
- Zhao, Y., Araki, S., Wu, J., Teramoto, T., Chang, Y.-F., Nakano, M., Abdelfattah, A.S., Fujiwara, M., Ishihara, T., Nagai, T., et al. (2011). An expanded palette of genetically encoded  $\text{Ca}^{2+}$  indicators. *Science*. 333, 1888–1891.
- Zheng, J. (2013). Molecular mechanism of TRP channels. *Compr. Physiol.* 3, 221–242.
- Zhou, J. (2009). Polycystins and primary cilia: primers for cell cycle progression. *Annu. Rev. Physiol.* 71, 83–113.

**CURRICULUM VITAE FOR Ph.D. CANDIDATES**  
The Johns Hopkins University School of Medicine

**Siew Cheng Phua**

**March 17<sup>th</sup> 2017**

**Educational History**

Ph.D. expected	2017	Program in Biochemistry, Cellular and Molecular Biology Mentor: Takanari Inoue Ph.D.	Johns Hopkins University School of Medicine
B.Sc.	2010	Program in Biological Sciences	Nanyang Technological University

**Other Professional Experience**

Ph.D. Candidate	2012-2017	Lab of Takanari Inoue, Johns Hopkins School of Medicine
Rotation student	2012-2012	Lab of Jeremy Nathans, Johns Hopkins School of Medicine
Rotation student	2012-2012	Lab of King-Wai Yau, Johns Hopkins School of Medicine
Research Officer	2010-2011	Lab of Colin L. Stewart, Institute of Medical Biology
B.Sc. Dissertation	2009-2010	Lab of Colin L. Stewart, Institute of Medical Biology
Research Scholar	2007-2008	Lab of Peter R. Preiser, Nanyang Technological University
Research Intern	2005-2007	Lab of Jackie Y. Ying, Institute of Bioengineering & Nanotechnology

**Scholarships**

2011-2016	National Science Scholarship <sup>1</sup>	A*STAR Singapore
2008-2010	A*STAR Pre-Graduate Scholarship <sup>2</sup>	A*STAR Singapore
2007-2008	President Research Scholarship <sup>3</sup>	Nanyang Technological University
2007-2008	Tan Teo Scholarship <sup>4</sup>	Nanyang Technological University

<sup>1</sup> A highly competitive five-year government fellowship that supports the top 1% science students in Singapore for overseas graduate training at leading institutions. This fellowship is administered by the Agency for Science, Technology and Research (A\*STAR), and covers tuition fees, insurance, local and overseas stipends as well as scientific conferences, with total support culminating to 600,000 USD. Awardees are selected based on scholastic excellence and potential to become leading scientists/engineers to drive R&D in Singapore.

<sup>2</sup> A two-year academic fellowship supporting top 5% of local university science/engineering undergraduates in their junior and senior years.

<sup>3</sup> A one-year research scholarship sponsoring top 5% of undergraduates for research training within the university.

<sup>4</sup> Founded by Google pioneer Chade-Meng Tan, this scholarship awards undergraduates based on their academic and extracurricular performance, creativity strength and concern for humanity.

## Awards & Honors

2017	Harold M. Weintraub Graduate Student Award	Fred Hutchinson Cancer Research Center
2016	The Lewis Travel Award	Johns Hopkins School of Medicine
2016	The Hans J. Prochaska Research Award	Johns Hopkins School of Medicine
2010	Bachelor of Science, First Class Honors	Nanyang Technological University
2009	Dean's List (Top 5% of cohort)	Nanyang Technological University
2008	Dean's List (Top 5% of cohort)	Nanyang Technological University
2007	Dean's List (Top 5% of cohort)	Nanyang Technological University

## Peer-Reviewed Publications

**Phua S.C.**<sup>\*\*</sup>, Chiba S., Suzuki M., Su E., Roberson E.C., Pusapati G.V., Setou M., Rohatgi R., Reiter J.F., Ikegami K.<sup>#</sup>, Inoue T.<sup>#</sup> Dynamic remodeling of membrane composition drives cell cycle through primary cilia excision. *Cell* 2017; 168(1-2), 264-279. (\*first author; <sup>#</sup>corresponding authors)

Garcia-Gonzalo F.R.\*, **Phua S.C.**\*, Roberson E.C., Garcia III G., Abedin M., Schurmans S., Inoue T., Reiter J.F. Ciliary phosphoinositides modulate Hedgehog signaling. *Developmental Cell* 2015; 34(4), 400-409. PMCID: PMC4557815. (\*co-first authors)

**Phua S.C.**<sup>\*\*</sup>, Lin Y.C., Inoue T.<sup>#</sup>. An intelligent nano-antenna: Primary cilium harnesses TRP channels to decode polymodal stimuli. *Cell Calcium* 2015; 58(4), 415-422. PMCID: PMC4564334. (\*first author; <sup>#</sup>corresponding authors)

Su S.\*, **Phua S.C.**\*, DeRose R., Chiba S., Narita K., Kalugin P.N., Katada T., Kontani K., Takeda S., and Inoue T. Genetically encoded calcium indicator illuminates calcium dynamics in primary cilia. *Nature Methods* 2013; 10(11), 1105-1107. PMCID: PMC3860264. (\*co-first authors)

Lin Y.C., **Phua S.C.**, Lin B., and Inoue T. Visualizing molecular diffusion through passive permeability barriers in cells: conventional and novel approaches. *Current Opinion in Chemical Biology* 2013; 17(4), 663-671. PMCID: PMC3860267.

Lin Y.C., Niewiadomski P.\*, Lin B.\*, Nakamura H.\*, **Phua S.C.**, Jiao J., Levchenko A., Inoue T., Rohatgi R., Inoue T. Chemically-inducible diffusion trap reveals molecular sieve-like barrier at primary cilia. *Nature Chemical Biology* 2013; 9(7), 437-443. PMCID: PMC3870470. (\*co-second authors)

**Phua S.C.**\*, Pohlmeier C., Inoue T. Rapidly relocating molecules between organelles to manipulate small GTPase activity. *ACS Chemical Biology* 2012; 7(12): 1950-1955. PMCID: PMC3528809. (\*first author)

Lai F.P.L., Mutalif R.A., **Phua S.C.**, Stewart C.L. Informatics-based analysis of mechanosignaling in the laminopathies. *Methods in Cell Biology* 2010; 98(C): 323-335.

Schumacher K.M., **Phua S.C.**, Schumacher A., Ying J.Y. Controlled formation of biological tubule systems in extracellular matrix gels in vitro. *Kidney International* 2008; 73(10): 1187-1192.

**Phua S.C.**\*, Parisa S., Preiser P.R. Acquisition of immunity to variant antigens on the surface of the malaria infected erythrocyte. *Proceedings of the URECA@NTU* 2007-08; 821 - 826. (\*first author)

## Posters and Oral Presentations

**Phua S.C.**, Inoue T. Ciliary PI(4,5)P<sub>2</sub> dictates fall of primary cilia and rise of cell cycle. *ASCB Annual Meeting*, Minisymposium 16: Dark matters in signaling and differentiation, San Francisco, CA, December 2016.

**Phua S.C.**, Chiba S., Suzuki M., Su E., Roberson E.C., Pusapati G.V., Setou M., Rohatgi R., Reiter J.F., Ikegami K., Inoue T. Ciliary PI(4,5)P<sub>2</sub> dictates fall of primary cilia and rise of cell cycle. *ASCB Annual Meeting*, Poster abstract, San Francisco, CA, December 2016.

**Phua S.C.** Discovering novel principles of primary cilia signaling. *Young Investigators' Day Lecture*, Johns Hopkins University School of Medicine, Baltimore, MD, April 2016.

**Phua S.C.**, Chiba S., Reiter J.F., Inoue T. Primary cilia PI(4,5)P<sub>2</sub> levels orchestrate ciliary F-actin assembly and cilia shaft separation. *FASEB SRC: The Biology of Cilia and Flagella*, Poster abstract, Snowmass, CO, July 2015.

**Phua S.C.**, Su S., Inoue T. Genetically encoded calcium indicator illuminates calcium dynamics in primary cilia. *Keystone Symposia: Cilia, Development and Disease*, Poster abstract, Tahoe City, CA, March 2014.

## Service and leadership

2015          Teaching Assistant for Scientific Foundation of Medicine- Cell Physiology